# Phase relations of Earth's core-forming materials

crystals

MDPI

*Review*

# Phase Relations of Earth's Core-Forming Materials

**Tetsuya Komabayashi**

School of GeoSciences and Centre for Science at Extreme Conditions, University of Edinburgh, Edinburgh EH9 3FE, UK; Tetsuya.komabayashi@ed.ac.uk; Tel.: +44-131-650-8518

**Abstract:** Recent updates on phase relations of Earth's core-forming materials, Fe alloys, as a function of pressure ($P$), temperature ($T$), and composition ($X$) are reviewed for the Fe, Fe-Ni, Fe-O, Fe-Si, Fe-S, Fe-C, Fe-H, Fe-Ni-Si, and Fe-Si-O systems. Thermodynamic models for these systems are highlighted where available, starting with 1 bar to high-$P$-$T$ conditions. For the Fe and binary systems, the longitudinal wave velocity and density of liquid alloys are discussed and compared with the seismological observations on Earth's outer core. This review may serve as a guide for future research on the planetary cores.

**Keywords:** phase relation; Earth's core; iron alloys; high-pressure; high-temperature; thermodynamics; extreme conditions



**Citation:** Komabayashi, T. Phase Relations of Earth's Core-Forming Materials. *Crystals* **2021**, *11*, 581. https://doi.org/10.3390/cryst11060581

Academic Editors: Daniel Errandonea and Simone Anzellini

Received: 31 March 2021
Accepted: 11 May 2021
Published: 22 May 2021



## 1. Introduction

The phase relations of Fe-alloys have been of primary importance in many research disciplines. For the engineering and metallurgy fields, the stability diagram of materials as a function of temperature ($T$) and composition ($X$) serves as a map to their target phase and its properties. In pursuit of this, phase relations at 1 bar were extensively studied for most of the binary Fe-alloy systems by experiment and theory. The stability diagrams of Fe-alloys are also important for Earth science as the major component of Earth's central core is iron. Because Earth's core is under high pressure ($P$) and temperature conditions, the stability diagrams need to be established for such extreme conditions.

High-pressure study of phase relations of Fe-alloys started around 1950 with shock loading experiments [1]. In the early days, the research was led by laboratory experiment which included static and dynamic compression techniques. Since around 2000, the theoretical approach with first-principles calculations became competitive with the experimental thanks to the enhanced computer performance and development of appropriate simplification of calculation. Currently, the experimental and theoretical approaches are considered to be complementary to each other. However, different approaches may give different results as is often the case, and therefore it is imperative to understand what properties are agreed on and what are not between the different/same techniques.

In this review, I will summarise recent updates on the phase relations of Earth's core-forming materials, Fe alloys, as a function of $P$-$T$-$X$ for the Fe, Fe-Ni, Fe-O, Fe-Si, Fe-S, Fe-C, Fe-H, Fe-Ni-Si, and Fe-Si-O systems. I highlight thermodynamic models based on experimental data for these systems, where available, starting with 1 bar to high-$P$-$T$ conditions. An experiment-based thermodynamic model, which includes thermodynamic potential functions of phases (e.g., the Gibbs free energy as a function of $P$-$T$-$X$), may provide information that is difficult to constrain by experiment such as the entropy of fusion and velocity of liquid under extreme conditions. Therefore, thus-calculated properties could serve as "experimental constraints" which can be compared with those from the first-principles calculations. For the Fe and binary systems, the longitudinal wave velocity and density of liquid alloys are discussed and compared with the seismological observations on Earth's outer core. This review may serve as a guide for the future research on the cores of terrestrial planets.

## 2. Theoretical Background

Here I briefly introduce thermodynamic functions that are needed for discussions in this paper.

### *2.1. Equation of State*

The equation of state (EoS) is needed for calculating the pressure effect on the Gibbs free energy, density, and elasticity of a phase. The detailed theoretical background of EoS can be found elsewhere [2,3].

The room-temperature molar volume of a phase upon compression can often be expressed with the third-order Birch–Murnaghan (BM) or Vinet EoS as:

$$P_{300} = \frac{3K_0}{2}\left[\left(\frac{V_0}{V}\right)^{\frac{7}{3}} - \left(\frac{V_0}{V}\right)^{\frac{5}{3}}\right]\left\{1 - \frac{3}{4}(4 - K\prime)\left[\left(\frac{V_0}{V}\right)^{\frac{2}{3}} - 1\right]\right\} \ldots .\text{BM} \quad (1)$$

$$P_{300} = 3K_0 x^{-2}(1 - x)\exp\left[\frac{3}{2}(K\prime - 1)(1 - x)\right] \ldots .\text{Vinet} \quad (2)$$

where $x \equiv (V/V_0)^{1/3}$ and, $P_{300}$, $K_0$, $K'$, and $V_0$ are the pressure at $T$ = 300 K, the isothermal bulk modulus, its pressure derivative, and the molar volume at $P$ = 1 bar and $T$ = 300 K, respectively.

In order to extrapolate an EoS to high temperature, either (i) the thermal pressure model or (ii) thermal expansivity model can be used.

(i) The thermal pressure model is described as:

$$P(V,T) = P(V,300\text{ K}) + Pth\ (V,T) \quad (3)$$

where $P(V,T)$, $P(V,300$ K), and $Pth(V,T)$ are the total pressure, pressure at 300 K for a given sample volume, and thermal pressure at a given temperature. The thermal pressure part may often be approximated as:

$$Pth = \alpha K_T \times (T - 300) \quad (4)$$

where $\alpha$ is the thermal expansion coefficient and $K_T$ is the isothermal bulk modulus. The $\alpha K_T$ value can be assumed to be constant near or above the Debye temperature. Therefore, a simple relation of $\alpha K_T = \alpha_0 K_0$ holds for materials with low Debye temperatures such as metals, where the subscript 0 indicates at 1 bar and 300 K.

Alternatively, the Mie–Grüneisen–Debye model can be used for the thermal pressure part in Equation (3) [3]:

$$Pth = \gamma/V\ \Delta Eth\ (\theta,T) \quad (5)$$

where $\gamma$ is the Grüneisen parameter, $\Delta Eth$ is the change in thermal energy, and $\theta$ is the Debye temperature. The thermal energy can often be calculated from the Debye approximation:

$$Eth = \frac{9nRT}{(\theta/T)^3}\int_0^{\theta/T}\frac{\xi^3}{e^{\xi} - 1}d\xi \quad (6)$$

where $n$, $\theta$, and $R$ are the number of atoms per formula unit, Debye temperature, and gas constant, respectively. The Debye temperature and Grüneisen parameter can be assumed to be functions of volume as:

$$\theta = \theta_0 \exp[(\gamma_0 - \gamma)/q] \quad (7)$$

and

$$\gamma = \gamma_0\ (V/V_0)^q \quad (8)$$

where $\theta_0$, $\gamma_0$, and $q$ are the Debye temperature, Grüneisen parameter at 1 bar and 300 K, and a dimensionless parameter, respectively. As mentioned above, $\theta_0$ for a metal is likely close to or below room temperature.

In the thermal pressure model (Equation (3)), there may be additional terms for anharmonic and electronic contributions. For example, hcp Fe shows large contributions from these terms [4]. The presence or absence of these additional contributions can be resolved when the $\alpha K_T$ term shows temperature dependence (Equation (4)) [5].

(ii) The thermal expansion coefficient can be modelled for a phase under high pressure using the Anderson–Grüneisen parameter, $\delta_T$ [6]:

$$\frac{\partial \ln \alpha}{\partial \ln V} = \delta_T = \delta_0 \eta^{\kappa} \tag{9}$$

where $\eta \equiv V/V_0$, $\delta_0$ is the value of $\delta_T$ at $P$ = 1 bar and $\kappa$ is a dimensionless parameter. This equation yields:

$$\frac{\alpha}{\alpha_0} = \exp\left[-\frac{\delta_0}{\kappa}(1-\eta^{\kappa})\right] \tag{10}$$

### *2.2. Thermodynamics*

Once a thermodynamic potential has been assessed, one can derive any equilibrium properties of the system [7]. The Gibbs free energy of a phase at a given $P$-$T$ condition ($G_{P,T}$) is expressed as:

$$G_{P,T} = G_{1\text{bar},T} + \int_{1\text{bar}}^{P} V_T dP \tag{11}$$

where $G_{1\text{bar},T}$ is the Gibbs free energy at $P$ = 1 bar and $T$ of interest and $V_T$ is the molar volume at $T$. $G_{1\text{bar},T}$ is often available from the metallurgy database for Fe-alloys (e.g., [8]). The volumetric term in Equation (11) is calculated from the $P$-$V$-$T$ EoS of the phase. Komabayashi [9,10] adopted the thermal expansion model (Equation (10)) in the free energy calculations. When a phase is a solution between end-members, such as Fe-alloys, its mixing property needs to be considered to obtain $G_{P,T}$. Many of the Fe-alloy liquids show nonideal mixing at 1 bar and its evolution with increasing pressure is of interest.

As mentioned above, one of the major advantages of thermodynamic modelling is that one can derive the properties that cannot be directly or easily constrained by experiment, such as the EoS of liquid phases. Komabayashi [9,10] evaluated EoS parameters for Fe-alloy liquid phases by calculating their melting curves which reproduce experimental data.

## 3. Phase Relations

Throughout the paper, I describe the composition of materials, for example, Fe-5 wt% Ni-4 wt% Si, as Fe-5Ni-4Si.

### *3.1. Major Components*

#### 3.1.1. Fe

Major issues in the phase relations of the main component of Earth's core, Fe(-Ni), include the $P$-$T$ location of the transition boundary between face-centred cubic (fcc) and hexagonal close-packed (hcp) structures, the stable structure in the inner core, and the melting point at the inner core-outer core boundary (ICB) corresponding to a pressure of 330 GPa.

- **The fcc-hcp Transition Boundary**

An important phase relation in iron is the fcc-hcp transition boundary. This boundary determines the $P$-$T$ location of an invariant point where the fcc, hcp, and liquid phases are stable [11–15] (Figure 1). Results of Shen et al. [12] and Boehler [13] highlighted a major inconsistency among experimental studies. The temperature values of the invariant point by both data are nearly the same of 2800 K, but the pressure values were very different: 60 GPa (Shen et al. [12]) and 100 GPa (Boehler [13]) (Figure 1), as a consequence of different $P$-$T$ slopes of the fcc-hcp boundary. Komabayashi et al. [14] revisited the boundary with internally resistive-heated diamond anvil cells (DAC) and precisely determined its slope. They also pointed out that the different slopes in the previous works could be partly re-

solved by taking into account the difference in estimates of thermal pressure during the experiments. Figure 1 summarises the results of experimental determinations of the fcc-hcp transition [11–14,16–18]. Among them, the *P-T* data where the pressures at high temperatures were calculated from internal pressure standards are fairly consistent [11,14,17,18]. In contrast, the high-temperature DAC studies in [12,13,16] did not consider thermal pressure effects. Therefore, it may be a coincident that Boehler's [13] result is rather consistent with Komabayashi et al.'s [14] data (Figure 1). The results of [12,16] would be relatively consistent with Komabayashi et al. [14] if the thermal pressure effects are considered which is about a 20 GPa increase upon heating to 2800 K based on the EoS of Fe [4]. As discussed later, Komabayashi [9] constructed a thermodynamic model of Fe including the fcc-hcp transition [14].

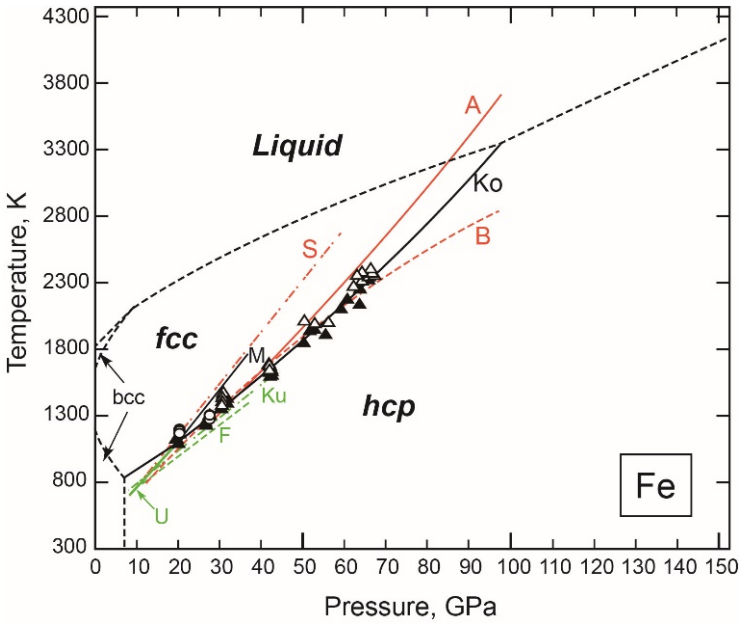


**Figure 1.** Pressure-temperature locations of the boundary of iron between face-centred cubic (fcc) and hexagonal close-packed (hcp) structures (S, Shen et al. [12]; B, Boehler [13]; M, Mao et al. [16]; U, Uchida et al. [11]; F, Funamori et al. [17]; Ku, Kubo et al. [18]; Ko, Komabayashi et al. [14]; and A, Anzellini et al. [15]). The other reaction boundaries (shown by dashed lines) are from Komabayashi [9].

More recently, Anzellini et al. [15] also determined the fcc-hcp transition boundary as part of their determination of the melting points of Fe to 200 GPa in laser-heated DAC. Their data show slightly higher, but still consistent, transition temperatures with Komabayashi et al.'s [14] data (Figure 1).

- **The Stable Structure in the Inner Core**

The stable iron structure in the inner core has been a literally "central" issue about the Earth as its physical properties, such as the melting/crystallising point and element partitioning upon crystallization, control core dynamics. Furthermore, the constituent phase structure would govern inner core dynamics, for example, the seismic anisotropy observed there, namely, seismic waves travel faster along the Earth's polar axis by 3–4% compared with equatorial directions [19–22], which will not be discussed in this paper as the focus is on the phase relations.

A growing number of data has accumulated supporting the conventional view that the hcp phase is the stable phase in the inner core [15,23–26]. Tateno et al. [23] reached the *P-T* conditions relevant to the centre of the Earth using a static device (i.e., DAC) (Figure 2a). Although samples in their experiments showed contamination by carbon from diamond anvils, their conclusion that the hcp phase is the stable iron phase in the inner core is

widely accepted. Other structures however have also been proposed by experiment and theory. Shock compression data by [27] showed two discontinuities in sound velocity. Assuming the second discontinuity was due to melting, the first one might have been from a solid-solid transition, and therefore, new phases were considered in the following studies (e.g., [28,29]).

A mixture of fcc and hcp phase was identified in X-ray diffraction (XRD) patterns in DAC samples quenched from high temperatures greater than 3700 K at above 160 GPa [30]. From their own first-principles calculations, Mikhaylushkin et al. [30] showed that the fcc-hcp transition boundary would be more temperature dependent at higher pressures due to the change in magnetic property [30] (Figure 2a). Stixrude [24] confirmed this temperature-dependent fcc-hcp transition slope of [30] by his own first-principles calculations within the quasiharmonic approximation, while he concluded that the hcp phase should be stable under Earth's core conditions. The *P*-*T* conditions of the experiments by [30] were close to the melting curve (Figure 2) and the Gibbs energies of hcp and fcc are similar at these *P*-*T* conditions in the vicinity of the fcc-hcp transition boundary, and therefore the possibility that the Fe sample once melted and the mixture of fcc and hcp phase crystallized from the melt upon quenching in [30] cannot be ruled out.

Possible stability of a bcc phase in the inner core was also proposed from classical molecular dynamics simulations [29] and later supported by several groups with the ab initio molecular or lattice dynamics simulations [31,32] (Figure 2a). Those studies claimed that the bcc phase at core pressures would not be dynamically stable at low temperatures, but should become stable at core temperatures due to the entropy effect. Luo et al. [31] discussed that the stability of the bcc phase cannot be properly addressed within the quasiharmonic approximation. There were no reports from experiment which observed the presence of the high-pressure bcc phase in pure iron. Since the expected *P*-*T* conditions are extremely high for a DAC study, there were not many XRD data relevant to the presence/absence of the high-pressure bcc phase [15,25]. In addition, so-called "fast crystallization" in these *P*-*T* conditions might have hindered those studies from obtaining a clear diffraction line.

- **The Melting Point at the ICB Pressure, 330 GPa**

The melting temperature of iron under core pressure has been extensively argued since 1986. Extrapolated shock wave data [27] indicated that the melting point of iron at 330 GPa was 6500 ± 300 K, while DAC studies reported significantly lower temperature of 4850 ± 200 K when extrapolated from 200 GPa [13] (Figure 2b). The melting points on the Hugoniots of different groups' shock compression data were generally consistent [33,34]. The latest shock compression data in which XRD patterns of liquid iron were obtained as a melting criterion reinforced the validity of the previous shock wave data [35] (Figure 2b). As such, the shock compression data are well consistent among different groups. First-principles calculations predicted melting points of hcp iron which are consistent with the shock compression data [36–38] although Laio et al.'s [39] calculations were consistent with the DAC data by [13] (Figure 2b). If the high-pressure bcc phase is stabilized, the melting point of Fe at the ICB pressure would be increased by about 300 K [29]. As such, there was a consensus that the melting point of iron at the ICB is in the order of 6300–6500 K between the studies with shock compression experiments and first-principles calculations.

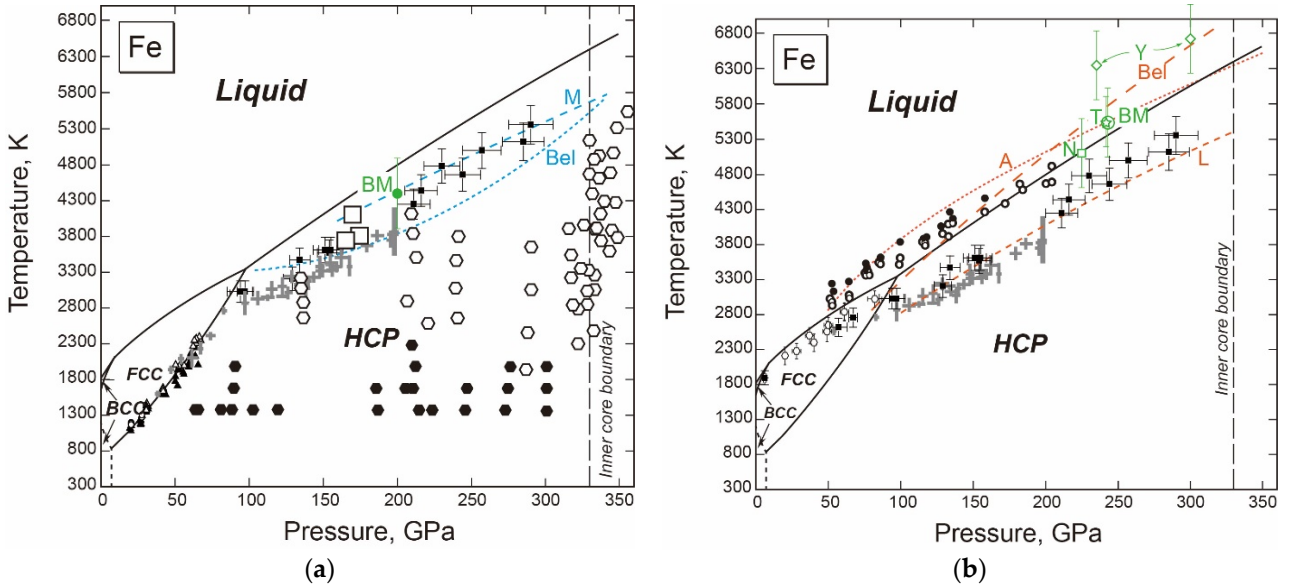


**Figure 2.** A phase diagram for iron [9] for discussions of (**a**) subsolidus and (**b**) melting relations. In (**a**), the plotted data are, the fcc–hcp transition boundaries in diamond anvil cells (DAC), Komabayashi et al. [14] (open triangle, fcc; solid triangle, hcp) and Boehler [13] (cross); stability of the hcp phase in DAC, Tateno et al. [23] (open hexagon) and Kuwayama et al. [26] (solid hexagon); stability of the fcc phase in DAC, Mikhaylushkin et al. [30] (square box); melting of the hcp phase in DAC, Boehler [13] (cross) and Sinmyo et al. [25] (small solid square with error bar); a phase transition in shock compression, Brown and McQueen [27] (BM, dot); the fcc-hcp transition by theory, Mikhaylushkin et al. [30] (M, blue dashed line); the hcp-bcc transition by theory, Belonoshko et al. [29] (Bel, blue dotted curve). In (b), the plotted data in addition to those in (**a**) are, melting in DAC, Jackson et al. [40] (open hexagon with error bar) and Anzellini et al. [15] (open circle, subsolidus; solid circle, melted); melting of the hcp phase by theory, Alfè et al. [38] (A, red dotted line), Belonoshko et al. [37] (Bel, red long dashed line), and Laio et al. [39] (L, red short dashed line); melting in shock compression, Brown and McQuee [27] (BM, green open circle), Yoo et al. [34] (Y, green open diamond), Nguyen et al. [33] (N, green open square), and Turneaure et al. [35] (T, green open star).

Newly improved static experimental measurements were reported by Anzellini et al. [15] in which melting was detected by the presence of diffuse scatterings from Fe liquid in laser-heated DAC. The previous melting experiments were based on the loss of diffractions lines from solids [12] or the detection of movement on the sample surface [13] as melting criteria. The results of [15] are well consistent with the shock wave and first-principles calculations, and the melting point of Fe at the ICB pressure should be 6230 ± 500 K [15]. Since the report by [15], the presence of a diffuse scattering has become a standard criterion for melting in the experimental mineral physics community. Published in the same year, Jackson et al. [40] also determined the melting points of fcc iron under pressure to 82 GPa using synchrotron Mössbauer spectroscopy which enabled them to monitor the dynamics of the iron atoms (Figure 2b). Their data showed somewhat lower melting temperatures than those of [15], but consistent with earlier [12,13] and recent measurements [25]. On the other hand, Morard et al. [41] discussed that Jackson et al.'s [40] data can be consistent with Anzellini et al.'s [15] when their pressure values were recalculated with revised thermal pressure values. As discussed later, the data of Jackson et al. [40] can be integrated into a thermodynamic model which is consistent with multi-anvil phase equilibrium data in the Fe-O system.

The quest for the accurate melting curve of iron in DAC is still on-going. Sinmyo et al. [25] used an internally resistive-heating system in DAC to place constraints on the melting point under high pressure to 290 GPa (Figure 2b). Their experiments had an advantage of stable and precise high-temperature generation as was the case for the fcc-hcp transition by [14]. The melting criteria in Sinmyo et al.'s [25] experiments did not include the presence of diffuse scatterings in XRD as was taken in [15] because the observation of a

diffuse scattering requires a sufficient amount of sample liquid, which Sinmyo et al. [25] claimed could be a source of overestimation of the experimental temperature on laser heating in [15]. Sinmyo et al.'s [25] melting points of hcp iron are systematically lower than Anzellini et al.'s [15] and higher than Boehler's [13] data and the extrapolated melting point at 330 GPa is 5500 ± 220 K.

- **An Integrated Thermodynamic Model**

Having reviewed the key phase relations of iron above, I here discuss the holistic picture of iron phase relations. Different pieces of experimental information can be integrated into a self-consistent thermodynamic model [9,42,43]. Among the latest models, the Fe database constructed by [9] has been widely used as a model based on latest high-*P*-*T* experimental measurements [4,14,15,44] together with 1 bar metallurgy data [43], although the model does not include the high-pressure bcc phase. Komabayashi [9] started with examining the thermodynamics of subsolidus phase relations including the fcc-hcp transition and extended it to include the liquid phase. The liquid EoS was assessed so that thermodynamic calculations would reproduce experimental data. As discussed later in the Fe-O system (Section 3.2.1), the melting points of Fe need to be lower than those of FeO at pressures to ~20 GPa, and therefore Fe melting points in [9] are somewhat lower than in Anzellini et al. [15] and more consistent with Jackson et al.'s [40] data (Figure 2b). Note that considering the experimental uncertainties, Komabayashi's [9] model is still consistent with both [15,40]. At higher pressures, the calculated melting curve becomes more consistent with Anzellini et al.'s [15] data, and reproduces the results of shock wave experiments and first-principles calculations (Figure 2b). In the following discussions, the iron database constructed by [9] will serve as a reference system.

- **Liquid Properties under Core Conditions**

Here I discuss some of the resulting properties of the thermodynamic model [9]. The entropy of fusion at 330 GPa calculated from the model is 7.17 J/K/mol, which is fairly consistent with 8.73 J/K/mol by the first-principles calculation [45]. The good agreement between the two different approaches implies that the values are reliable. Indeed, these values are close to the gas constant and this would prove that the Richard's rule (a constant entropy change on melting for metals on the order of the gas constant) (e.g., [46]) is still valid under such extreme *P*-*T* conditions.

The longitudinal wave velocity ($V_p$) and density of iron liquid calculated from the thermodynamic model [9] are compared with those from shock wave experiments [47], DAC experiments [48], and first-principles calculations [49,50], together with seismological models (preliminary reference Earth model (PREM), Dziewonski and Anderson [51]) over the outer core depths between the core-mantle boundary (CMB) and ICB (Figure 3). The different types of measurements, except those by [50], show consistent $V_p$ and density of iron liquid. The validity of the EoS for liquid iron in [9] was further confirmed by the first-principles calculation to 2 terapascals and 10,000 K [49]. As such, the Fe database of Komabayashi [9] based on static experimental data is consistent with shock compression studies and theoretical studies in phase relation and EoS of the phases. If one models the EoS for liquid iron using Sinmyo et al.'s [25] melting curve, its resulting density will be greater than the case of Komabayashi's [9] melting curve, which will have to be tested by comparing with those different types of measurements in the future.

Figure 3 shows that liquid iron shows a greater density by 7.1% and a reduced velocity by 3.7% compared with the PREM at the ICB conditions [9]. Similarly, the solid hcp Fe shows 4.5% greater density than the inner core. These values, so-called core density deficit (cdd), are the important starting point for the discussions of the kinds and amounts of light elements dissolved in the core. The cdd of the inner core has often been revised upon publication of a new EoS for the hcp phase and the most recent estimate is based on Fei et al. [52] of 3.6% at 6000 K. The cdd obviously depends on core temperature which can be constrained by the melting point at the ICB. The densities of iron liquid and solid, and

the melting point of iron at the ICB can only be simultaneously constrained by internally consistent thermodynamic models (e.g., [9]).

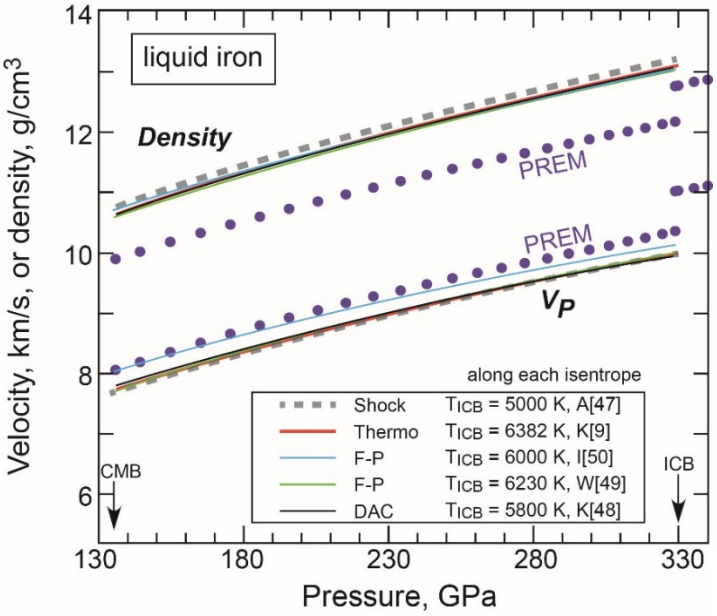


**Figure 3.** Density and longitudinal wave velocity (*Vp*) profiles for pure Fe over the outer core pressure range along each isentrope: shock wave study (Anderson and Ahrens [47]); thermodynamic model (Komabayashi [9]); first-principles calculation (Ichikawa et al. [50]; Wagle and Steinle-Neumann [49]); static measurements in DAC (Kuwayama et al. [48]). Data of the preliminary reference Earth model (PREM, Dziewonski and Anderson [51]) are also shown.

#### 3.1.2. Fe-Ni

Phase relations of the Fe-Ni system are reviewed here. In particular (i) the fcc-hcp transition boundary, (ii) the stable structure in the inner core, and (iii) the melting point at the ICB, are discussed in comparison with the cases of pure Fe (Section 3.1.1). The Ni content in Earth's core is expected to be 5–15 wt% from the cosmochemical arguments (see [53]) and therefore many of the existing reports were made on the Fe-rich portion, namely Fe-5-15Ni.

- **The fcc-hcp Transition Boundary**

Figure 4a summarizes the results of experimental determinations of the fcc-hcp phase transitions in the Fe-Ni system together with the results of pure iron (Fe-10Ni, [54]; Fe-5.4Ni, [55]; Fe-10.2Ni, [56]; Fe-9.7Ni, [57]; and Fe, [12,14]). Lin et al. [54], Mao et al. [55], and Shen et al. [12] did not consider thermal pressure effects upon heating, while Dubrovinsky et al. [56] and Komabayashi et al. [57] estimated the pressures at high temperatures, and therefore the comparison should be made for each of the former and latter groups. Both groups show that the addition of Ni to Fe reduces the transition temperature, expanding the stability field of the fcc phase. Komabayashi et al. [57] reported a narrower two-phase region where the fcc and hcp phases coexist than the other three works (Figure 4a). This may be a direct result of the use of the internal resistive-heating system with improved precision in temperature [57].

- **The Stable Structure in the Inner Core**

Since the fcc-hcp transition boundary in Fe-10Ni is placed at only slightly lower temperatures than in pure Fe, the stable phase in Fe-Ni Earth's inner core is expected to be hcp as well (e.g., [57]). However, Dubrovinsky et al. [56] reported the formation of a bcc phase in Fe-10Ni at above 225 GPa and 3400 K (Figure 4b). They also conducted first-principles calculations and found that the high-pressure bcc phase was dynamically unstable within the quasiharmonic approximation as is the case for pure Fe [31]. Their calculations demonstrated that Fe and Fe-10Ni bcc phases showed similar phonon spectra which implied that the effect of Ni is minor, and therefore they expected that high temperature should stabilize the bcc phase due to the entropic effect, same as for pure Fe [56]. Then, Sakai et al. [58] and Tateno et al. [59] conducted laser-heated DAC experiments on the same composition Fe-10Ni, but did not observe any phases other than hcp in their DAC experiments (Figure 4b).

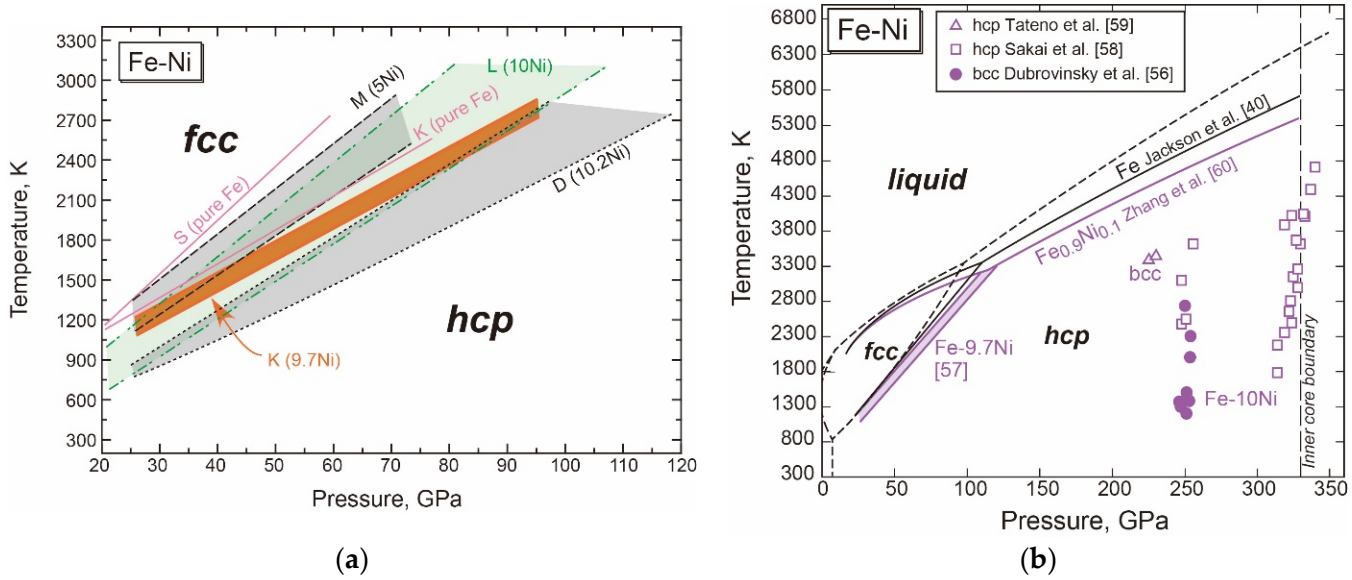


**Figure 4.** (**a**) Comparison of the *P*-*T* location of the fcc-hcp transition boundaries (L, Lin et al. [54]; M, Mao et al. [55]; D, Dubrovinsky et al. [56]; K, Komabayashi et al. [57]). The Ni content in wt% in each study is shown. For reference, the fcc-hcp transition boundaries in pure iron are shown (S, Shen et al. [12]; K, Komabayashi et al. [14]). Lin et al. [54], Mao et al. [55], and Shen et al. [12] did not take the thermal pressure upon laser heating into consideration, while Dubrovinsky et al. [56] and Komabayashi et al. [14,57] evaluated the pressures at high temperatures. (**b**) A phase diagram of Fe-10Ni (purple): the fcc-hcp transition boundaries [57]; melting of the fcc phase [60]. For comparison, iron phase relations are shown (black dashed line [9]; black solid line [40]). Note that Zhang et al. [60] took the same method as in Jackson et al. [40] to determine the fcc melting temperatures, and therefore, the effects of Ni can be seen from comparison of these two datasets. The stability of the hcp phase and high-pressure bcc phase was examined by Sakai et al. [58], Tateno et al. [59], and Dubrovinsky et al. [56].

- **The Melting Point at the ICB**

The melting points of the fcc and hcp phases in Fe-10Ni were measured to 125 GPa using laser-heated DAC and synchrotron Mössbauer spectroscopy by Zhang et al. [60], which was the same methodology as in [40] for pure Fe (Figure 4b). The results indicate that the addition of Ni negligibly changes the melting points of the fcc phase. However, the triple point where the hcp, fcc, and liquid phases are stable is moved to a higher pressure by the addition of Ni because of the steeper d$P$/d$T$ slope of the fcc-hcp transition boundary [57], which results in a depression of the melting point of the hcp phase by about 200 K for Fe-10Ni (Figure 4b). Similar discussions were recently made by Torchio et al. [61] from their new experimental measurements of melting point in more Ni-enriched systems

to Fe-36Ni. As discussed later in the Fe-Ni-Si system, Ni-bearing systems may be more complicated than expected from relevant binary systems.

### *3.2. Binary Systems with Light Elements*

Here I review phase relations of binary systems with light elements. The phase relations of iron by Komabayashi [9] are compared as a reference system.

#### 3.2.1. Fe-O

The Fe-O system shows many intermediate compounds between Fe and O. The relevant compositional range for the Earth's core falls between Fe and FeO and the subsystem Fe-FeO has been extensively studied.

- **Solid FeO**

FeO shows rich polymorphism from 1 bar to core *P-T* conditions including magnetic and metal-insulator transitions [62–70]. A metallic B8 structure was previously considered to be relevant to Earth's core due to an inferred strongly pressure-dependent phase boundary between B1 and B8 phases at about 70 GPa [63,65,66,71]. However, the slope of the boundary turned out to be less pressure-dependent [68] and the B8 phase was found to transition to a B2 phase under Earth's core *P-T* conditions [69]. On the other hand, the B1 phase is stable as a liquidus phase over a wide *P-T* range. This phase was considered to be insulating, but Fischer et al. [72] and Ohta et al. [70] demonstrated from either experiment, theory, or in combination, that it undergoes an insulator-metal transition at 30–90 GPa depending on temperature (Figure 5).

- **Melting of FeO**

Komabayashi [9] modelled the thermodynamics of FeO melting, while assessing the EoS of FeO liquid. The key phase relation is that B1 FeO is stable over a wide *P-T* range from 1 bar to 240 GPa and 5000 K as a liquidus phase (Figure 5), which enabled constraining the liquid EoS parameters using the EoS of the counterpart of solid B1 phase (e.g., [73]). The melting temperatures of B1 FeO were experimentally constrained to 77 GPa [74–77] and Ozawa et al. [69] constrained the stability of solid FeO phases (B1 and B2) up to about $T$ = 5000 K at $P$ = 240 GPa. Komabayashi [9] obtained EoS parameters of liquid FeO that give a calculated melting curve consistent with selected experimental measurements. The calculated melting curve is shown in Figure 5. Komabayashi [9] pointed out that consistency between the melting points of Fe and FeO should be considered (Figure 6a,b); the melting temperature of FeO needs to be higher than that of pure iron at about 15 GPa in order to reproduce binary phase assemblages determined in multi-anvil experiments (e.g., [77]) (Figure 6b). The melting temperatures of FeO determined by [74] are much lower than those of pure iron [15] at about 15 GPa and hence were not integrated in the thermodynamic model by [9] which is consistent with [15].

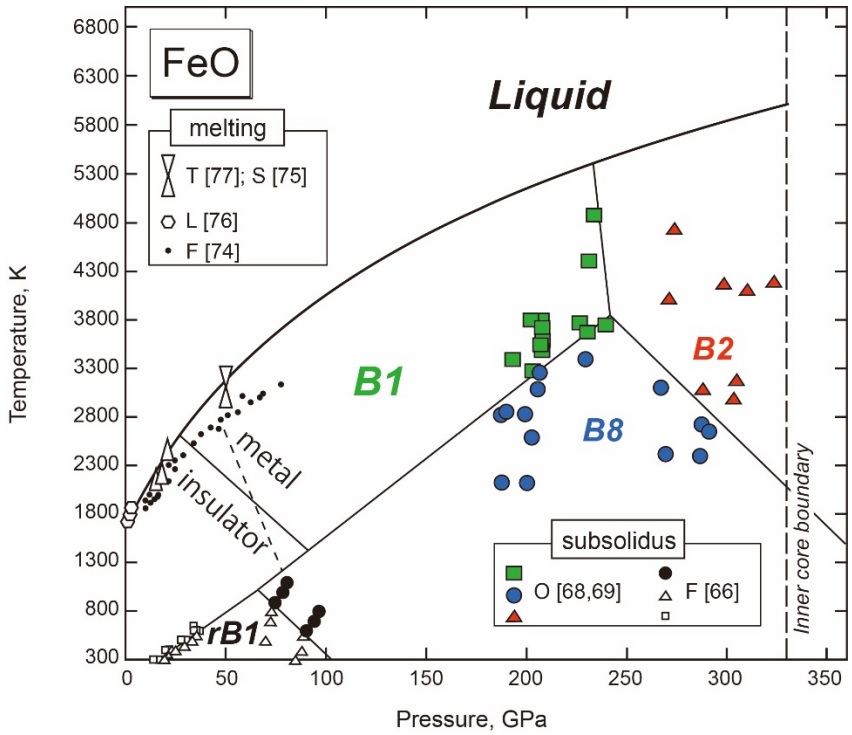


**Figure 5.** Phase relations of FeO. The solid black curve is the melting curve of the B1 structure extended to the inner core-outer core boundary, which was calculated with the thermodynamic model [9]. Thin solid straight lines are solid-solid reactions which divide stability fields of the phases. The B1 structure undergoes insulator-metal transition (dashed line [72]; solid line [70]). Melting experimental data to constrain the equation of state (EoS) of the liquid are plotted (Lindsley [76]; Tsuno et al. [77]; Seagle et al. [75]). High-pressure stability of solid FeO is indicated (Ozawa et al. [68,69]). The stability of rhombohedral B1 (rB1) phase is by Fei and Mao [66]. The small filled circle is the melting point of FeO (Fischer and Campbell [74]) which was not used for the liquid EoS determination in [9].

- **The Fe-FeO System**

The Fe-FeO system is characterized by the presence of a large miscibility gap above the solidus between Fe-rich metallic liquid and FeO-rich ionic liquid [77–79] (Figure 6a). The mixing property of liquid Fe and FeO was well examined at 1 bar [80,81]. The pressure dependence of the mixing interaction parameters was assessed by Frost et al. [82] based on two-liquid immiscibility data obtained in their own experiments up to 25 GPa. At greater pressures, the system behaves as a simple binary eutectic system [75] (Figure 6c,d). Komabayashi [9] calculated the eutectic relations to 50 GPa (Figure 6b,c) using the mixing parameters by [82] and at the core pressures (Figure 6d) with ideal mixing employed. Although Frost et al.'s [82] model was aimed at calculating the oxygen partitioning between the mantle and core, their mixing parameters reproduced the experimental data to 50 GPa well (Figure 6c). Komabayashi [9] also calculated the pressure dependence of eutectic composition, which is compared with experimental measurements in Figure 7 [75,77,78,83–86]. The calculated oxygen content in eutectic melt shows a steep rise at 30–60 GPa [9] which is consistent with earlier experimental data in laser-heated DAC [75]. Recent experiments further reinforced this pressure effect [85,86] (Figure 7), although Morard et al. [85] reported the steep rise at some greater pressures (~80 GPa).

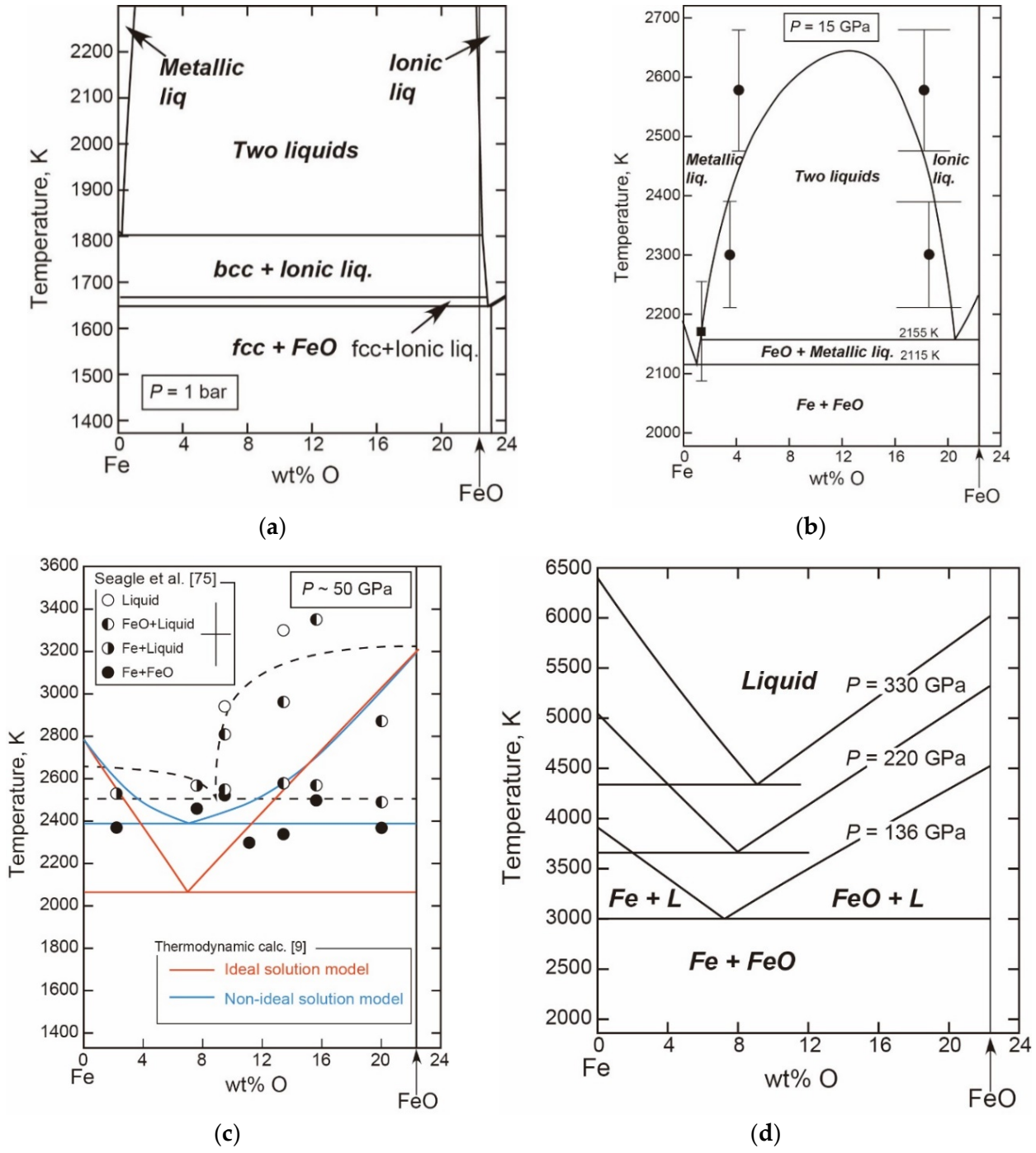


**Figure 6.** Eutectic relations in the system Fe-FeO at (**a**) 1 bar, (**b**) 15 GPa, (**c**) 50 GPa, and (**d**) 136–330 GPa. (**a**) is from [79] and (**b**–**d**) are from [9]. In (**b**), calculated phase relations [9] and experimental data of the compositions of liquids [77] are plotted: circle, coexisting two liquids; square, a liquid coexisting with solid FeO. In (**c**), calculated eutectic relations [9] are compared with laser-heated DAC experimental data [75]. The experimental error bar is shown in the inset, and the dashed line is the liquidus curve that Seagle et al. [75] drew. The calculations were made with the ideal solution and nonideal solution models [82] assumed. In (**d**), eutectic relations to the inner core boundary pressure were calculated with the ideal solution employed for the liquids. L, liquid.

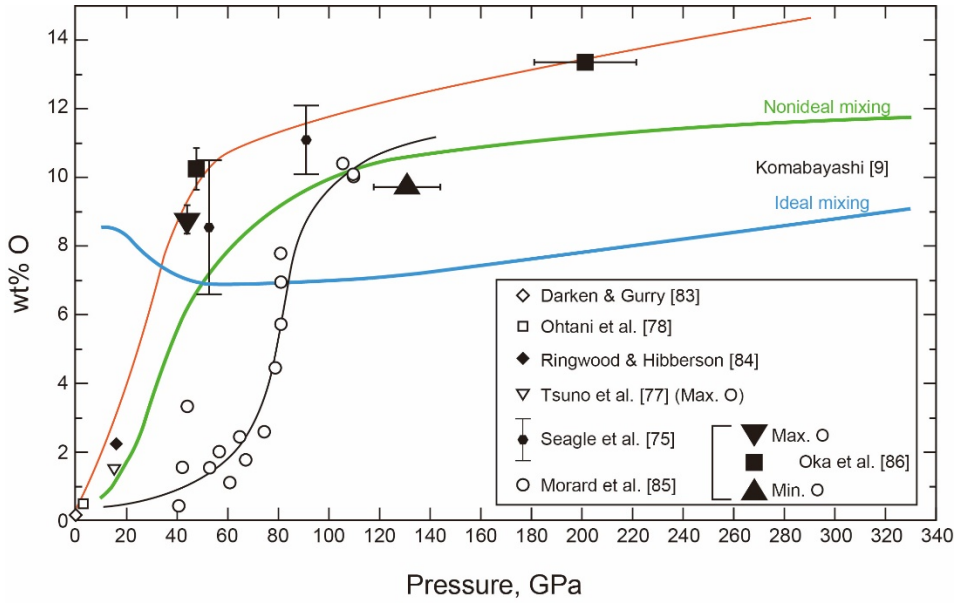


**Figure 7.** Change in eutectic composition of the Fe-FeO system as a function of pressure. Calculated eutectic compositions are shown as green (nonideal) and blue (ideal) lines [9]. Experimental estimates are plotted (Darken and Gurry [83]; Ohtani et al. [78]; Ringwood and Hibberson [84]; Tsuno et al. [77]; Seagle et al. [75]; Morard et al. [85]; Oka et al. [86]). The red and black curves were fitted to [86] and [85], respectively.

I here calculated a *G*-*X* relation for liquids and solids in the Fe-FeO system from the thermodynamic database [9,82] (Figure 8) to make detailed analyses of the increasing oxygen content in eutectic melt with increasing pressure. At a low pressure of 15 GPa, the nonideal mixing of Fe and FeO liquids forms two minima in the free energy curve, which accounts for the liquid immiscibility for intermediate bulk compositions. The eutectic point where solid fcc Fe and liquid coexist is very close to Fe (Figure 8, upper panel). With increasing pressure, the pressure effect stabilizes the liquids in the intermediate compositional range, and therefore the free energy curve becomes a simple downward convex curve where the two-liquid field diminishes (<50 GPa) while the eutectic point is moving towards the FeO side (Figure 8, middle panel). At a greater pressure of 90 GPa, the eutectic point is at about 9 wt% O (Figure 8, lower panel) and there is no further move with further increasing pressure because there is no longer drastic change in the shape of the free energy curve.

A liquid immiscibility occurs when the mixing enthalpy is a large positive value and disappearance of the two-liquid field often occurs with increasing temperature at a fixed pressure, for example, at 1 bar, due to the effect of configurational entropy. However, the Fe-FeO system shows disappearance of the liquid immiscibility with increasing pressure at a fixed temperature as well [82]. This indicates that the mixing enthalpy becomes smaller with pressure; in other words, the end-member liquids which are metallic Fe-rich liquid and ionic FeO-rich liquid become compatible at high pressures. Komabayashi [9] discussed that a potential source for the reduction in nonideality with increasing pressure is metallization of FeO liquid. Metallization of subsolidus B1 FeO was observed by experiment and theory [70,72], which occurred at 30–90 GPa depending on temperature. The structure of a liquid may change according to that of the counterpart crystalline phase (e.g., [87]). Hence FeO liquid might become a metal at pressures in the vicinity of the transition in the solid, which might make it compatible with Fe liquid. As such, the rapid increase in the oxygen content in eutectic melt at 30–60 GPa could be as a consequence of metallization of liquid FeO [9,85]. Although there is a slight difference in the pressure where the oxygen content starts rising between the studies [9,75,85,86], the important point is that the pressure dependence of the nonideal mixing parameters established for another geological

reaction [82] reproduces the change in eutectic composition with pressure [9] and this is also consistent with the pressure range of metallization of B1 FeO [70,72].

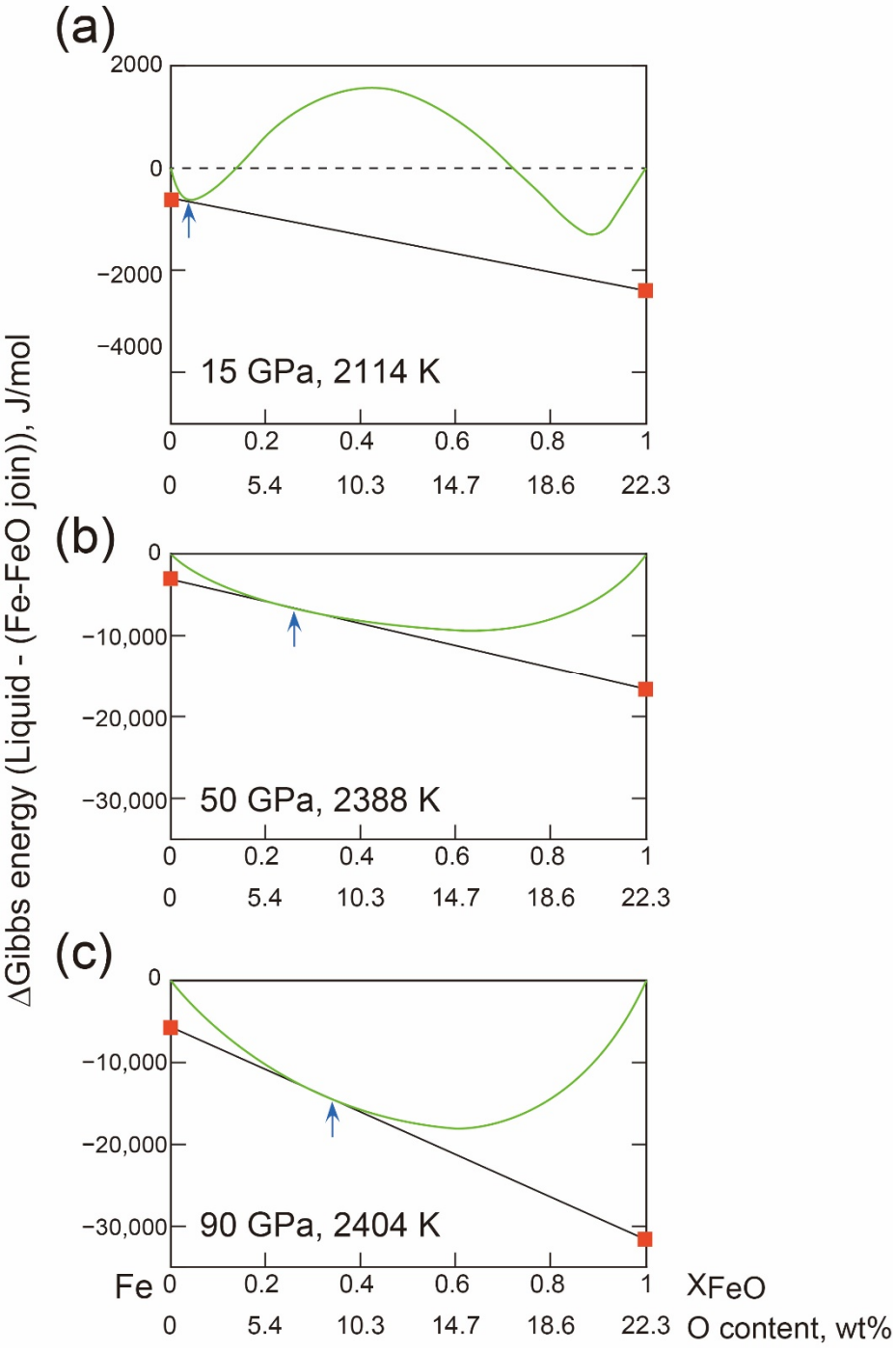


**Figure 8.** Gibbs energy-composition (*G*-*X*) diagrams for the Fe-FeO system at the eutectic temperatures for (**a**) 15 GPa, (**b**) 50 GPa, and (**c**) 90 GPa, which were calculated with the thermodynamic model [9]. The green curve represents the free energy curve for the liquids and the red squares are the free energies of solid Fe and FeO. The eutectic points are indicated by arrow. From low to high pressures, the nonideality of the Fe-FeO liquids decreases, which moves the eutectic point from oxygen-depleted side to -enriched side. The reduction of nonideality should be associated with metallization of B1 FeO [70,72].

As for the eutectic temperature, Komabayashi [9] discussed that the nonideal mixing model reproduced DAC experimental data to 50 GPa and the ideal mixing model worked for the data of [69] to pressures above 200 GPa (Figure 9). Recent laser-heated DAC data [85,86] are also consistent with the ideal mixing model. This agreement between the thermodynamic calculations and experiments indicates that the mixing property indeed changes from the highly nonideal at low pressures to ideal under core pressures. The calculated eutectic compositions at the core pressures are slightly depleted in oxygen than the experimental measurements (Figure 7). This could be resolved if the melting points of FeO would be elevated, which can be tested in the future.

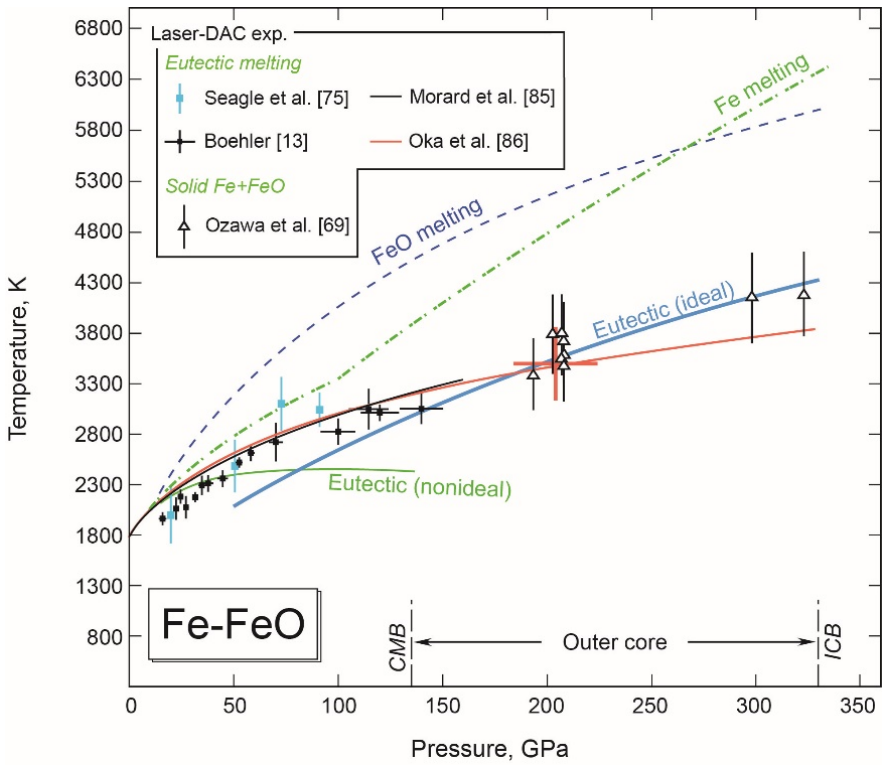


**Figure 9.** Eutectic melting temperatures in the Fe-FeO system together with the melting curve for each end-member composition. The green and blue solid lines give the calculated eutectic temperatures assuming the nonideal and ideal solution for liquids, respectively [9]. The squares with error bars are experimentally determined eutectic temperatures (blue, Seagle et al. [75]; black, Boehler [13]). The triangles are points of stability of solid Fe + FeO observed in DAC experiments [69]. The solid black and red curves are experimentally constrained eutectic curves by Morard et al. [85] and Oka et al. [86], respectively. The red cross denotes the error bar for [86]. CMB, core-mantle boundary; ICB, inner core boundary.

- **The Liquid Properties**

The *Vp* and density of Fe-FeO liquids were calculated from the thermodynamic model [9]. The results are shown in Figure 10 together with first-principles calculations [88,89]. The calculated results by [9] show that the addition of oxygen to Fe liquid reduces both the density and *Vp*, while the theoretical calculations show a reduction in density but an increase in *Vp*. Figure 10b shows the effects of oxygen on the liquid iron properties: density, adiabatic bulk modulus (*Ks*), and *Vp*. Komabayashi's [9] model predicted a negative effect (i.e., decrease) on the velocity by the addition of oxygen, while the first-principles calculations by Badro et al. [88] and Ichikawa and Tsuchiya [89] predicted positive effects (Figure 10b). However, this does not necessarily imply that the experiment-based and theory-based results are complete opposites. The result depends on the magnitude of reduction of the bulk modulus of iron liquid due to oxygen. All of [9,88,89] show that the addition of

oxygen reduces both the bulk modulus and density (Figure 10b). The *Vp* of iron liquid is reduced in Komabayashi [9] because the bulk modulus decreases more than the density by mixing an oxygen component. As such, the *Vp* may increase or decrease due to oxygen depending on the difference in the bulk modulus between the end-members (i.e., Fe and FeO in [9]). In his modelling of the EoS of liquid phases, Komabayashi [9] demonstrated that the compressibility of a liquid should be close to that of the counterpart crystalline phase under core pressure, and the small bulk modulus of liquid FeO was a consequence of the small bulk modulus of solid B1 FeO. The EoS of solid B1 FeO was established based on experimental data to 207 GPa and 3800 K [69,73] which are relevant to core conditions and therefore its elastic behaviour can be reliably applied. Komabayashi [9] listed a set of EoS for the solids and liquids in the Fe-O system while the first-principles calculations did not provide such a self-consistent set of EoS for the solids and liquids. Further comparison is needed to resolve the difference between experiment and theory.

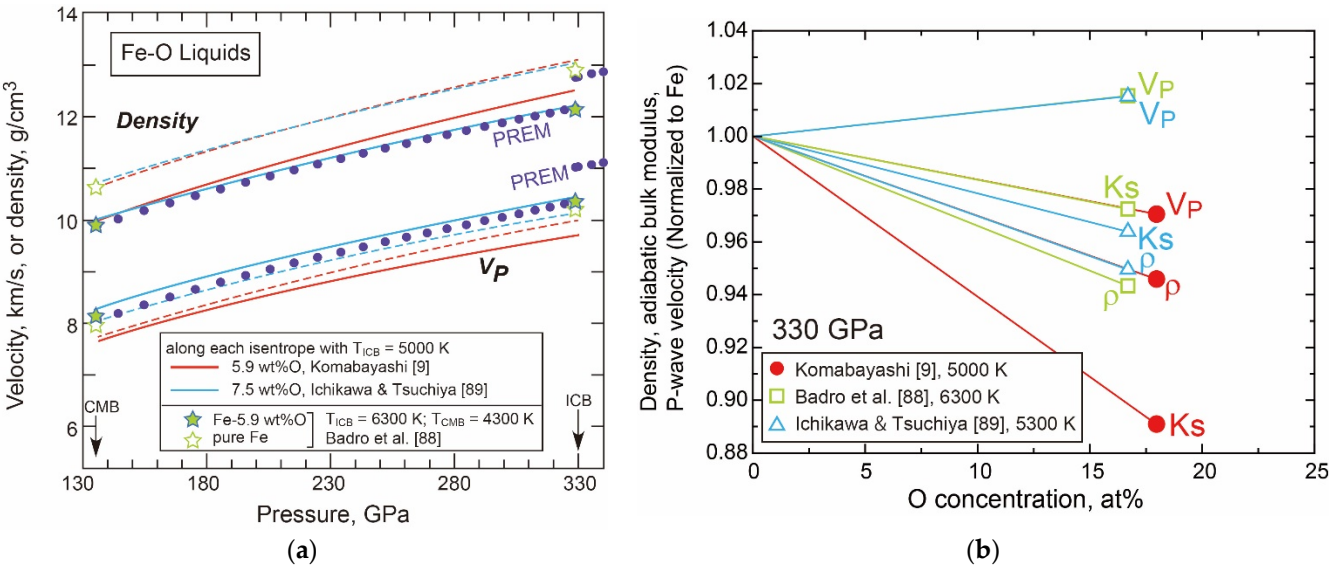


**Figure 10.** (**a**) Density and *Vp* profiles for Fe-O outer core models along each isentrope from thermodynamic calculations (Fe-5.9O, [9]) and first-principles calculations (Fe-7.5O, [89]). Furthermore, results of another theoretical calculation at the CMB and ICB are shown [88]. Note that the plots for Fe-5.9O needed a slight extrapolation in composition for [88]. For comparison, pure iron data are plotted (red dashed line with $T_{ICB}$ = 6382 K [9]; blue dashed line with $T_{ICB}$ = 6000 K [50]). (**b**) Effects of oxygen on the *Vp*, adiabatic bulk modulus (Ks), and density ($\rho$) of liquid iron at 330 GPa. Data from different approaches are compared (Komabayashi [9]; Badro et al. [88]; Ichikawa and Tsuchiya [89]). Note that the parameters are normalized to those for pure iron. The effect of oxygen on *Ks* is more pronounced than on $\rho$, resulting in a reduction of *Vp* in [9].

The above analyses suggest that Fe-O liquids may or may not account for the outer core profiles (Figure 10a). On the other hand, hcp iron may crystallise to form the inner core, if the outer core contains 5.9–7.5 wt% oxygen [88,89] since the oxygen content in eutectic melt would be greater (Figure 7). The crystallised hcp iron would however not accommodate any amount of oxygen [68] so that it cannot account for the inner core density deficit. Therefore, the addition of oxygen alone to iron cannot fully explain the PREM profiles of the core.

3.2.2. Fe-Si

The Fe-Si system is characterised by a narrow melting loop of the bcc Fe phase at 1 bar which partitions Si into both solid and liquid. This could account for the cdd of both the solid and liquid cores if high-pressure iron phases would show similar melting relations. The phase relations and EoS of solid phases in the Fe-(Fe)Si system have been extensively studied by both experiment and theory [90–99].

- **The *T*-*X* Relations**

Phase relations in the Fe-Si system are complicated with many different solid phases involved at low pressures, but they become simpler with increasing pressure (Figure 11). Above 100 GPa the subsystem Fe-FeSi, which is relevant to Earth's core, only includes hcp iron, B2, and liquid phases (e.g., [95]) (Figure 11d). Fischer et al. [95,100] determined phase relations based on in situ XRD while Ozawa et al. [98] placed constraints on the width of melting loops based on chemical analyses of recovered DAC samples. The two studies are qualitatively consistent, but some details need attention. While the compositional range of fcc + B2 at 50 GPa (Figure 11b) and hcp + B2 at 125 GPa (Figure 11d) constrained by Ozawa et al. [98] are not inconsistent with the data in Fe-9Si and Fe-16Si by [95], the compositional ranges of fcc + B2 and hcp + B2 at 80 GPa (Figure 11c) which are well constrained by [95] seem too wide compared with Ozawa et al.'s [98] data at 50 and 125 GPa (Figure 11b,d). This apparent discrepancy is due to the very large compositional range of the B2 solid solution phase in [98]. This should further be examined, by an alternative approach such as first-principles calculation.

- **The fcc-hcp Transition**

Because the Fe-phases (bcc, fcc, and hcp) form extensive solid solutions with Si, as was discussed in Fe-Ni (Section 3.1.2), the fcc-hcp transition boundary is discussed here. Figure 12 summarises the experimental attempts to determine the *P*-*T* locations of the fcc-hcp transition boundaries in the Fe-Si system with in situ synchrotron XRD [97,99,101]. An experimental study with laser-heated DAC reported that the transition temperature was greatly reduced when 3.4 wt% Si was added to Fe [101]. In contrast, Tateno et al. [97] showed increased transition temperatures in Fe-6.5Si, which was later supported by Komabayashi et al. [99] who employed internally resistive-heated DAC experiments in Fe-4Si (Figure 12). Komabayashi et al. [99] noted that Asanuma et al. [101] assigned tiny shallow rises as peaks from the fcc phase, while the appearance of the fcc phase was clearly marked by the presence of the (200) peak in [14,57,99] (Figure 13).

- **The Stable Structure in the Inner Core**

The stable structure in a hypothetical Fe-Si inner core has been discussed in relation to a reaction boundary: hcp → hcp + B2 (Figures 11d and 14) [93,95,97,102]. Fischer et al. [95] and Tateno et al. [97] determined this boundary in Fe-9Si by synchrotron XRD in laser-heated DAC to 201 GPa and 407 GPa, respectively, and both results agree well (Figure 14). According to Tateno et al.'s [97] boundary, if the inner core temperature is below 4800 K, the inner core can be a sole hcp phase with up to 9 wt% Si.

On the other hand, theoretical studies reported a possible presence of the high-pressure bcc phase at a lower Si concentration (~5 mol% = 2.6 wt%) under the inner core conditions [103,104]. Vočadlo et al.'s [103] calculations showed that the high-pressure bcc phase is dynamically stable at core temperatures, but thermodynamically less stable than the hcp phase in pure Fe. However, the addition of a few mol% Si stabilized the bcc phase relative to the hcp phase and they concluded that the bcc phase is a strong candidate for the inner core constituent phase. This is somewhat in contrast to Belonoshko et al. [29,32] who claimed that the bcc structure is more stable than the hcp structure even in pure Fe as we have seen in Fe section (Section 3.1.1). In addition, it is uncertain whether the high-pressure bcc phase is identical to the B2 phase observed in the experiments above, although the high-pressure bcc phase should take the same atomic coordinates as the B2 phase [103].

The above discussions are based on the stability of crystal structures under subsolidus conditions (see Figure 11b–d), but the liquidus phase of the outer core that crystallises to form the inner core depends on the eutectic composition. Ozawa et al. [98] placed constraints on the eutectic composition in the Fe-Si system from textural observations made on samples recovered from DAC experiments, which is compared with existing data in Figure 15 [95,97,98,100,105]. Their results show that the Si content in eutectic melt decreases with increasing pressure and is less than 1.5 ± 0.1 wt% Si at 127 GPa (Figure 15). The expected Si content in the outer core ranges from 4.5 to 11 wt% assuming that silicon is the sole light element in the core [10,88,89,96,106], in order to account for the cdd (see also the discussions about the *Vp* and density of Fe-Si liquids below). Such a Si-enriched liquid core should crystallise a less dense solid, CsCl (B2)-type phase at the ICB which would not meet the inner core density. However, the crystallization of the hcp iron phase would be possible if other light elements are present in the core to account for the cdd [98]. It would therefore be concluded that silicon cannot be the sole light element in the core.

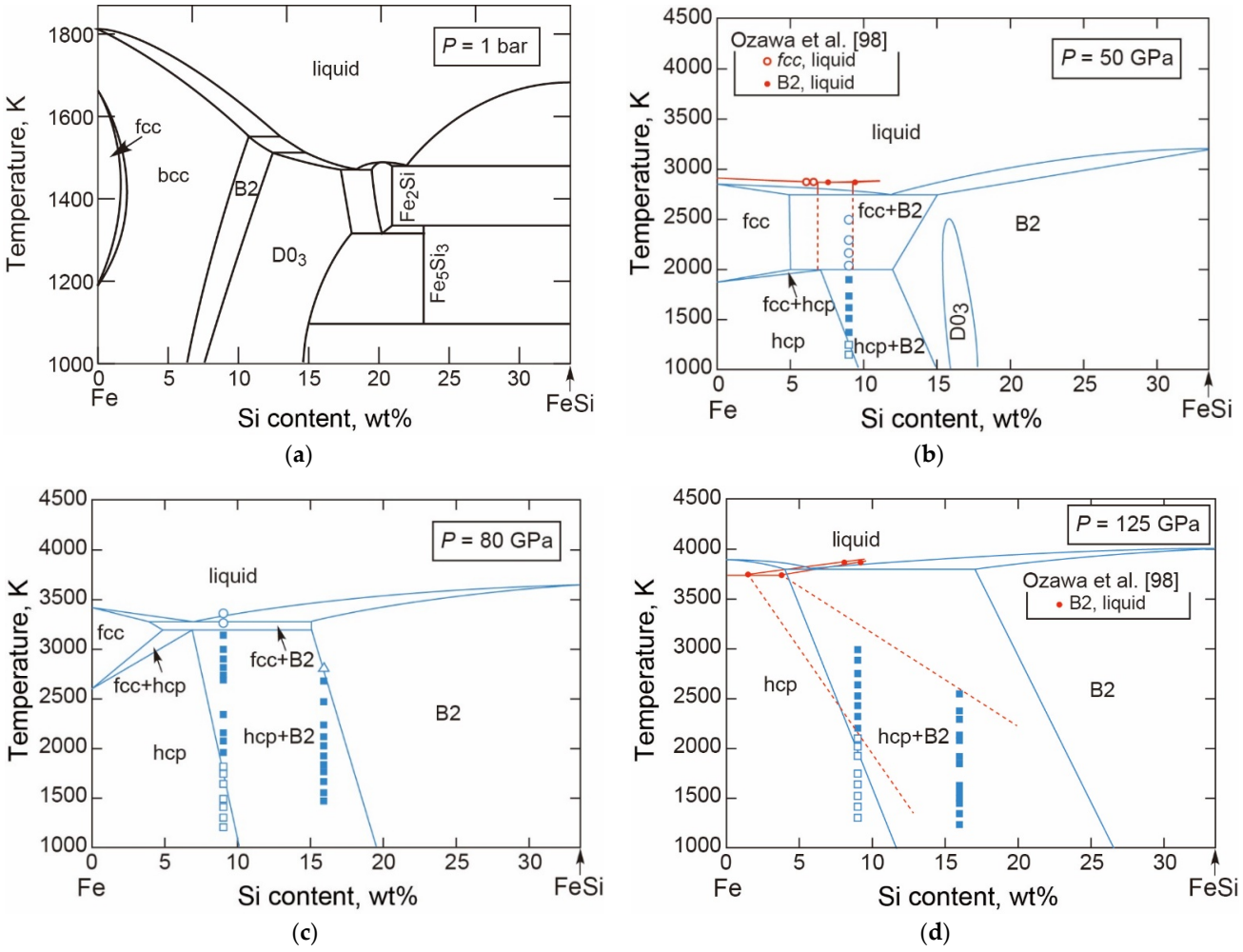


**Figure 11.** Eutectic relations in the Fe-Si system at (**a**) 1 bar, (**b**) 50 GPa, (**c**) 80 GPa, and (**d**) 125 GPa. (**a**) is from Ohnuma et al. [107], (**b**) from Fischer et al. [95] (blue) and Ozawa et al. [98] (red), (**c**) from Fischer et al. [95], and (**d**) from Fischer et al. [95] (blue) and Ozawa et al. [98] (red). For Ozawa et al.'s [98] data, the eutectic temperatures were constrained by [10]; solid lines are constrained by experimental data points, whereas the dashed lines are inferred boundaries which are drawn to be consistent with data in [95].

- **The Mixing Properties of Solutions**

Since many phases in the Fe-Si system show extensive mixing of Fe and Si, their mixing properties needs to be critically evaluated in order to understand the materials properties. The thermodynamic models established at 1 bar in metallurgy indicate that the low-pressure bcc, fcc, and liquid phases show strong negative nonideality, which stabilizes them more than what is expected from ideal mixing (e.g., [107]). Alfè et al. [90] discussed that the deviation from the ideal solution was weak in the hcp and liquid phases at low Si content under core conditions. More recently, Huang et al. [108] also reported that the mixing of Fe and Si in liquids at core pressures would be ideal from first-principles calculations. On the experimental side, Komabayashi [10] evaluated the mixing properties of the fcc and hcp phases based on the *P*-*T* locations of the fcc-hcp transition boundaries in Fe-4Si [99]. He applied the nonideal mixing model developed at 1 bar [107] and ideal mixing model to thermodynamic calculations of the transition and found that both models reproduced the experimental measurements at pressures to 40 GPa [99]. As such, it is reasonable to apply ideal mixing to the solutions in the Fe-Si system under the core *P*-*T* conditions.

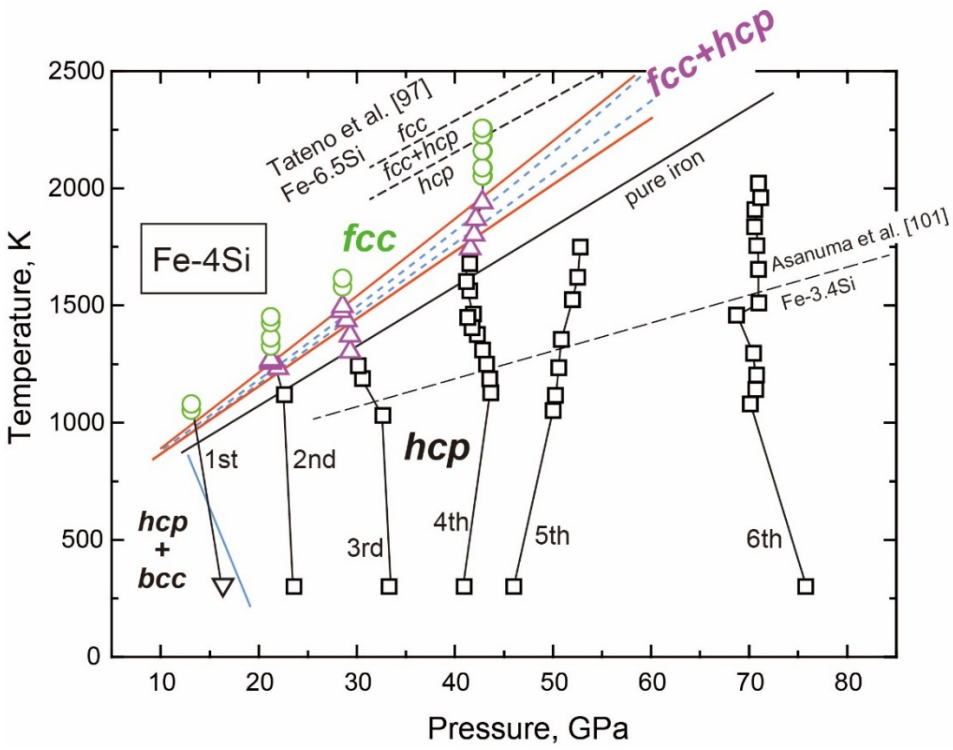


**Figure 12.** Calculated fcc-hcp transition boundaries for Fe-4Si with the ideal mixing model (red line) and nonideal mixing model (blue dashed line) [10]. Experimental results with in situ XRD in internally resistive-heated DAC are also plotted: inverted triangle, hcp + bcc; square, hcp; normal triangle, fcc + hcp; circle, fcc [99]. The transition boundaries in pure iron [14] (hcp-fcc), Fe-3.4Si [101] (hcp → hcp + fcc), and Fe-6.5Si [97] (hcp → hcp + fcc → fcc) are also shown.

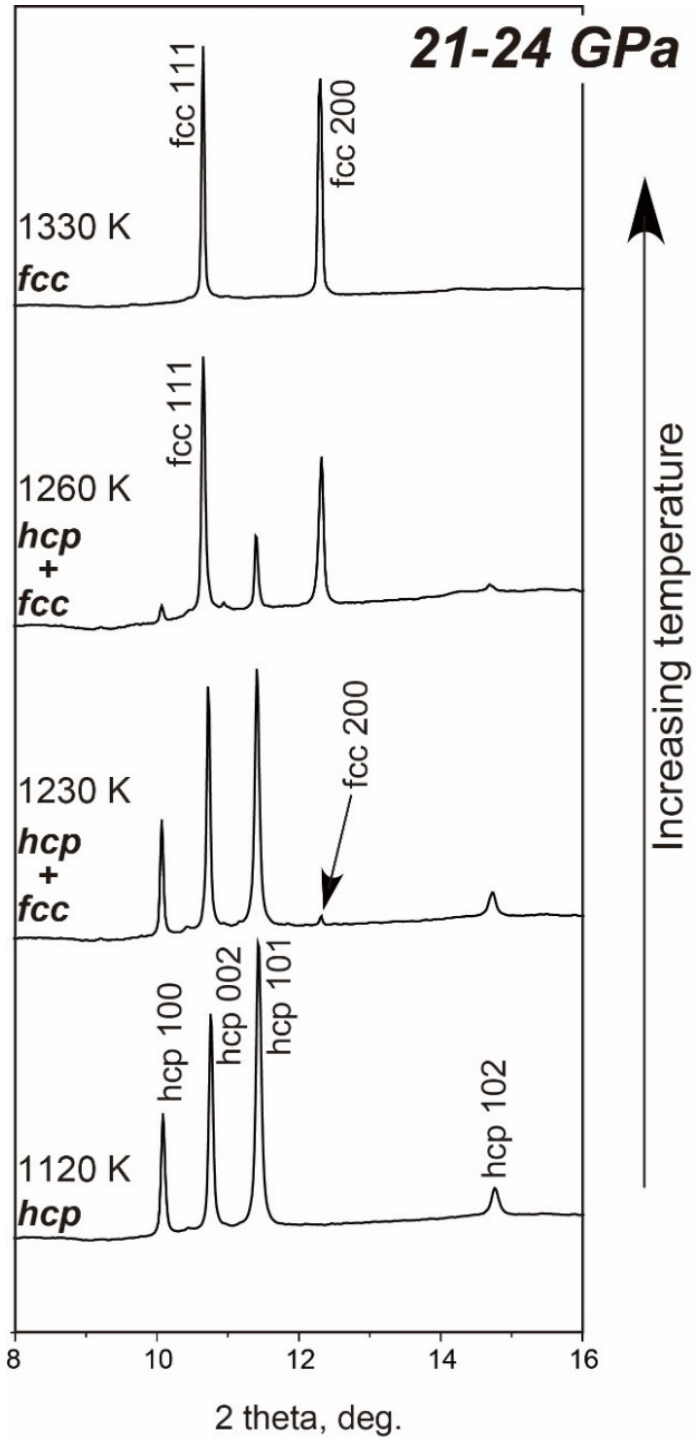


**Figure 13.** Series of XRD patterns collected in the run 2 in Figure 12 for increasing temperature [99]. The presence of the fcc phase was unambiguously marked by the appearance of (200) peak. The figure is taken after [99].

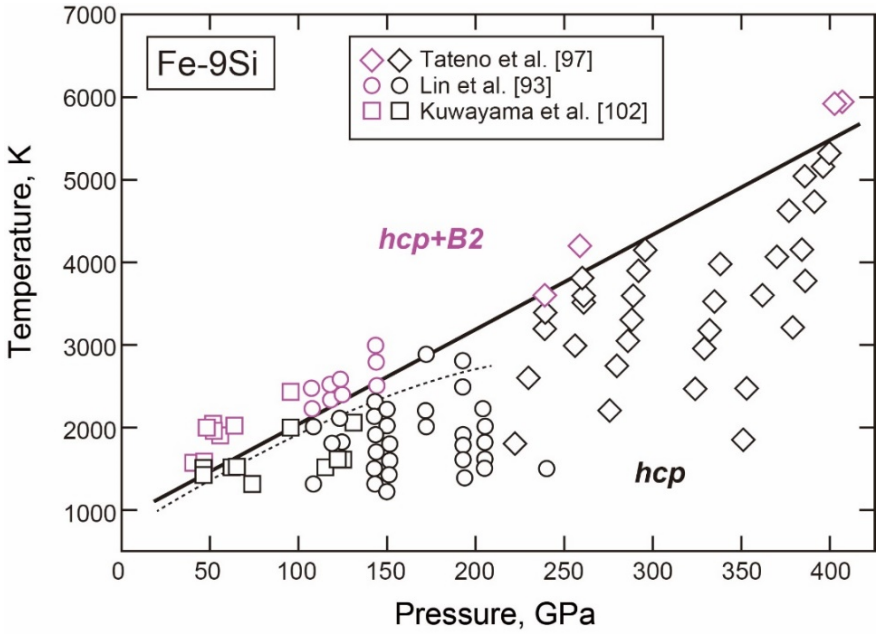


**Figure 14.** Phase boundary between hcp and hcp+B2 for Fe–9Si alloy [93,97,102]. The dotted curve is from [95]. The figure is taken after [97].

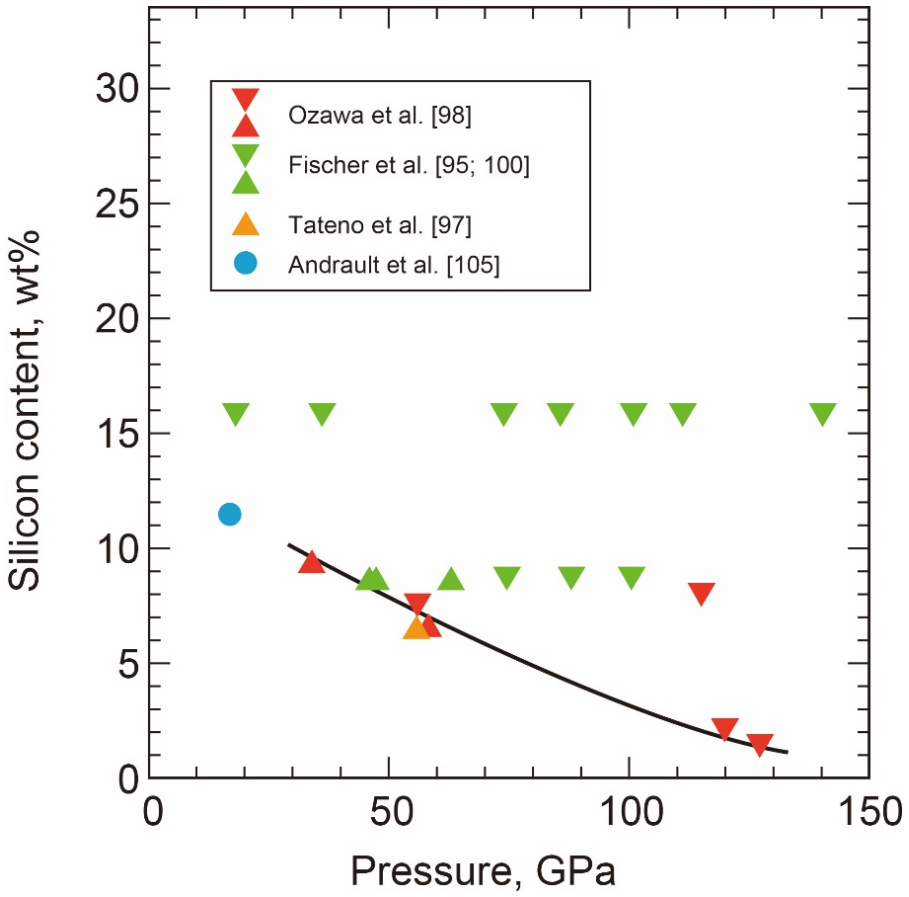


**Figure 15.** Silicon content in eutectic point as a function of pressure in the Fe–FeSi system [95,97,98,100,105]. The normal and inverted triangles denote the lower and upper bounds of the silicon content in eutectic melt, respectively. The thick black line shows the best-representative eutectic compositions [98].

- **The Melting Point at the ICB**

The melting temperature of Si-bearing iron phases (fcc and hcp) was not directly measured at pressures greater than 21 GPa [94], although high-pressure experiments observed melting of the B2 phase or eutectic of Fe + B2 in the Fe-(Ni)-Si system in the Si-rich portion of the system Fe-Si (Si > 10 wt%) [95,109–111]. There are no reports from theory on the melting point of hcp Fe-Si phases under core conditions, although Belonoshko et al. [104] reported the melting temperatures of bcc Fe and $Fe_{0.9375}Si_{0.0625}$ (Fe-3.2Si) at the ICB pressure of 7000 and 7200 K, respectively (Figure 16).

Another important melting property is the width of the melting loops of iron phases because it is the key to understanding the Si partitioning between the solid inner core and liquid outer core upon inner core crystallization [90,94,98]. At 1 bar the width of the melting loop for the bcc phase is as narrow as 2 wt% Si for Fe-5Si [107] (Figure 11a). Kuwayama and Hirose [94] suggested that the width of the melting loop for the fcc phase would be less than 2 wt% of Si at 21 GPa based on high pressure experiments performed in a multi-anvil apparatus. Recently Ozawa et al. [98] demonstrated from laser-heated DAC experiments that the fcc melting loop was as narrow as less than 1 wt% Si at 58 GPa. Alfè et al. [90] reported by first-principles calculation that silicon is almost equally partitioned between hcp iron and liquid at 370 GPa. As such the width of melting loop of the iron phases seems to become narrower with increasing pressure from 1 bar to over 3 Mbar.

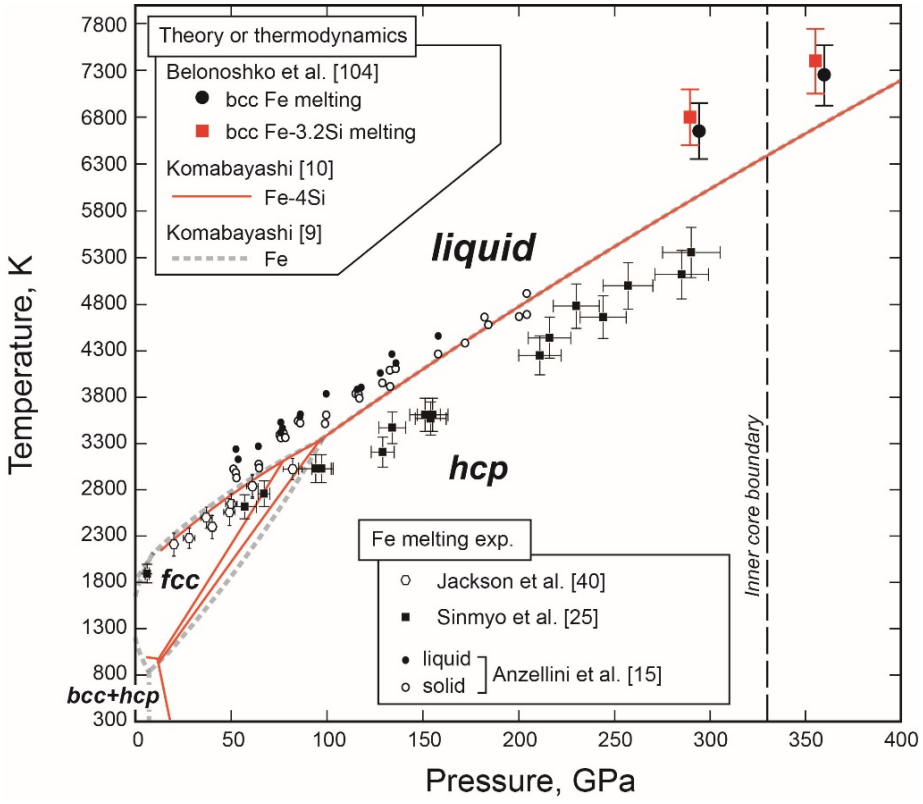


**Figure 16.** A phase diagram for Fe-4Si [10] in comparison to that of pure iron [9]. The fcc-hcp transition boundaries and melting curve of the hcp phase were calculated with ideal mixing of Fe and Si in the phases, while the other boundaries including the melting curve of the fcc phase were schematically drawn for Fe-4Si. The melting curves of fcc and hcp phases are compared with of pure Fe, namely, 20 K lower than pure iron at 60 GPa and the same as for iron above 90 GPa. Pure iron melting data are plotted [15,25,40]. The melting points of high-pressure bcc Fe and bcc Fe-3.2Si are also shown [104]. Note that the melting curve for Fe-4Si is to demonstrate that the effect of Si can be negligible. Ozawa et al. [98] reported that the silicon content in eutectic point is less than 4 wt% at pressures greater than 90 GPa (Figure 15).

Komabayashi [10] assessed the melting temperatures of Si-bearing fcc and hcp structures based on the width of the melting loops. The thermodynamic system that he considered was Fe-Si in which the hcp, fcc, and liquid phases were treated as solutions between Fe and hypothetical Si with the same structure, for example, hcp Fe and hcp Si. He assessed the melting temperature for the Si end-member ($T_{Si}^{melting}$) under high pressure, by reproducing the width of melting loops [90,98], adopting ideal mixing as discussed above. The key constraints came from that the entropy of fusion, $\Delta S^{melting}$, for both end-members (Fe and Si) are large of 7–10 J/K/mol (cf. $\Delta S_{Fe}^{fcc-hcp\ transition}$ = 3 J/K/mol at 60 GPa). With the ideal mixing model, when $\Delta S$ is large for both end-members, a phase transition loop would be wide, depending on the difference in transition temperature between the end-members, i.e., $\Delta T_{Fe-Si}^{melting}$ for the present discussion (e.g., Yamasaki and Banno [112]) (Figure 17). As such $\Delta T_{Fe-Si}^{melting}$ needs to be small in order to account for the reported narrow melting loops, namely, $T_{Si}^{melting}$, should be close to $T_{Fe}^{melting}$. When the melting phase loop was calculated to match the data by [98] at 60 GPa, $T_{Si}^{melting}$ needed to be 2600 K (Figure 18) which is only 300 K lower than $T_{Fe}^{melting}$ = 2910 K. Alfè et al. [90] concluded that Si is almost equally partitioned between solid and liquid to 20 mol% Si (11 wt% Si) at 7000 K and 370 GPa. Assuming an ideal solution for both liquid and solid, an equal partitioning of Si between solid and liquid implies composition-independent melting temperature. Thus-obtained melting curves for the hcp and fcc phases in Fe-4Si are shown in Figure 16. Note, that as discussed above, the Si content in the eutectic melt under the core conditions might be less than 1.5 wt% [98], and therefore Figure 16 is exclusively used for the effects of Si on the melting temperature of the hcp phases.

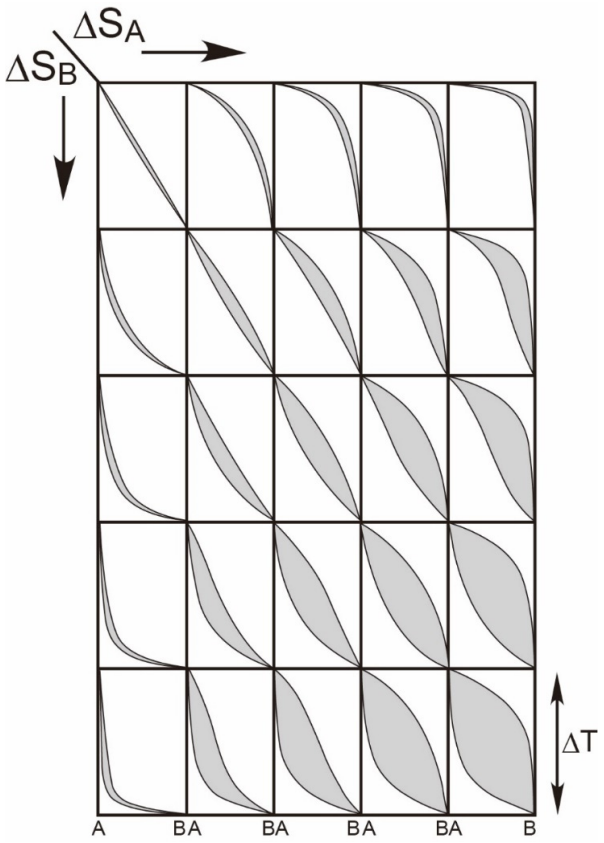


**Figure 17.** Variation in the shape of a two-phase loop in the binary AB system as a function of $\Delta S_A$ and $\Delta S_B$ (after [112]). Ideal mixing is assumed. When both $\Delta S$ are large, the loop is wide, unless $\Delta T$ is small. The figure is taken after [10].

For 1–8 wt% Si-bearing iron systems, which span the proposed values for the Si content in Earth's core [113–117], the expected change of liquidus temperature of Fe due to Si is about –50 K at 60 GPa and about 0 K at 330 GPa (Figure 16). This suggests that the addition of Si to Earth's core would not significantly affect the temperature at the ICB where the inner core is believed to be crystallised from the outer core.

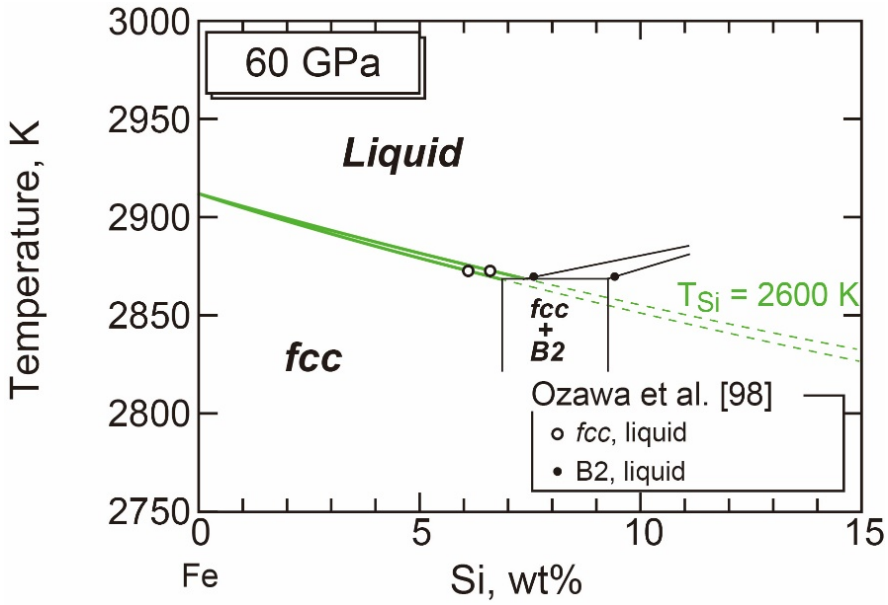


**Figure 18.** Calculated melting loop of the fcc phase at 60 GPa, with ideal mixing assumed between Fe and Si [10]. The green lines were obtained so that the calculations reproduce the reported Si partitioning data [98]. The Si partitioning data between the liquid and B2 phases are also plotted [98].

- **Liquid Properties**

From the above-constrained melting curve, Komabayashi [10] assessed thermal EoS of Si-bearing iron liquids. Figure 19a shows calculated density and *Vp* for an Fe-4Si outer core along its isentrope together with results of first-principles calculations [88,89], inelastic X-ray scattering experiments [118], and PREM [51]. Note that the Si contents in Komabayashi [10], Badro et al. [88], and Nakajima et al. [118] in Figure 19a are not meant to be best-fits to the PREM while that in Ichikawa and Tsuchiya's [89] calculations is the best-fit composition in the binary Fe-Si. All four the models show that the addition of silicon increases the velocity. However, the effects of silicon on the bulk modulus of liquid iron are in contrast between the experiment-based [10] and theory-based models [88,89] (Figure 19b). As discussed in the case of Fe-FeO (Section 3.2.1), the compressibility of a liquid should be close to that of the counterpart crystalline phase under core pressure. The EoS parameters for the Fe-Si hcp phase in Komabayashi [10] was based on compression experiments on the hcp phase by Tateno et al. [97] to 305 GPa who demonstrated that the addition of silicon surely increases the bulk modulus of hcp iron. Komabayashi [10] provided a set of EoS for the solids and liquids in the Fe-Si system while the first-principles calculations have not, the same as in the case of oxygen (see, Section 3.2.1. Fe-O).

Any of Badro et al. [88], Ichikawa and Tsuchiya [89], and Komabayashi's [10] models in Figure 19a require a Si content greater than 4 wt% to make the density and *Vp* profiles match the PREM. However, as discussed above, the Si content in the eutectic melt at the ICB is expected to be less than 1.5 wt% [98]. Therefore, the crystallising phase from such an outer core is likely the B2 phase, which should be less dense than the inner core. On the other hand, recent experimental measurements by Nakajima et al. [118] showed that the addition of Si to iron liquid produced an enhanced increase in the *Vp* and moderate reduction in density, which implies that the addition of Si alone cannot account for the

observed seismic properties of the outer core. As such, all the *Vp*-density modelsplotted in Figure 19a suggest that silicon cannot be the sole light element in Earth's core.

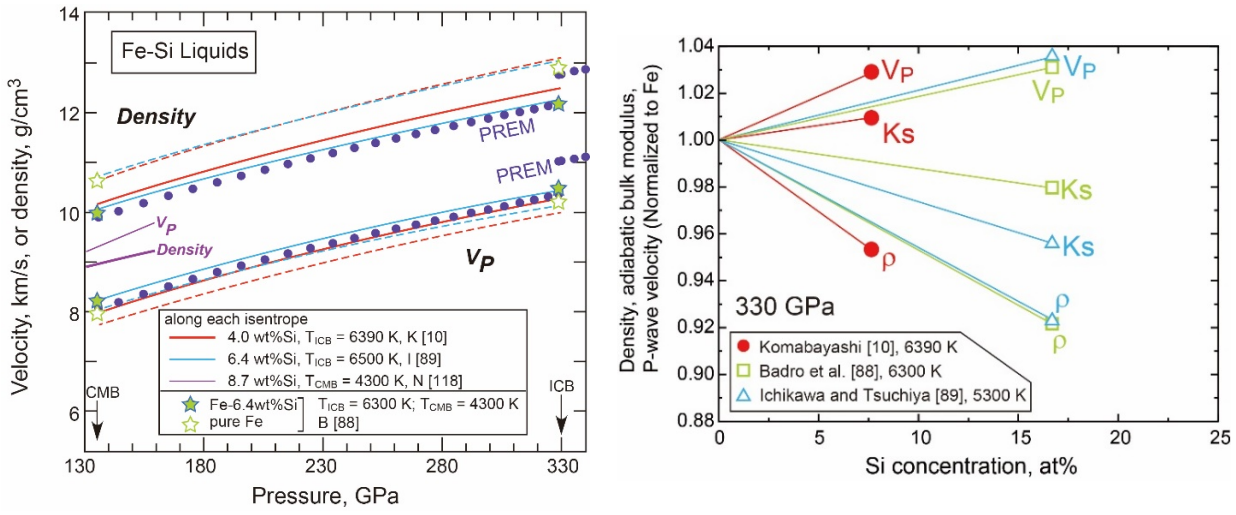


**Figure 19.** (**a**) *Longitudinal* wave velocities (*Vp*) and densities of Fe-Si liquids: Fe-4Si (Komabayashi [10]), Fe-6.4Si (Ichikawa and Tsuchiya [89]), Fe-6.4Si (Badro et al. [88]), and Fe-8.7Si (Nakajima et al. [118]). Each profile is along its isentrope. For comparison, pure iron data are plotted (red dashed line with $T_{ICB}$ = 6382 K, Komabayashi [9]; blue dashed line with $T_{ICB}$ = 6000 K, Ichikawa et al. [50]). (**b**) Effects of silicon on the *Vp*, adiabatic bulk modulus (*Ks*), and density (*ρ*) of liquid iron at 330 GPa [10]. Data from the first-principles studies are compared [88,89]. Note that the parameters are normalized to those for pure iron.

### 3.2.3. Fe-S

Of the candidate elements to account for the cdd, sulphur has been most extensively studied [119]; the Fe-S system is still currently of significant interest as new discoveries are being reported [120–125].

- **The *T-X* Relations**

The 1-bar phase relations of the Fe-S system include many intermediate compounds (e.g., [126]) and these compounds show a series of phase changes under pressures [127,128] (Figure 20). Above 21 GPa the sulphide phase stable with Fe under subsolidus conditions is $Fe_3S$ which takes a tetragonal system [128] forming a simple eutectic system [124,129] (Figure 20d).

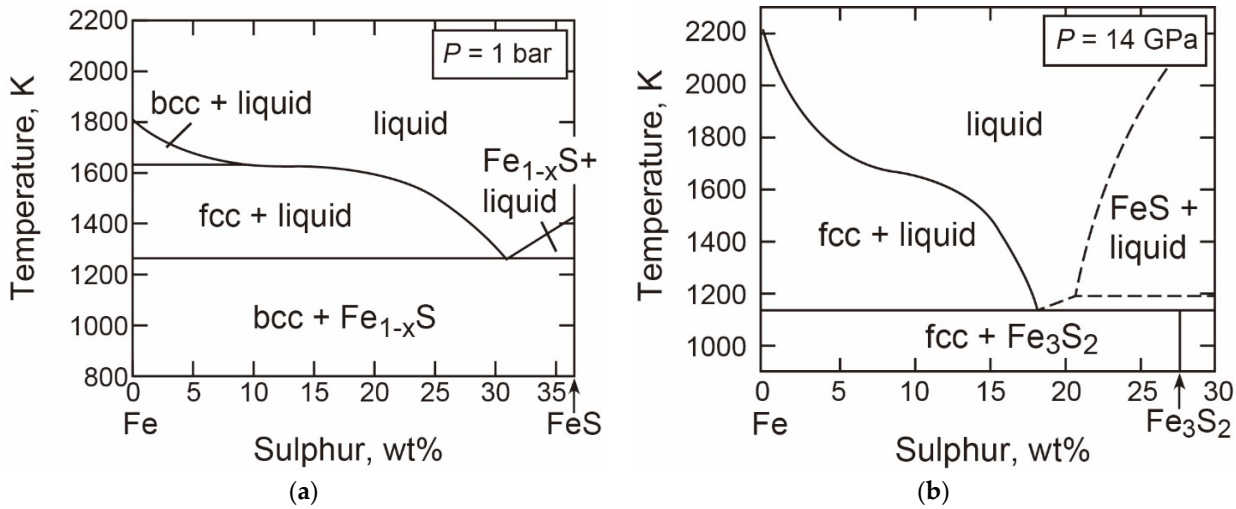


**Figure 20.** *Cont.*

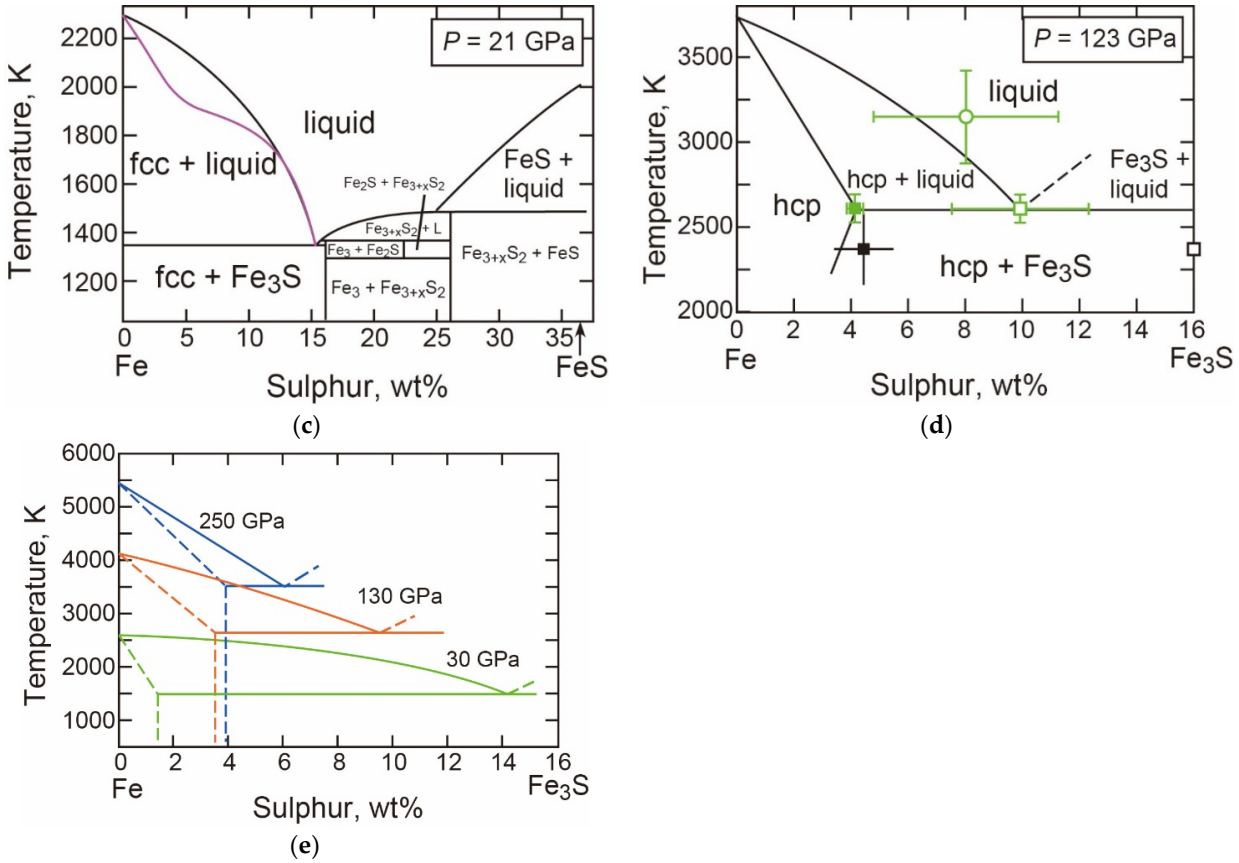


**Figure 20.** Experimentally constrained eutectic relations in the Fe-S system at (**a**) 1 bar, (**b**) 14 GPa, (**c**) 21 GPa, and (**d**) 123 GPa. Calculated eutectic relations are shown in (**e**) [122]. (**a**) is from Waldner and Pelton [126], (**b**) from Chen et al. [127], (**c**) from Fei et al. [128] (black line) and Pommier et al. [125] (purple line), and (**d**) from Kamada et al. [124]. In (**b**), the dashed lines were not directly constrained by [127]. In (**d**), the green open circle denotes total melting, green solid and open squares are eutectic solid and liquid, and black solid square denotes the subsolidus assemblage of hcp Fe and $Fe_3S$.

The eutectic composition and temperature as a function of pressure were experimentally examined [122,124,128–132] (Figure 21). Experiments also confirmed the stability of $Fe_3S$ to 250 GPa (Figure 20e). The eutectic composition becomes Fe-richer with increasing pressure to 6 wt% S at 250 GPa (Figure 21a). The eutectic temperatures were also constrained to 250 GPa [122,124,128,130,132,133] (Figure 21b). Considering the experimental uncertainties, the eutectic temperatures do not differ much between the Fe-FeO and Fe-$Fe_3S$ systems at the core pressures (Figure 21b).

The *T*-*X* liquidus curve of the Fe phases at 1 bar shows a sigmoidal shape. This is due to the nonideality of liquids and was also confirmed at 14 GPa [127] (Figure 20b). Although Fei et al. suggested a parabolic-shaped liquidus curve at 21 GPa, a recent study by Pommier et al. [125] reported a sigmoidal liquidus curve, which indicates that the nonideality still remains at this pressure (Figure 20c). There are no reports on the shape of the liquidus curve of the Fe phases at greater pressures.

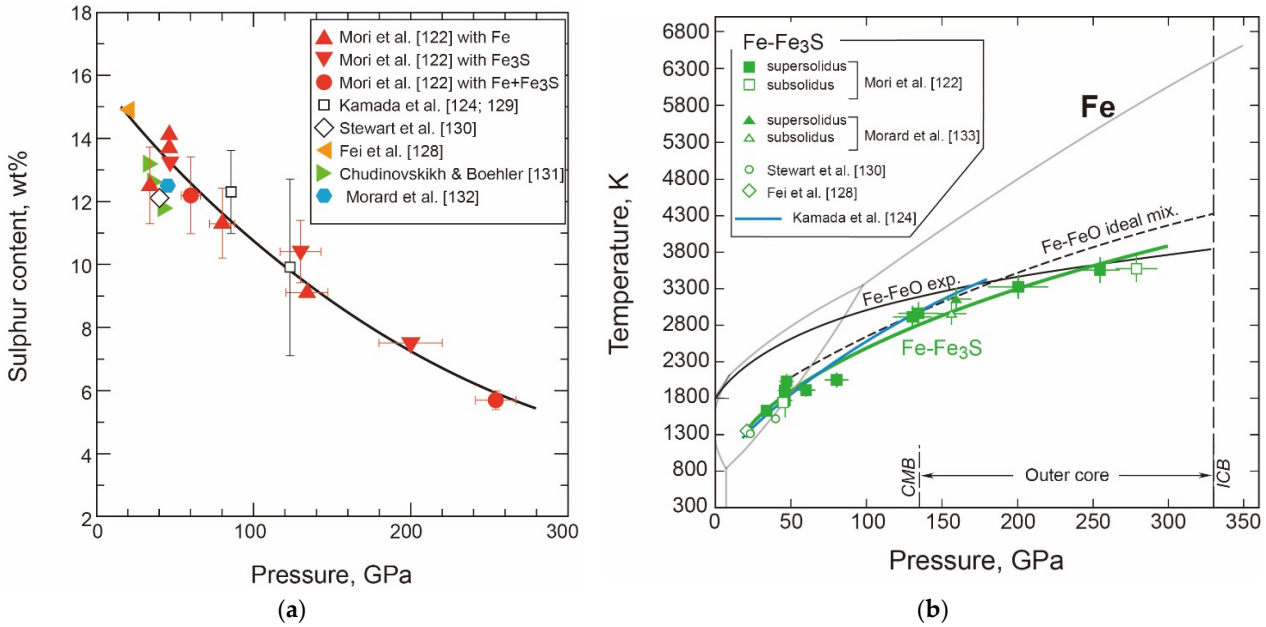


**Figure 21.** (**a**) Sulphur content in eutectic melt as a function of pressure in the Fe-S system [122,124,128–132]. (**b**) Eutectic temperatures of the Fe-S system [122,124,128,130,133] in comparison with Fe-FeO by experiment [85] and thermodynamic calculation with ideal mixing for liquids [9].

- **Sulphur in the hcp Phase**

The sulphur content in hcp Fe coexisting with a liquid needs to be critically assessed because a S-rich hcp phase could be a main constituent phase of the inner core [90]. Experimental data cover a pressure range to 250 GPa, which show that the sulphur content in the hcp phase increases with pressure [122,124,129,130,134] (Figure 22a). Figure 22b shows partitioning of S between solid (hcp) and coexisting liquid in experiments by Mori et al. [122] compared with a prediction from the first-principles calculations at 330 GPa [90]. The experimental data are approaching the theoretical value for 330 GPa with increasing pressure; the data at 254 GPa is very close to the predicted curve. Thus, a significant amount of sulphur can be incorporated in the hcp phase at the ICB conditions.

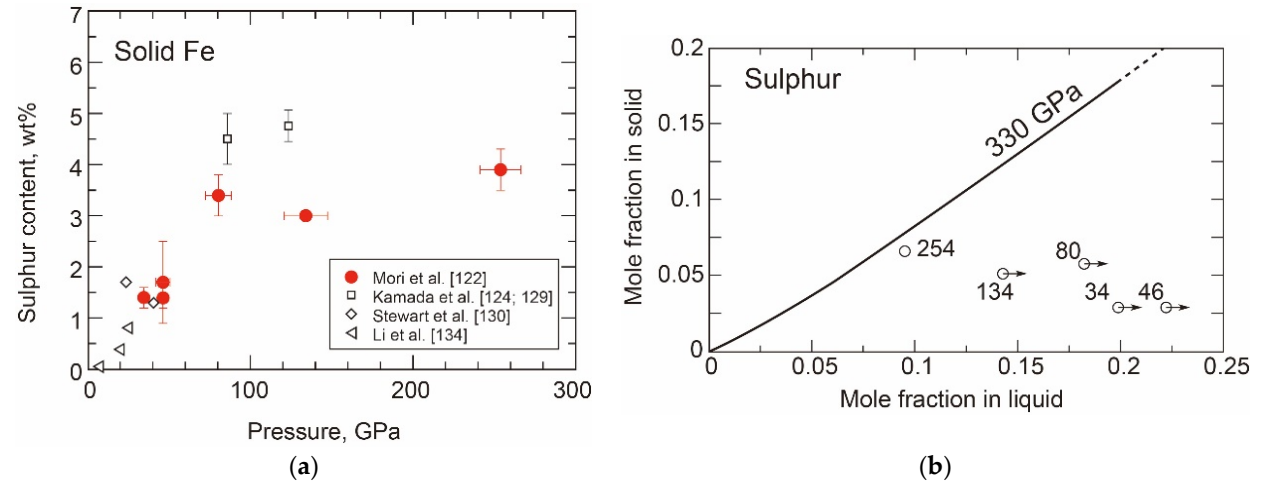


**Figure 22.** (**a**) Sulphur content in solid iron phases [122,124,129,130,134]. (**b**) Sulphur partitioning between solid iron and liquid. The black line is a result of the first-principles calculations for 330 GPa by Alfè et al. [90]. The circle symbols are experimental data and the numbers attached are the experimental pressures [122]. The small arrows attached to circles indicate the lower bounds of sulphur content in the iron phases.

- **The Properties of $Fe_3S$**

Since the $Fe_3S$ phase is stable over 200 GPa as an end-member of the subsystem Fe-$Fe_3S$ (Figure 20), constraining its physical properties provides vital information about a hypothetical sulphur-bearing core. The EoS of $Fe_3S$ has been experimentally examined with in situ XRD [128,135–138]. The 300-K EoS was well constrained thanks to the wide pressure range covered up to 200 GPa [135–138] (Figure 23a). In contrast, the thermal parameters were less studied [135,137,138]. The most recent high-$T$ data were reported by Thompson et al. [138] who proposed a thermal EoS from laser-heated DAC experiments with in situ XRD to 126 GPa and 2500 K. Figure 23b shows compression curves of $Fe_3S$ calculated with the EoS by Thompson et al. [138] and Kamada et al. [136]. The EoS by [138] calculates the density of solid $Fe_3S$ greater than by [136] since Kamada et al. [136] adopted the large $\alpha K_T$ value (0.011 GPa/K) proposed by Seagle et al. [135].

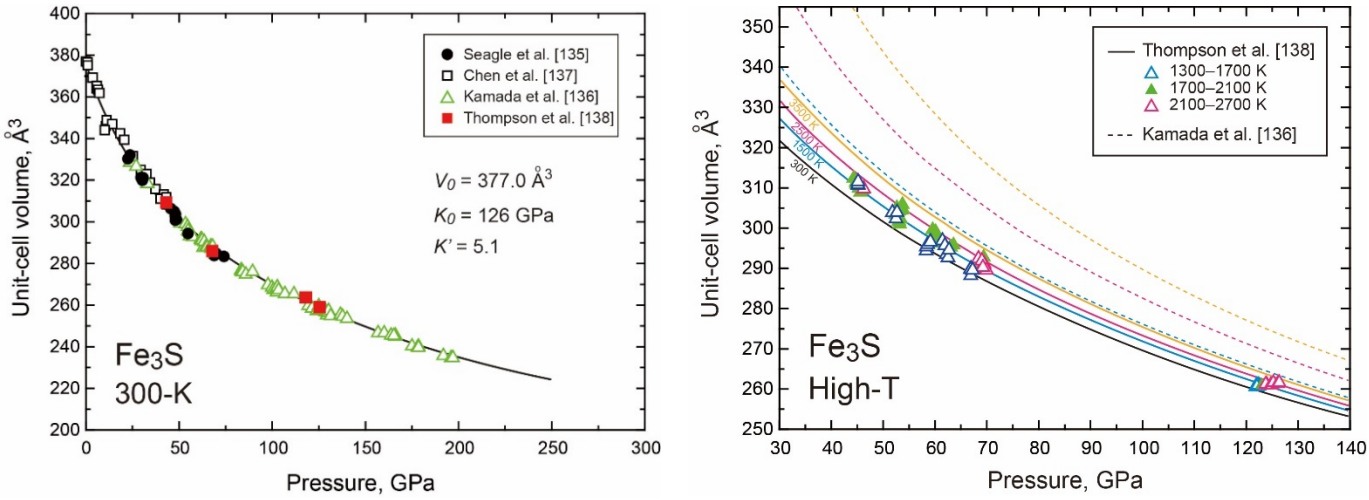


**Figure 23.** (**a**) Unit-cell volumes for $Fe_3S$ at 300 K (Seagle et al. [135]; Chen et al. [137]; Kamada et al. [136]; Thompson et al. [138]). A compression curve based on the BM EoS (Equation (1)) fitted to all the data is also shown. (**b**) Unit-cell volumes for $Fe_3S$ under high temperatures [138]. Compression curves based on the thermal EoS constructed by [138] are shown together with those by [136]. The figures are from [138].

- **Decomposition of $Fe_3S$ at Core Pressures**

Solid $Fe_3S$ is stable to 250 GPa and therefore its elastic parameters can be used to assess the liquid properties in the future. However, it undergoes a decomposition reaction into an Fe-rich hcp phase and a S-rich B2 phase at higher pressures, and therefore, the most Fe-rich sulphide phase stable in the inner core conditions would be the B2 phase, not $Fe_3S$ [121].

The nature of the reaction,

$$Fe_3S = \text{Fe-rich hcp} + \text{S-rich B2} \quad \text{(R1)}$$

was examined by Thompson et al. [138], assuming the composition of the hcp and B2 phases to be pure Fe and $Fe_2S$, respectively [121,123]. Figure 24a plots the average atomic volumes for Fe and $Fe_3S$ at 250 GPa and 300 K, based on which the volume for $Fe_2S$ is estimated. The average atomic volume for the B2 phase needs to be below the Fe-$Fe_3S$ line (Figure 24a), because a first-order pressure-induced transition must be accompanied with a volume reduction. Thompson et al. [138] considered two possible cases: (i) the volume change of the reaction ($\Delta Vr$) of $Fe_3S$ = Fe + $Fe_2S$ is zero, and (ii) $\Delta Vr = -1.5\%$. The volume for $Fe_2S$ is then obtained for each case in Figure 24a. Recently, Tateno et al. [123] reported experimental data on the unit-cell volume of the $Fe_2S$ phase at pressures greater than

180 GPa. Their volume of $Fe_2S$ is plotted in Figure 24a, with their experimental pressure values corrected to be consistent with the pressure scale in [138]. Tateno et al.'s [123] data shows 1.0% volume reduction on reaction (R1), which is within the predicted range by [138] (Figure 24a). Thompson et al. [138] estimated compression curves for $Fe_2S$ with evaluating EoS parameters (Figure 24b).

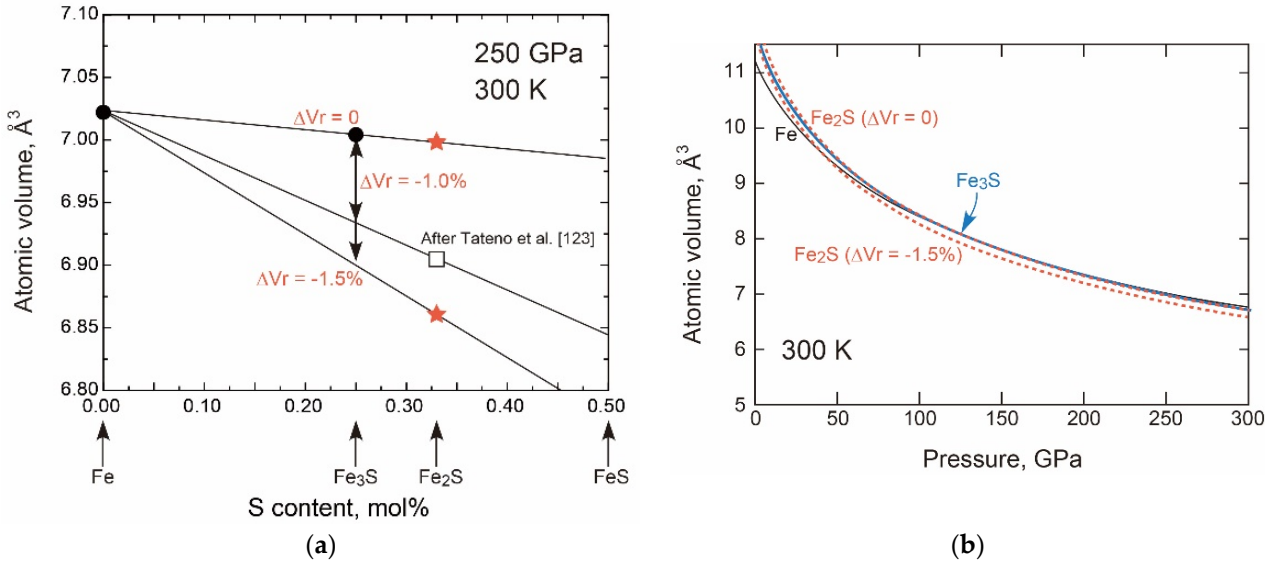


**Figure 24.** (**a**) Volume relationships for reaction (R1) [121]. The composition of the hcp phase is assumed to be pure Fe. The volumes were calculated from Dewaele et al. [4] for Fe and Thompson et al. [138] for $Fe_3S$. The star represents a hypothetical B2 phase with a composition of $Fe_2S$ [121]. The volumes of the hypothetical $Fe_2S$ phase were estimated for the cases of $\Delta Vr = 0$ and $-1.5\%$, respectively. The open square indicates the volume of $Fe_2S$ constrained by experiment [123]. (**b**) Compression curves of the hypothetical $Fe_2S$ at 300 K. The figures are from [138].

- **Thermodynamic Model of the System**

The thermodynamics of the Fe-S system at 1 bar has been well studied [126,139–142]. The system is characterized by the liquid phases showing negative nonideality over the entire compositional range. The most recent study treated the liquid phases with the quasi-chemical model [126]. Solid $Fe_3S$ was not included in those models as it is only stable at high pressures ($P > 20$ GPa). The nonideality under high pressure can be discussed from the shape of the liquidus curve of the Fe phases. At 1 bar to 20 GPa, experiments confirmed that the liquidus curves are sigmoidal shaped, which implies that the nonideality continues to those pressures [125–127]. There is no information about the nonideality of liquids under greater pressures.

Saxena and Eriksson [143] established a model for calculations of high-*P*-*T* phase relations including $Fe_3S$. The calculated eutectic composition at the ICB is Fe-10S, which is more S-enriched than the recent experimental determination by Mori et al. [122] (Figure 21a), but they are qualitatively consistent as for the pressure dependence of the sulphur content in eutectic melt, namely it is decreasing with increasing pressure [143].

Future models should include the recent experimental data: the updated EoS for $Fe_3S$ [138], eutectic compositions to 250 GPa [122], and the breakdown reaction of $Fe_3S$ into Fe(+S) hcp +$Fe_2S$ [121]. Integrating these new data will make the model more robust and enable us to assess the liquid EoS to compare with the outer core PREM.

- **Density of Fe-S Liquids and Solids in the Core**

Figure 25a shows density profiles of solid $Fe_3S$ from the EoS by [138] at 300, 4000, and 5500 K compared with the PREM over the core pressure range. The density of solid $Fe_3S$ at 300 K is calculated to be smaller than the inner core PREM (Figure 25a). As the compression behaviour of $Fe_3S$ at 300 K is well constrained to 200 GPa [135–138], the uncertainty of the

calculated unit-cell volume when extrapolated to 330 GPa is ±0.2%. This ensures that solid $Fe_3S$ is less dense than the inner core under core temperatures.

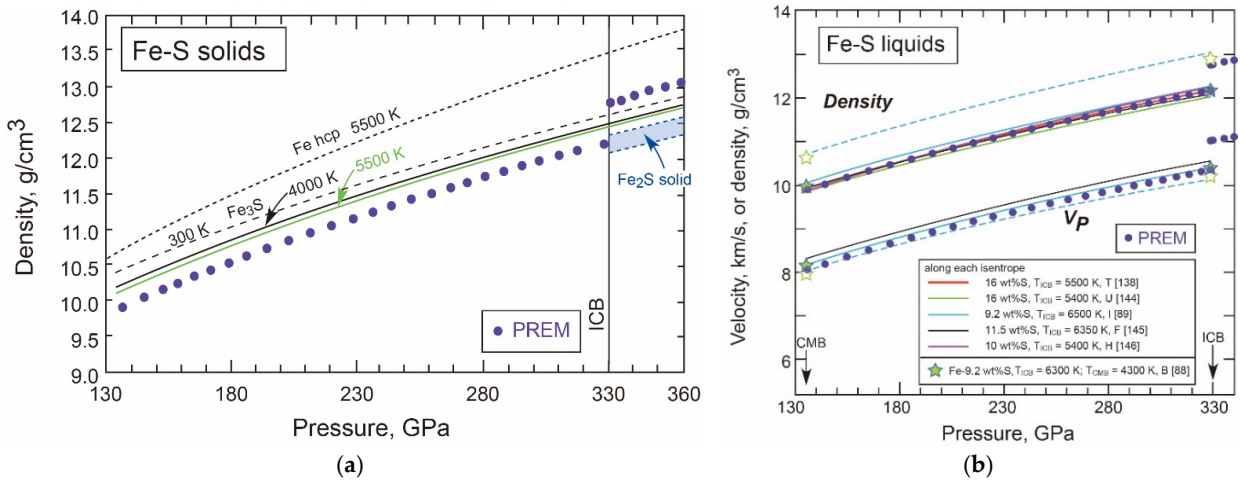


**Figure 25.** (**a**) Isothermal density profiles of solid $Fe_3S$ based on [138] at 300 (black dashed), 4000 (black solid), and 5500 K (green solid), compared with a compression profile of hcp Fe [4] along a 5500 K isotherm and the PREM profiles [51]. An estimated density range of $Fe_2S$ B2 phase at the inner core pressures and 5500 K is shown: the lower and upper bounds are for $\Delta Vr$ (R1) = 0 and −1.5% respectively. (**b**) Density and *Vp* for Fe-S liquids over the outer core pressure range together with the PREM data. The density of liquid $Fe_3S$ (Fe-16S) estimated from that of solid $Fe_3S$ is from Thompson et al. [138]. Results from the first-principles calculations are also shown (Badro et al. [88]; Umemoto et al. [144]; Ichikawa and Tsuchiya [89]; Fu et al. [145]). The green open stars denote the pure Fe properties by [88]. Results for the density measurements of a shock wave compression study (Huang et al. [146]) are also plotted. Isentropic profiles of liquid Fe are also shown (dashed blue lines, Ichikawa et al. [50]) from Figure 3.

Data of Fe-S liquids are summarized in Figure 25b including estimates based on solid compression data [138], first-principles calculations [88,89,144,145], and shock compression experiments [146]. Thompson et al. [138] estimated the density profile of liquid $Fe_3S$ by assuming a $\Delta V$ upon melting ($\Delta Vm$) for $Fe_3S$ to be the same as for pure iron at core pressures, and assuming a temperature gradient by 1500 K through the outer core, which means 4000 K at 140 GPa and 5500 K at 330 GPa. This temperature gradient is consistent with the Grüneisen parameter of pure Fe of about 1.5 [9,147]. Thus-calculated density profile for liquid $Fe_3S$ matches the outer core density within an uncertainty of 1% (Figure 25b). As such, the sulphur content in the outer core needs to be as much as 16 wt% (=$Fe_3S$) if it is the sole light element in the core [138]. This estimate can be improved by refining the values of $\Delta Vm$ and the isentropic temperature gradient over the outer core.

Using first-principles calculations, Umemoto et al. [144] calculated the density of $Fe_3S$ liquid along an isentrope with 5400 K at 330 GPa, which agrees with the PREM density of the outer core and the estimated $Fe_3S$ liquid density by [138]. Ichikawa and Tsuchiya [89] provided the best-fit value of sulphur content in the outer core of 9.2 wt%. Badro et al.'s [88] calculations also showed that 9.2 wt% sulphur would make the liquid *Vp* and density match the PREM (Figure 25b). A shock compression study reported that the density of Fe-10S along an isentrope with $T_{ICB}$ = 5400 K would match the PREM [146]. As such, the estimated sulphur content in the outer core based on density ranges from 9.2 to 16 wt%, which could be narrowed down if all the density profiles were set at the same $T_{ICB}$. More data from different approaches are needed to constrain the *Vp*.

Liquid cores with compositions of Fe-9.2S or Fe-16S would crystallise a sulphide since the eutectic composition in the Fe-$Fe_3S$ sustem was reported to become close to the Fe side with increasing pressure [122] (Figure 21a). On the other hand, as we discussed above, crystalline $Fe_3S$ may not be stable under inner core conditions as it would break down to a mixture of Fe-rich hcp phase and S-rich B2 phase above 250 GPa [121]. This results in

a formation of the S-rich B2 phase from a liquid with S > 6 wt% at ICB. Assuming that the B2 phase has a composition of $Fe_2S$ and causes $\Delta Vr = 0$ to $-1.5\%$ as discussed above (Figure 24a), the density profile of B2 $Fe_2S$ for the inner core range is calculated along a 5500 K isotherm (Figure 25a). The density of $Fe_2S$ is likely less dense than solid $Fe_3S$ and cannot match Earth's inner core density. As such, the liquidus phase for Fe-9.2S to Fe-16S is not the constituent phase of the inner core. In summary, while the outer core density requires as much sulphur as 9–16 wt%, the resulting liquidus phase cannot meet the density of the inner core.

#### 3.2.4. Fe-C

The phase relations in the Fe-C system at 1 bar were extensively studied as it is a fundamental system in steelmaking. High-pressure phase diagrams were constructed to 13 GPa in the late 1960s [148,149]. In Earth science, a pioneering work on the phase relations which can be applicable to core conditions was made by Wood [150] who employed thermodynamic calculations to 330 GPa based on available experimental data including melting data to 5 GPa and thermoelastic properties of Fe-C phases. His calculations showed that the eutectic composition was very close to the Fe end-member (0.9 wt% C) at 330 GPa and solid $Fe_3C$ may compose the inner core. Later experiments, up to 29 GPa, confirmed that $Fe_7C_3$ would be the first phase to crystallize out of a carbon-rich liquid core [151] which reinforced earlier results of the stability of $Fe_7C_3$ under high pressure [149]. Here I review *T*-*X* phase relations, stability relations of $Fe_3C$ and $Fe_7C_3$, and liquid properties.

- **The *T*-*X* Relations**

Figure 26 summarises *T*-*X* relations in the Fe-rich portion with increasing pressure [150–154]. At 1 bar, the steelmaking industry prefers to show both stable and metastable reactions (Figure 26a) because the free energy difference between them is so small and one would encounter both reactions in an experiment [155]. Under high pressure, for example, 5 GPa (Figure 26b), $Fe_3C$ is a stable phase and the phase diagram is unambiguous. A high-pressure phase $Fe_7C_3$ appears above 9 GPa, which makes $Fe_3C$ melt incongruently [149,151] (Figure 26c). The phase relations at core pressures (Figure 26d,e) are based on thermodynamic calculations [150,154,156] and experiments [156].

The eutectic point is at Fe-4.2C at 1 bar and its carbon content may or may not change with increasing pressure (Figure 27a). At the ICB pressure, while the recent thermodynamic model predicted it to be around 2 wt% [154], experiments in laser-heated DAC combined with chemical analysis on recovered samples showed that almost constant eutectic compositions with 3.6–4.5 wt% C at 23–255 GPa [156]. On the other hand, the eutectic temperatures are consistent between different studies at least up to 70 GPa [85,154,156,157] (Figure 27b).

- **Carbon in the hcp Phase**

Carbon dissolves into the crystal structure of iron. The maximum carbon concentration in bcc iron at 1 bar is about 0.02 wt% at 1010 K [152], which increases in fcc iron to about 2.00 wt% [152], and decreases with increasing pressure [158]. Mashino et al. [156] showed that carbon content in solid hcp iron remains in the order of 1 wt% up to 255 GPa (Figure 28).

From first-principles calculations, Caracas [159] found that the density deficit of the inner core can be matched for 1–2.5 wt% carbon in hcp Fe, depending on the thermal profile. This is consistent with an experimental investigation by Yang et al. [160] who made compression experiments in DAC and showed that 1.30 and 0.43 wt% carbon may explain the inner core density deficit at 5000 K and 7000 K, respectively. As such the carbon content in hcp iron required for the 4% cdd at 6000 K is only 1–2 wt% because incorporation of carbon in the hcp structure expands the volume [160]. Such C-bearing hcp phases can directly crystallise out of an Fe-C outer core as the eutectic composition would be at 2–4 wt% C at the ICB as discussed above [154,156], depending of the carbon content in the outer core, which will be discussed later.

- **The Properties and Decomposition of $Fe_3C$ at Core Pressures**

Figure 26d,e show that $Fe_3C$ is destabilised between 136 and 330 GPa according to the thermodynamic model by [154], which has an impact on the liquidus phase field adjacent to the eutectic point, namely from $Fe_3C$ to $Fe_7C_3$. Since $Fe_3C$ and $Fe_7C_3$ phases have different carbon contents, thermoelasticity, and physical properties, their stability relations are critically important for models of a carbon-bearing inner core. Both of these iron carbides have been shown to plausibly match some solid-state physical properties of the inner core, such as shear wave velocity and Poisson's ratio [161–165]. As Fei and Brosh's [154] model was focused on melting relations, I here review the subsolidus relations regarding stability of $Fe_3C$ examined by experiment and first-principles calculation.

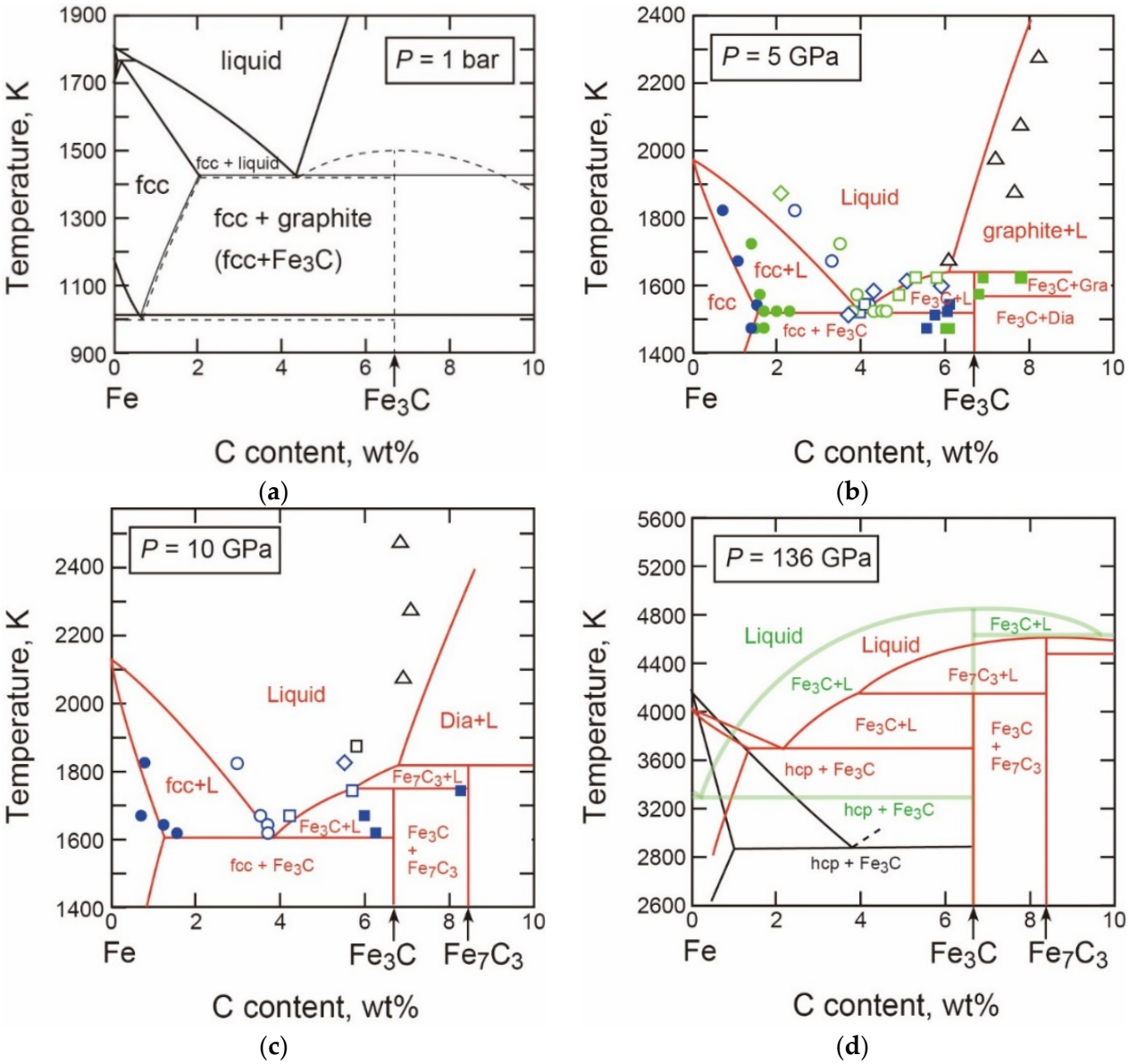


**Figure 26.** *Cont.*

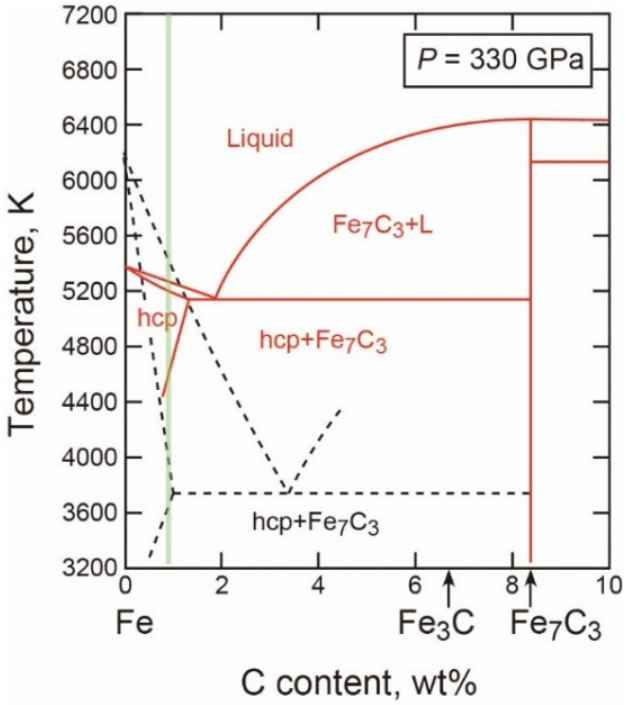


(**e**)

**Figure 26.** Eutectic relations in the Fe-C system at (**a**) 1 bar, (**b**) 5 GPa, (**c**) 10 GPa, (**d**) 136 GPa, and (**e**) 330 GPa. (**a**) is after Gustafson [152], and the red lines in (**b**–**e**) are calculated by Fei and Brosh [154]. The green and black lines in (**d**) are calculated by Wood [150] and are based on experiments by Mashino et al. [156], respectively (the dashed curve is inferred). The black dashed lines in (**e**) are inferred from thermodynamic calculations by [156]; the green line in (**e**) indicates the eutectic composition by [150]. In (**a**), the solid lines are equilibrium lines and dashed lines are metastable lines. Both phase relations are encountered in experiments [155]. In (**b**,**c**), the symbols are experimental data: blue [154]; green [153]; black [151]. The solid circles denote the compositions of solid iron coexisting with either melt or $Fe_3C$. The open circles denote the compositions of melt coexisting with solid iron. The solid squares represent the compositions of iron carbides ($Fe_3C$ or $Fe_7C_3$). The open squares represent the compositions of melt coexisting with iron carbides. The open diamonds show that only melt was observed. The open triangles show the melt compositions coexisting with either graphite at 5 GPa or diamond at 10 GPa.

The key reaction is,

$$3Fe_3C = Fe_7C_3 + 2Fe \quad \text{(R2)}$$

which is an equilibrium univariant reaction. This was first inferred by Lord et al. [166] from the topology of high-pressure melting curves of $Fe_3C$ and $Fe_7C_3$. Reaction (R2) was later examined in laser-heated DAC with in situ XRD by Liu et al. [157], who placed its boundary at about 150 GPa (Figure 29a). This observation is contradicted, however, by Tateno et al.'s [23] in situ XRD measurements of the formation of $Fe_3C$ phase in their Fe sample in the DAC upon laser heating at about 340 GPa. More recent in situ XRD experiments also observed $Fe_3C$ to pressures greater than 250 GPa [167] (Figure 29b). Mookherjee et al. [168] reported that $Fe_3C$ was energetically stable at all pressures to the centre of the Earth from first-principles calculations on reaction (R2) at $T = 0$. On the other hand, Mashino et al. [156] reported the $Fe_3C$ phase as a liquidus phase in their melting experiments in the Fe-C system to 203 GPa, but placed the possible occurrence of reaction (R2) at 255 GPa from chemical and textural analyses of recovered samples (Figure 29b). McGuire et al. [169] made thermodynamic calculations on the *P*-*T* locations of reaction (R2) using their newly established EoS for $Fe_3C$. The reaction is located at 87 GPa and 300 K and 251 GPa and 3000 K and its boundary is consistent with the results of both Tateno et al. [23] and Mashino et al. [156] (Figure 29b).

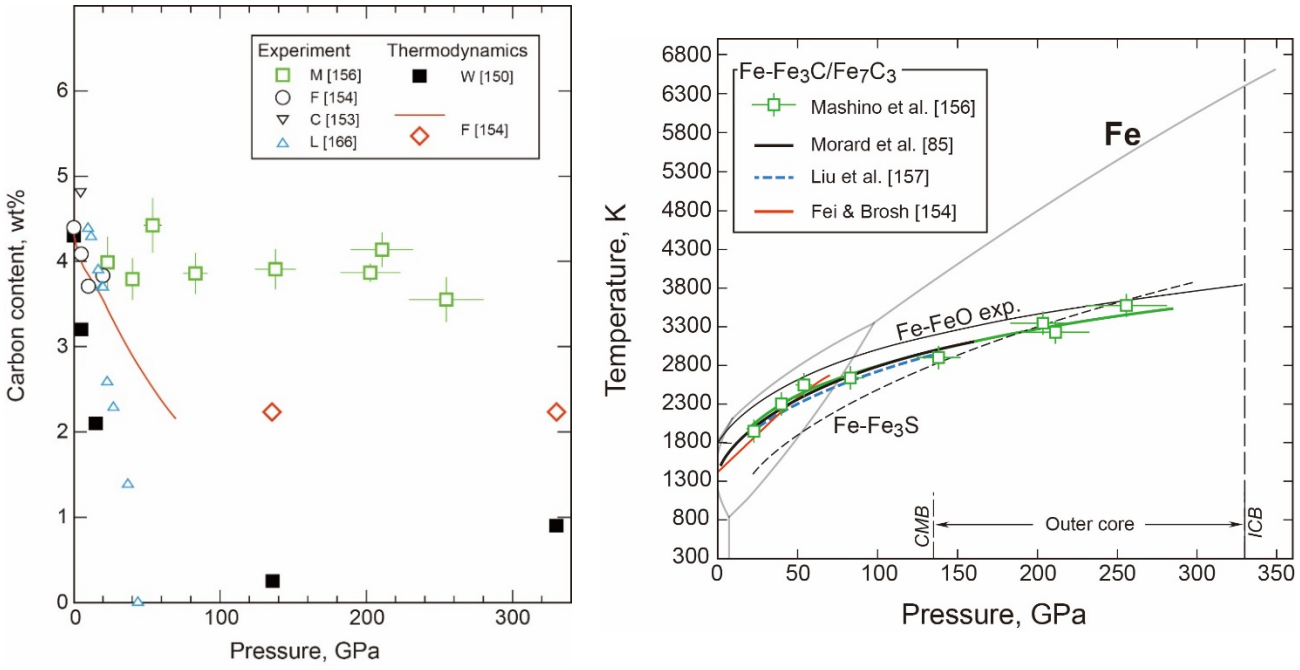


**Figure 27.** (**a**) Eutectic compositions in the Fe-$Fe_3C/Fe_7C_3$ system. Experimental data are plotted (Chabot et al. [153]; Lord et al. [166]; Fei and Brosh [154]; Mashino et al. [156]). Results of thermodynamic calculations by [150] and [154] are also shown. (**b**) Eutectic temperatures of the Fe-$Fe_3C/Fe_7C_3$ system (Mashino et al. [156]; Morard et al. [85]; Liu et al. [157]; Fei and Brosh [154]). Experimental data for the Fe-FeO system [86] and Fe-$Fe_3S$ [122] are also shown for comparison. The phase relations for pure Fe is from [9].

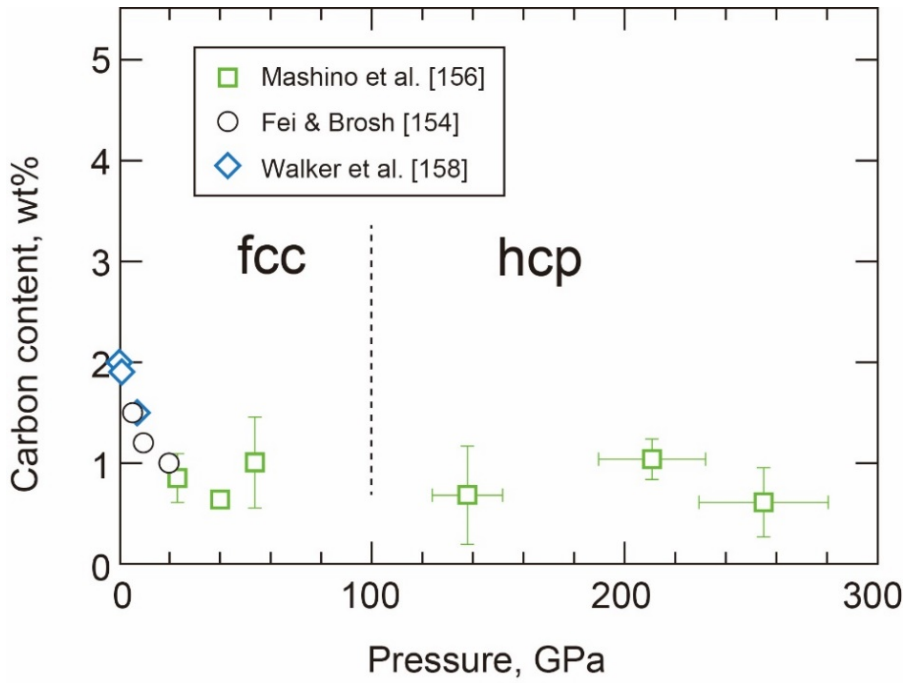


**Figure 28.** Carbon content in solid iron phases in the system Fe-C (Walker et al. [158]; Fei and Brosh [154]; Mashino et al. [156]). The figure is from [156].

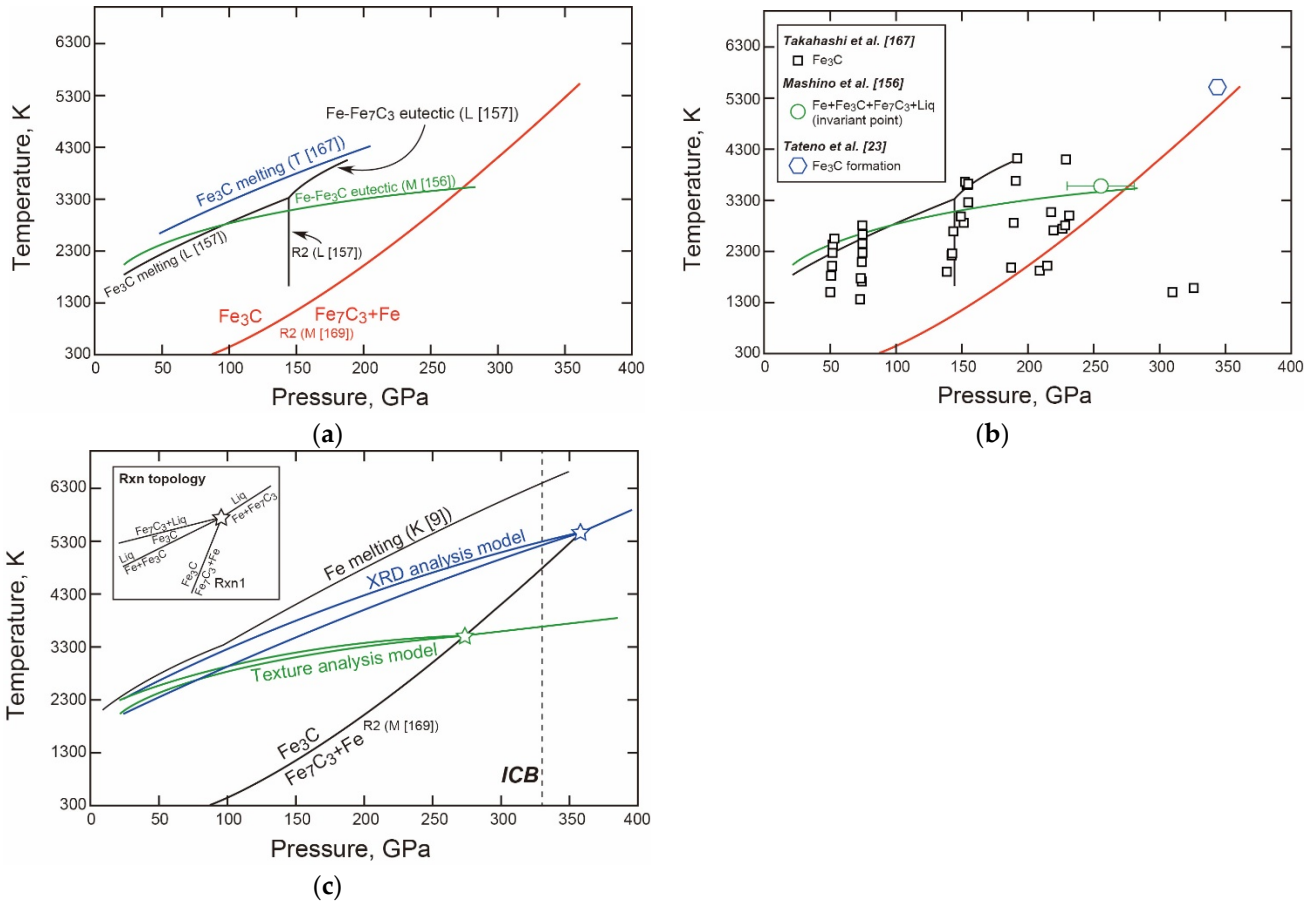


**Figure 29.** (**a**) Phase relations in the Fe-C system up to 400 GPa and 6000 K (Liu et al. [157]; Mashino et al. [156]; Takahashi et al. [167]; McGuire et al. [169]). The solid red line shows reaction $Fe_3C$ = $Fe_7C_3$ +Fe calculated in [169]. (**b**) Selected experimental data points from the literature. Mashino et al. [156] observed an invariant assemblage in their experimental run charge at the intersection of reaction $Fe_3C$ = $Fe_7C_3$ + Fe and the eutectic melting curve (green, [156]). The black lines are the observed phase boundaries by in situ XRD [157]. Experimental data of Takahashi et al. [167] are also plotted; their 300 K data are not shown. Tateno et al. [23] observed the formation of $Fe_3C$ in their Fe sample at 5520 K and 344 GPa. (**c**) Inferred phase diagram for the Fe-C system. The stars denote two possible cases of the invariant point where Fe, $Fe_3C$, $Fe_7C_3$, and liquid coexist. The in situ XRD analysis-based work [23,167] forms the invariant point at 360 GPa and 5500 K (blue star) whereas the texture analysis-based model [156] placed it at 275 GPa and 3500 K (green star). The melting curve for pure Fe is taken from Komabayashi [9]. Rxn, reaction. The figures were modified after McGuire et al. [169].

An invariant point occurs on the reaction boundary (R2) where Fe, $Fe_3C$, $Fe_7C_3$, and liquid are stable, which places constraints on the liquidus temperature of a C-rich outer core [166,169]. From the invariant point, melting reactions originate: $Fe_3C$ = $Fe_7C_3$ + liquid, Fe + $Fe_3C$ = liquid, and Fe + $Fe_7C_3$ = liquid (Figure 29c). Two possible *P*-*T* locations for the invariant point were predicted from existing experimental data combined with reaction (R2) determined in [169] (Figure 29c): 360 GPa and 5500 K based on XRD studies [23,167] and 275 GPa and 3500 K based on a texture analysis-based study [156]. If the XRD-based model is the case, $Fe_3C$ is stable over the outer core pressure conditions and the Fe-$Fe_3C$ subsystem may be relevant for an outer core composition near the eutectic point. In contrast, if the invariant point constrained by the textural analysis of DAC experiments [156] is the case, the subsolidus system would be Fe-$Fe_7C_3$.

- **Thermodynamic Model of the System**

Thermodynamic models of the system at 1 bar revealed that liquids show negative nonideal mixing [152,170,171]. Wood [150] and more recently Fei and Brosh [154] established high-pressure thermodynamic models for melting relations based on available experimental data. Both models predicted the eutectic points moving towards the Fe side with increasing pressure but became fairly constant above 136 GPa (Figure 27a).

At a core pressure of 136 GPa, the eutectic composition and temperature are not in agreement between the model by Fei and Brosh [154] and the experimental data by Mashino et al. [156] (Figure 26d). The disagreement could be reduced by refining the mixing model used in [154].

On the other hand, Fei and Brosh [154] and Mashino et al. [156] agreed on the stability of $Fe_3C$ which is decomposed between 136 and 330 GPa. As discussed above, $Fe_3C$ might be stable at the inner core conditions and its stability is related with the liquidus temperatures of the Fe-C system (Figure 29c). Constraining the liquid properties combined with the thermodynamics of the subsolidus reaction $3Fe_3C = Fe_7C_3 + 2Fe$ [169] will provide a holistic understanding of the system.

- **Density and Velocity of Fe-C Liquid and Solid in the** Core

Figure 30a shows the density of $Fe_3C$ and $Fe_7C_3$ solid phases calculated from the EoS [169,172]. The experimental *P-V-T* data were collected to 117 GP and 2100 K for $Fe_3C$ and 72 GPa and 1973 K for $Fe_7C_3$ and therefore Figure 30a is based on large extrapolations. Nevertheless, $Fe_3C$ is less dense at any temperature than the inner core while the density of $Fe_7C_3$ may match the inner core PREM when the temperature is as low as 3700 ± 500 K.

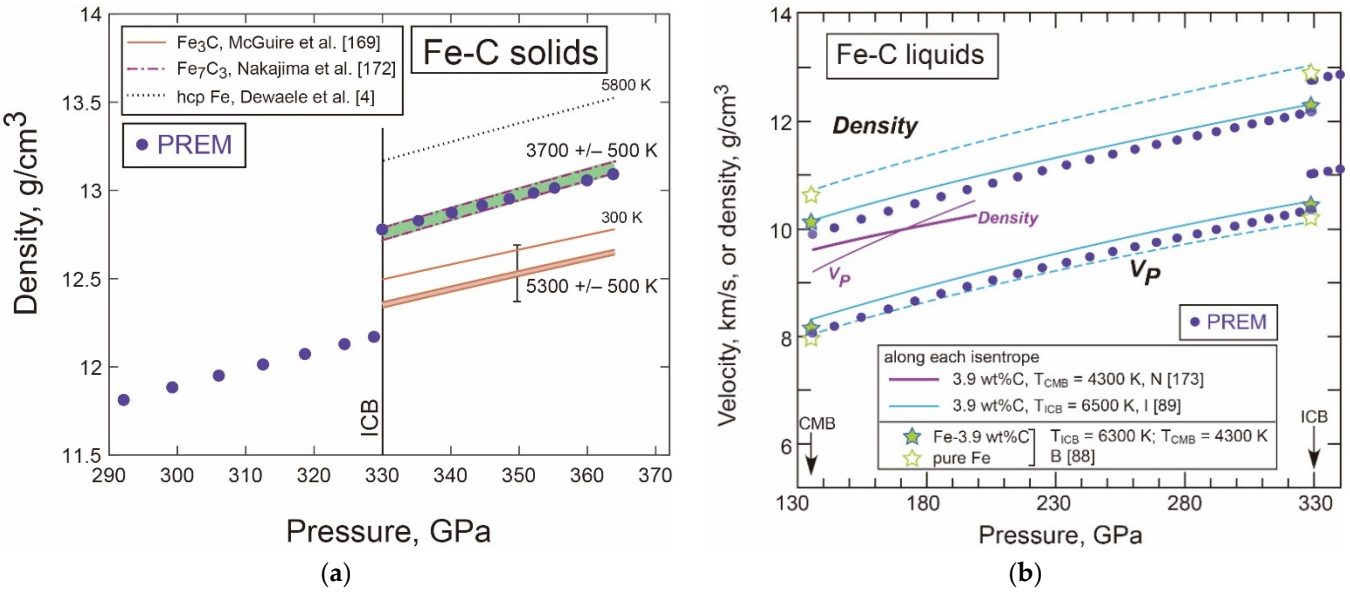


**Figure 30.** (**a**) Density versus pressure relation for the solid inner core with PREM and candidate iron carbides. The ICB pressure is indicated. Solid $Fe_3C$ is shown at 300 K and 5300 ± 500 K in the solid orange line [169]. Solid $Fe_7C_3$ at 3700 ± 500 K is shown in the dot-dash line [172]. Solid hcp iron at 5800 K [4] is shown in the short-dash line. The uncertainty bar attached to the density of $Fe_3C$ is propagated from the uncertainties in the EoS parameters. The figures are taken from [169]. (**b**) Density and *Vp* for Fe-C liquids over the outer core pressure range together with the PREM data. Results from the first-principles calculations are shown (Badro et al. [88]; Ichikawa and Tsuchiya [89]). Experimental measurements of Fe-3.9C using inelastic X-ray scattering are also plotted [173]. Isentropic profiles of liquid Fe are compared (dashed blue lines, Ichikawa et al. [50]) from Figure 3.

Comparison of the density and *Vp* of Fe-C liquids with the outer core profiles is made in Figure 30b. Results of first-principles calculations for Fe-3.9C show moderate reductions in density but great increases in *Vp* [88,89], which means there is no "best-representing" solution for the Fe-C system. The *Vp* of an Fe-C liquid with the same composition (Fe-3.9C) was examined in laser-heated DAC with synchrotron inelastic X-ray scattering to 70 GPa and 2800 K, followed by an evaluation of its thermal EoS from their *Vp* measurements [173]. Nakajima et al. [173] then calculated the *Vp* and density of liquid Fe-3.9C under core *P-T* conditions and compared them with the PREM (Figure 30b). Their plots are for a similar temperature to those of the first-principles calculations and therefore one can directly compare the data. The experimental determination [173] shows a greater reduction in density and increase in *Vp* than the theoretical results. This indicates that the properties of the Fe-C liquid are very sensitive to the carbon content. Nakajima et al. [173] estimated the carbon content required to account for the PREM values; 1.2–0.9 wt% C for velocity and 3.8–2.9 wt% for density, depending on the temperature and uncertainty of data extrapolation. They concluded that carbon cannot be a predominant light element in the outer core. However, a 1–2 wt% C in the outer core may crystallise a carbon-bearing hcp phase that could match the inner core PREM density as discussed above. As such, although the addition of carbon alone to iron cannot account for the properties of the outer core, the presence of carbon, particularly in the inner core, cannot be ruled out.

### 3.2.5. Fe-H

The Fe-H system is probably the most challenging system for an experimental study among the Fe-light element systems reviewed in this paper as the characterization of hydrogen dissolved in phases is very difficult. This is because Fe solid phases at 1 bar show little hydrogen solubility in the order of <0.05 at% (Figure 31a) and therefore the precise quantitative measurements of the amount of hydrogen in phases require in situ analysis [174] or very rapid (i.e., anvil breaking) decompression to turn dissolved hydrogen into bubbles which leave traces in the sample [175]. The hydrogen solubility in the Fe phases is conventionally expressed with a coefficient x, in iron hydride, FeHx. The x value drastically increases with increasing pressure (Figure 31b).

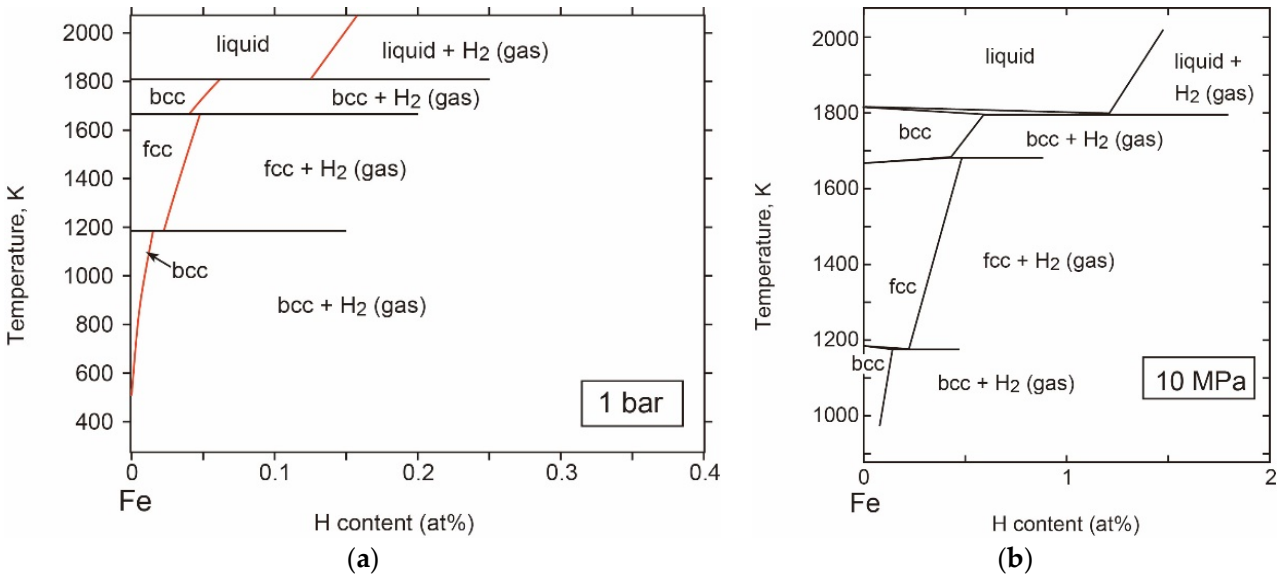


**Figure 31.** Phase relations for the Fe-H system at (**a**) 1 bar and (**b**) 10 MPa [176]. Note that the red lines in (**a**) show observed limit of H solubility and are not necessarily equilibrium phase boundaries. In (**b**) the H solubility in Fe phases is increased compared to at 1 bar.

- **The *T-X* Relations**

At 1 bar, the iron phases show negligible hydrogen solubility [176] and therefore, the phase assemblage in the Fe-H system is always FeHx + $H_2$ (gas) (Figure 31a). The hydrogen solubility, namely the x value, increases with increasing pressure (Figure 31b). Phase relations at 10 MPa shown in Figure 31b also show that the transitions between the bcc and fcc phases occur with loops [176]. The x value further increases with pressure and would reach 1, which means that stoichiometric FeH becomes stable at about 10 GPa [177] (Figure 32a). Fukai [178] suggested that the *T-X* relation at high pressures (e.g., 100 GPa) would be characterised by the presence of an extensive solid solution between Fe and FeH (x = 1) which covers a wide compositional range and the melting would occur over a loop (Figure 32b). This prediction was based on experimental observations that the x value became constant above 10 GPa [179,180]. However, Pepin et al. [181] reported new FeHx phases with x = 2 and 3 at 67 and 86 GPa, respectively, observed upon laser heating in DAC, which was later supported by Hirose et al. [182] to 127 GPa. As such, the compositional range of the solid-solution is expanding as the system is explored further.

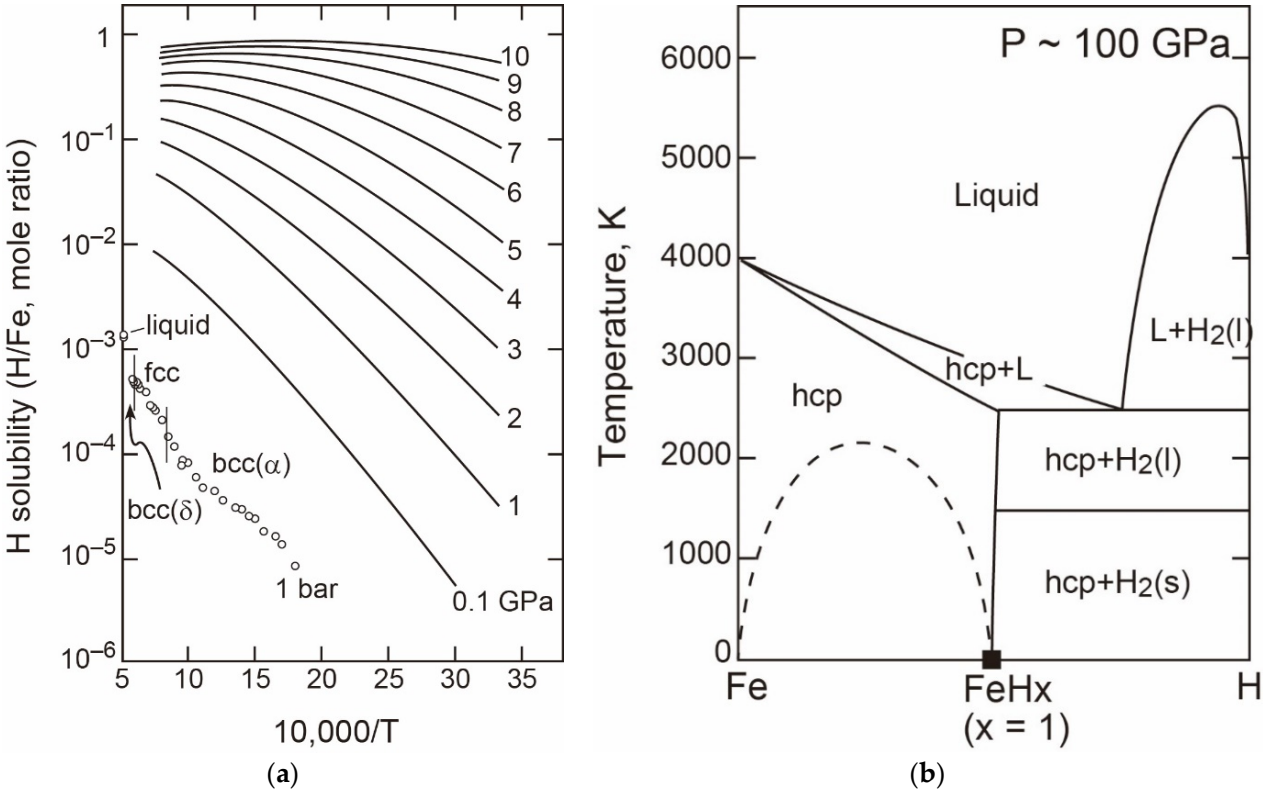


**Figure 32.** (**a**) Solubility of hydrogen in iron as a function of temperature and pressure. Experimental data for 1 bar are shown as open circles. The solid curves represent the results of thermodynamic calculations by Fukai and Suzuki [177]. The figure is taken from Fukai and Suzuki [177]. (**b**) A predicted phase diagram of the Fe-H system at ~100 GPa [178]. L, metallic liquid; $H_2$(s), solid hydrogen; $H_2$(l) liquid hydrogen. The figure was modified after Fukai [178].

As predicted by Fukai [178], the presence of solid FeHx solution under high pressure may result in a melting loop (Figure 32b). Sakamaki et al. [179], however, could not resolve the solidus and liquidus in their multi-anvil experiments to 21 GPa in which temperature precision was high, which suggests that the melting loop might be very narrow. A very narrow melting loop could partition hydrogen equally between solid and liquid and therefore could not account for the density contrast between the inner core and outer core.

- ***P-T* Relations**

The subsolidus phase relations of the Fe-H system can be compared with those of pure Fe. Notable differences include that a double hcp (dhcp) structure is stabilized instead of hcp under high pressure (Figure 33) and fcc FeH would be stable to high pressures. Previously dhcp, fcc, and liquid were expected to form a triple point (e.g., [179]), which is comparable to the invariant point in pure Fe where fcc, hcp, and liquid coexist. This was, however, recently challenged by observations of fcc FeH at higher pressures than previously expected [183–185]. Kato et al. [185] observed the formation of fcc FeH at 1000 K above 57 GPa, which implies that the fcc-dhcp boundary with a positive d$P$/d$T$ slope constrained at low pressures to 21 GPa would bend back towards low temperature with increasing pressure (Figure 33). As a consequence, this topology hinders the formation of the triple point and the phase diagram looks very different from that for pure Fe. The high-pressure dhcp-fcc transition with a negative d$P$/d$T$ slope can be tested by thermodynamic analysis. For example, the high-pressure phase, fcc must be denser than the dhcp phase upon transition.

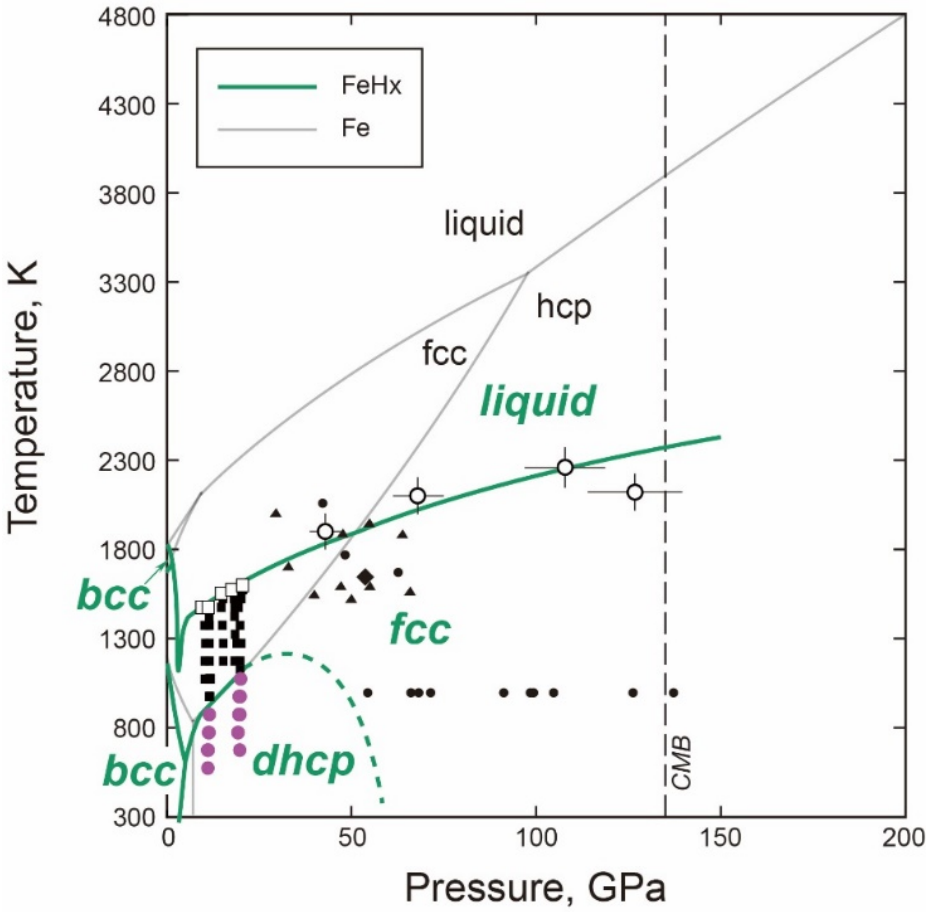


**Figure 33.** *P-T* phase relations for FeHx (x~1) in comparison with Fe [9]. The symbols are experimental observations: purple circles, dhcp; solid square, fcc; open square, liquid (Sakamaki et al. [179]); triangles, fcc (Thompson et al. [184]); diamond, fcc (Narygina et al. [183]); black solid circle, fcc (Kato et al. [185]); large open circle, liquid (Hirose et al. [182]).

The melting temperature of FeHx under hydrogen-saturated conditions is dramatically reduced with increasing pressure to 3 GPa [174,179] (Figure 33). This can be explained by the enhanced hydrogen incorporation into the phases; the x value in solid phases drastically increases with pressure, and iron liquid shows a greater concentration of hydrogen than the coexisting solid (Figure 31b). As a consequence, the melting temperature reduces by 500 K at 3 GPa [178,186]. The melting points above 5 GPa were reported by [179] in a multi-anvil

apparatus and more recently in DAC by [182]. Hirose et al. [182] conducted laser-heated DAC experiments on the Fe-C-H system and they selected recovered samples which did not show a significant amount of carbon (0.2–0.3 wt% C) in Fe-H liquids and discussed the melting of FeHx at high pressures (Figure 33).

- **Density and Velocity of Fe-H Liquid and Solid in the Core**

Figure 34a shows relationships between the *Vp* and density (Birch plot) of solid FeHx and hcp Fe determined by experiment at 300 K or high temperatures and by first-principles calculation at $T = 0$ [180,187–190]. Both experiment and theory show that the addition of hydrogen to solid Fe increases both the *Vp* and shear wave velocity (*Vs*). The experimental data suggest that the *Vp* and density of the inner core may be explained by the addition of 0.2–0.3 wt% hydrogen [180]. There seems to be no solution for the *Vs* as the *Vs* of iron needs to be slowed down by the addition of a light element to Fe to match the inner core profile (Figure 34a), although the possibility that anharmonic effects could reduce the *Vs* under the inner core conditions cannot be ruled out [180].

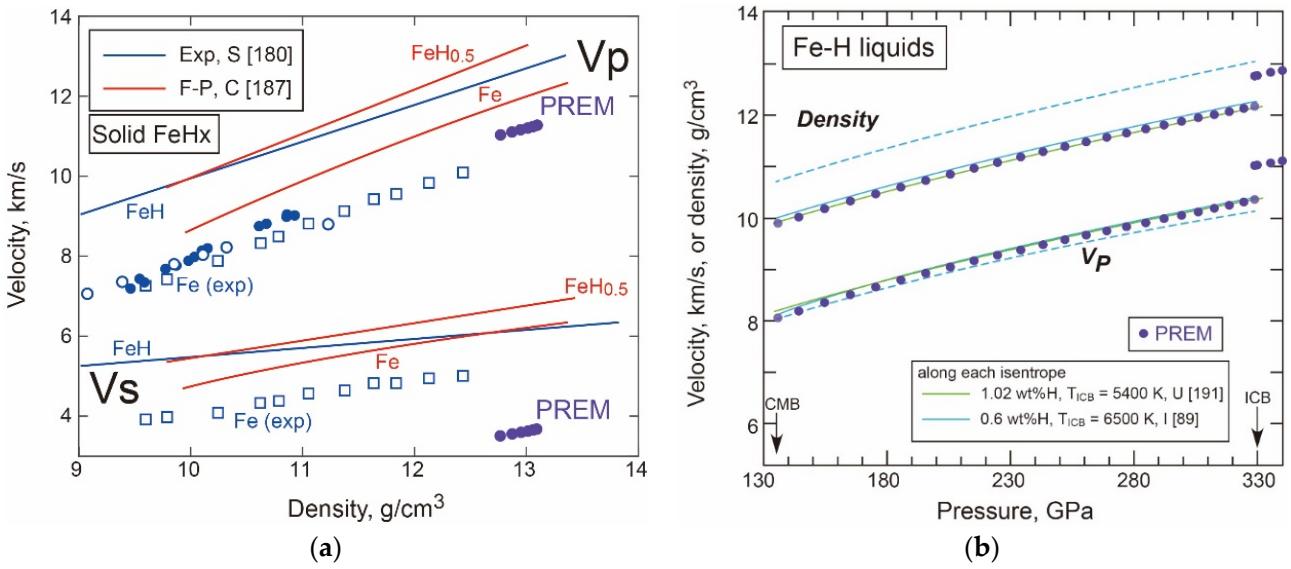


**Figure 34.** (**a**) *Vp*-density relations (Birch plot) for solid FeHx with the PREM data for the inner core. Experimentally constrained data using inelastic X-ray scattering are for FeH (x~1) by Shibazaki et al. [180] and results of first-principles calculations are for Fe and $FeH_{0.5}$ at $T = 0$ by Caracas [187]. The experimental data for pure hcp Fe are also shown for comparison [188–190]. (**b**) Density and *Vp* for Fe-H liquids over the outer core pressure range together with the PREM data. First-principles calculations were employed by Umemoto et al. [191] and Ichikawa and Tsuchiya [89]. Isentropic profiles of liquid Fe are compared (dashed blue lines, Ichikawa et al. [50]) from Figure 3.

Figure 34b compares the *Vp* and density of Fe-H liquids from first-principles calculations [89,191] with those of the outer core PREM. About 1 wt% hydrogen could match the calculated properties with the PREM profiles of the outer core.

### *3.3. Ternary Systems with Light Elements*

Below I will review two ternary systems and associated topics.

#### 3.3.1. Fe-Ni-Si

Phase relations in the Fe-Ni-Si system were experimentally investigated in DAC with in situ synchrotron XRD [58,110,192].

- **The fcc-hcp Transitions**

Komabayashi et al. [192] examined the *P*-*T* locations of the fcc-hcp transitions in Fe-5Ni-4Si in the internally resistive-heated DAC. Their results are compared with existing data for pure Fe [14] and the binary Fe-Ni [57] and Fe-Si [99] systems (Figure 35). Note that all the fcc–hcp transitions in those four different systems were examined in the internally heated DAC, which enables us to make a precise comparison. The addition of Ni reduces the transition temperature [55,57] whereas the Si incorporation has the opposite effect [97,99]. From these observations, one can expect that the simultaneous addition of Ni and Si will not greatly move the boundary from the case of pure Fe, as the effects of Ni and Si would cancel out.

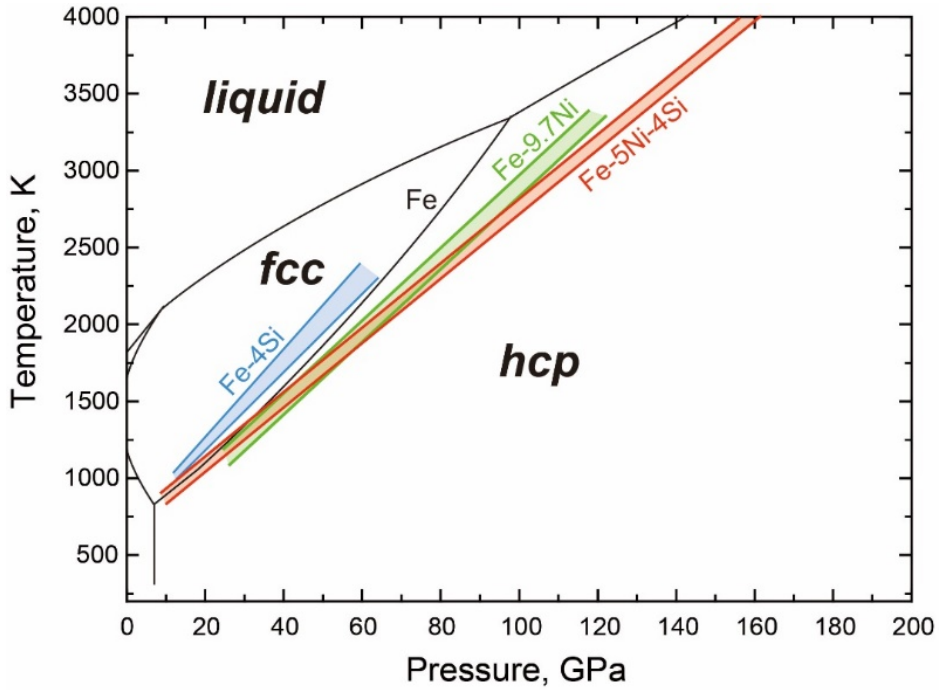


**Figure 35.** Comparison of the fcc-hcp transition boundaries in four different compositions: Fe [9,14], Fe-9.7Ni [57], Fe-4Si [99], and Fe-5Ni-4Si [192].

The transition in the Fe-Ni-Si system occurs at 15 GPa and 1000 K, similar to that for pure Fe. The Clausius–Clapeyron slope is however, 0.0480 GPa/K, which is larger than the reported slopes for Fe (0.0394 GPa/K, [14]), Fe-9.7Ni (0.0426 GPa/K, [57]), and Fe-4Si (0.0394 GPa/K, [99]), stabilising the fcc structure towards high pressure (Figure 35). Above 95 GPa, the boundary of the reaction hcp + fcc → fcc in Fe-5Ni-4Si is placed at a lower temperature than the hcp → hcp + fcc boundary in Fe-9.7Ni (Figure 35). This is even more important because Fe-5Ni-4Si contains less Ni than Fe-9.7Ni. As such, the simultaneous addition of Ni and Si has an anomalous effect on the transition pressure and temperature, which is greatly stabilising the fcc structure under high pressure.

The d$P$/d$T$ slopes of the fcc-hcp transition boundaries in different systems and related properties, which include the volume change ($\Delta V$) and entropy change ($\Delta S$) upon transition, were summarized in [192]. The d$P$/d$T$ slopes and $\Delta V$ were directly obtained from the experiments while $\Delta S$ were calculated through the Clausius–Clapeyron equation, $\Delta P/\Delta T = \Delta S/\Delta V$. Komabayashi et al. [192] showed that the increased slope in Fe-5Ni-4Si relative to pure Fe is because of a significantly small $\Delta V$. The addition of Ni to Fe-Si changes $\Delta S$ little, but reduces $\Delta V$, which leads to the increased d$P$/d$T$ slope in Fe-5Ni-4Si. As such, the thermodynamic properties of the fcc-hcp transition in Fe-5Ni-4Si cannot readily be explained by a combination of the Fe-Ni and Fe-Si systems. The origin of the enlarged fcc

stability may lie in the mixing properties of the phases. The triple point, where the fcc, hcp, and liquid phases coexist in Fe-5Ni-4Si is placed at 145 GPa and 3750 K (Figure 36).

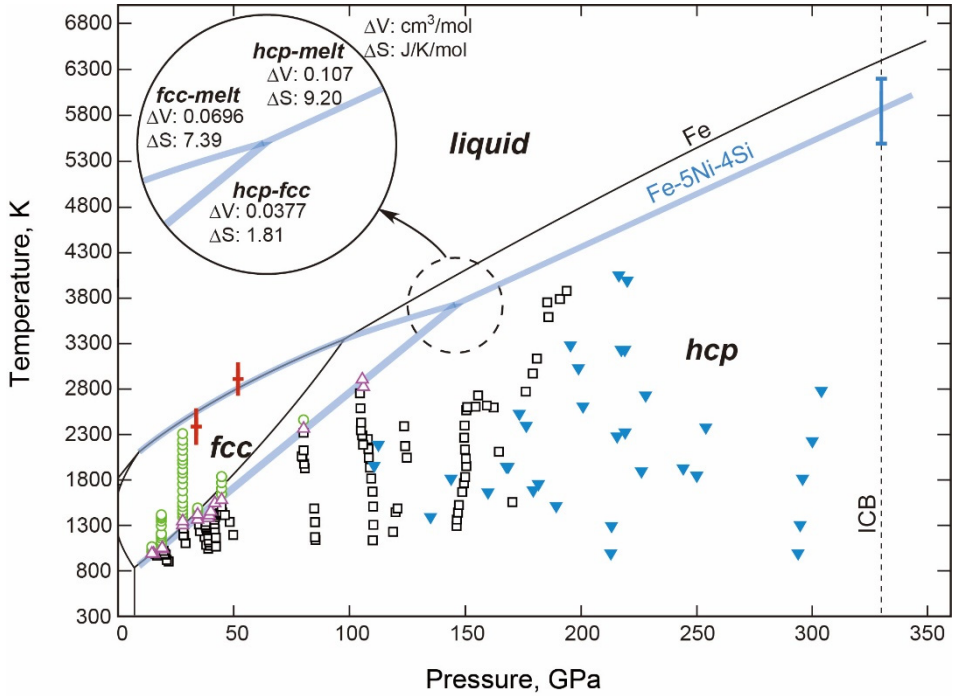


**Figure 36.** A phase diagram for Fe-5Ni-4Si (blue thick line). Experimental data plotted are: hcp in Fe-5Ni-4Si (open black square, Komabayashi et al. [192]) and Fe-4.8Ni-4Si (inverted blue triangle, Sakai et al. [58]), hcp+fcc in Fe-5Ni-4Si (purple triangle, [192]), fcc in Fe-5Ni-4Si (green circle, [192]), and melting of Fe-5Ni-10Si (red cross, Morard et al. [110]). Komabayashi et al.'s [192] data were based on internally resistive-heated DAC and laser-heated DAC. Inset: the thermodynamics of the triple point where the hcp, fcc, and liquid phases coexist.

- **The Melting Temperatures**

Figure 36 shows a phase diagram of Fe–5Ni–4Si reporting the fcc–hcp boundaries together with phase relations in pure Fe [9]. Experimental constraints on melting in Fe-5Ni-10Si under high pressure were also shown as the crosses in Figure 36 [110]. Since the melting temperature in Fe–Ni–Si is not greatly different from that in Fe up to 50 GPa, Komabayashi et al. [192] assumed the same fcc melting curve for Fe-5Ni-4Si. As the melting loop was not resolved in the previous works, they assumed a narrow melting interval, namely, between solidus and liquidus, and expressed it as a single thick line (Figure 36).

The triple point where the fcc, hcp, and liquid phases coexist is located at 100 GPa and 3400 K for pure Fe [9]. Assuming the same fcc melting curve as for pure Fe, the triple point for Fe-5Ni-4Si is located at 145 GPa and 3750 K. The melting curve of the hcp phase was obtained from the Clausius-Clapeyron relation at the triple point (inset of Figure 36) with the thermodynamics of fcc melting [9]. The phase diagram obtained is consistent with earlier laser-heated DAC experiments in Fe-4.8Ni-4Si to 304 GPa and 2780 K [58].

The melting temperature of the Fe-5Ni-4Si hcp phase at the ICB pressure is estimated to be 5850 $\pm$ 350 K, which is 550 K lower than the pure Fe melting temperature. This is consistent with shock wave measurements in Fe-8Ni-10Si [193] although their measurements did not address the structure of the phases. As mentioned above, the melting temperature of Fe-Ni-Si alloy is not very different from that of pure Fe when the alloy structure is fcc [110]. Due to the shift of the triple point towards the high pressure, the melting temperature of the hcp alloy should be largely reduced. As such, the phase relations in the Fe-Ni-Si system cannot readily be inferred from those in the binary Fe-Ni and Fe-Si

systems, and therefore the melting temperature as well as the melting relations at 330 GPa needs to be directly constrained.

3.3.2. Fe-Si-O

The phase relations of the Fe-Si-O system at 1 bar are characterized by the presence of two-liquid immiscibility in the Fe-O-rich portion. The two-liquid field occurs due to the immiscibility between the metallic Fe-rich liquid and ionic FeO-rich liquid as was seen in Section 3.2.1.

- **Phase Relations and Mixing Properties for Liquids**

Phase relations of the Fe-rich portion under high pressure were constrained by laser-heated DAC experiments [194,195]. Hirose et al. [194] showed that the liquidus phases were $SiO_2$ for their experimental samples with compositions from Fe-12.1Si-8.3O to Fe-3.8Si-4.4O and the coexisting liquids were depleted in silicon or oxygen on the basis of chemical analysis of recovered samples. This implies that the eutectic point(s) should be placed near the Fe-Si or Fe-O axes (Figure 37). Arveson et al. [195] also conducted laser-heated DAC experiments on Fe-9Si-3O. They however reported a texture which they took as evidence for the presence of liquid immiscibility just above the solidus over a pressure range from 13 to 78 GPa. The temperature interval for immiscibility was rather constant over their experimental pressure range (Figure 38), which would be aligned with that in the Fe-FeO system over the 15 to 21 GPa pressure range explored by Tsuno et al. [77].

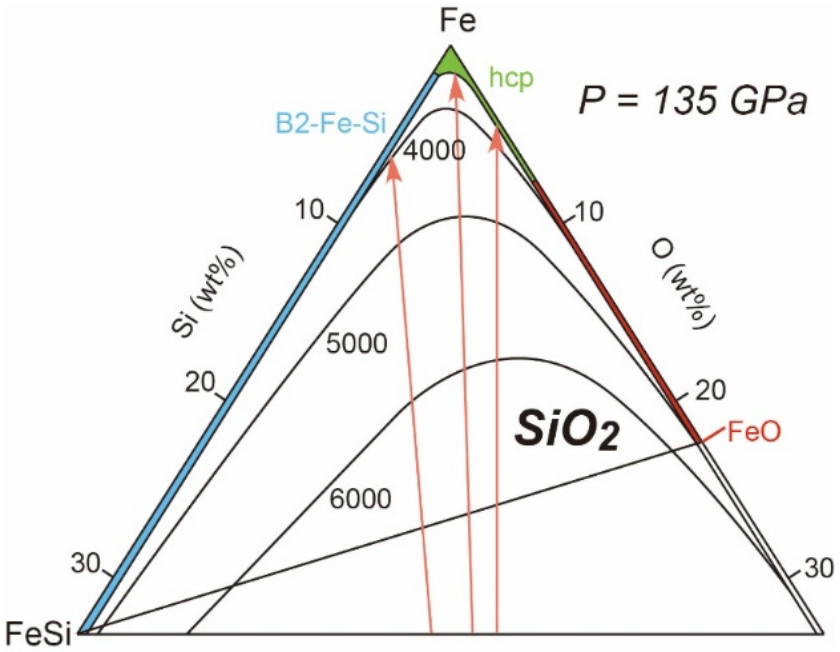


**Figure 37.** Liquidus phase relations in Fe-FeSi-FeO at about 135 GPa (Hirose et al. [194]) which are characterized by the presence of a large liquidus field with $SiO_2$. The arrows show the directions of liquid compositions moving away from $SiO_2$ upon crystallization, found in their experiments. Green, blue, and red areas are the liquidus fields with hcp Fe, CsCl type (B2) Fe-Si phase, and FeO, respectively. The figure is from [194].

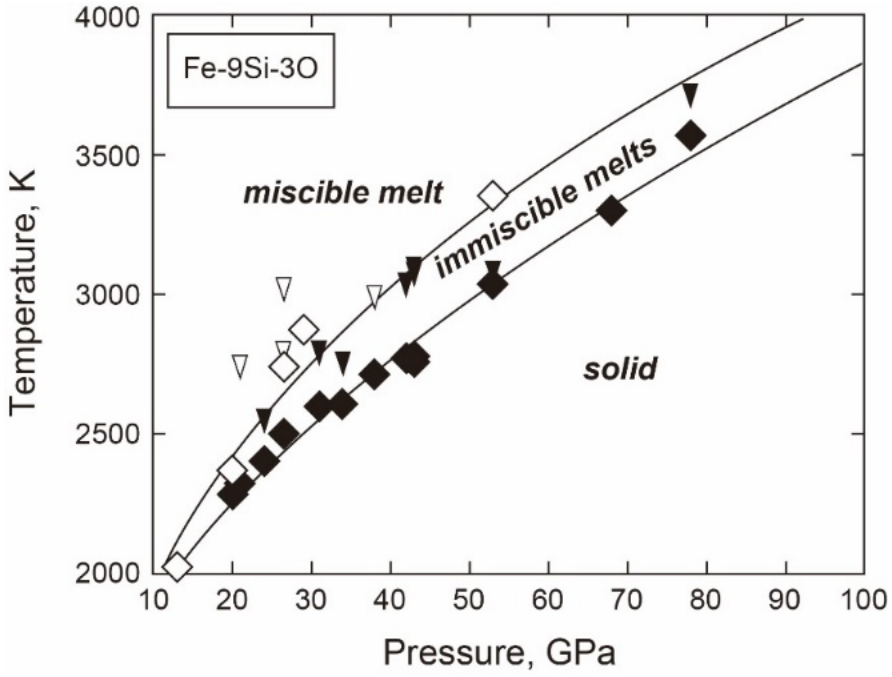


**Figure 38.** A proposed *P-T* diagram for Fe-9Si-3O showing a miscibility region based on textural observation of laser-heated DAC samples (Arveson et al. [195]). The open and solid diamonds are temperatures for closure of immiscibility and for solidus, respectively. The open and solid inverted triangles denote the maximum experimental temperatures for miscible and immiscible regions, respectively.

Arveson et al. [195] also employed first-principles molecular dynamics simulations. They used three indirect criteria for phase separation as there is no direct measure for it with these types of simulations: atom trajectories, oxygen clustering, and evolution of atom-atom coordination numbers. One of the key results was that most oxygens were clustered with each other via O-Fe/Si bonding under *P-T* conditions where their experiments observed immiscibility, supporting their interpretation of the texture showing immiscibility. However, this was challenged by Huang et al. [108] who also employed first-principles calculations, but with longer simulation durations for 10, 20, and 29 ps in contrast to 6.6–14.8 ps in Arveson et al. [195]. Huang et al. [108] observed full mixing in the longest simulation runs. They also concluded that the atoms of Fe, Si, and O mix ideally under the core conditions.

Huang et al. [108] also challenged the scenario proposed by Hirose et al. [194] that $SiO_2$ is being crystallised from the outer core at the CMB. Huang et al. [108] reversed the experiment by investigating a two-phase simulation containing solid $SiO_2$ in contact with liquid Fe and observed that $SiO_2$ and Fe phases mixed in a short time scale (less than 10 ps) above 4100 K at the CMB pressure, which is a relevant temperature for the outer core.

In summary, the discussion points here are whether the mixing property of Fe-Si-O liquids is ideal or nonideal, and whether the outer core is at its liquidus temperature for $SiO_2$ crystallisation or at a greater temperature at the CMB. Meanwhile, the enlarged $SiO_2$ liquidus field proposed by [194] has not been tested by first-principles calculation.

## 4. Conclusions

As reviewed above, the phase relations of every binary system have not fully been understood under high *P-T* conditions. The maximum *P-T* conditions achieved by experiment for some systems are still away from those corresponding to the centre of the Earth. Nevertheless, we can draw a significant conclusion that any of the binary systems reviewed here by itself cannot account for all the properties of Earth's core. While future research

needs to resolve the existing discrepancies raised for each binary system, we should start rigorous and meticulous study on the ternary systems.

**Funding:** This research was funded by the European Research Council (ERC) Consolidator Grant, grant number #647723.

**Acknowledgments:** The author thanks Simone Anzellini and Daniel Errandonea for the invitation to this special volume. Chris McGuire and Sam Thompson are thanked for their discussions. The anonymous reviewers are acknowledged for their thorough reading and comments on the manuscript which improved the quality of the paper.

**Conflicts of Interest:** The author declares no conflict of interest. The funders had no role in the design of the study; in the collection, analyses, or interpretation of data; in the writing of the manuscript, or in the decision to publish the results.

## References

1. Bancroft, D.; Peterson, E.L.; Minshall, S. Polymorphism of iron at high pressure. *J. Appl. Phys.* **1956**, *27*, 291–298. [CrossRef]
2. Anderson, O.L. *Equations of State of Solids for Geophysics and Ceramic Science*; Oxford University Press: New York, NY, USA, 1995; p. 405.
3. Jackson, I.; Rigden, S.M. Analysis of *P-V-T* data: Constraints on the thermoelastic properties of high-pressure minerals. *Phys. Earth Planet. Inter.* **1996**, *96*, 85–112. [CrossRef]
4. Dewaele, A.; Loubeyre, P.; Occelli, F.; Mezouar, M.; Dorogokupets, P.I.; Torrent, M. Quasihydrostatic equation of state of iron above 2 Mbar. *Phys. Rev. Lett.* **2006**, *97*, 215504. [CrossRef] [PubMed]
5. Alfè, D.; Price, G.D.; Gillan, M.J. Thermodynamics of hexagonal-close-packed iron under Earth's core conditions. *Phys. Rev. B* **2001**, *64*, 045123. [CrossRef]
6. Anderson, O.L.; Oda, H.; Isaak, D.G. A model for the computation of thermal expansivity at high compression and high temperatures: MgO as an example. *Geophys. Res. Lett.* **1992**, *19*, 1987–1990. [CrossRef]
7. Callen, H.B. *Thermodynamics*; John Wiley & Sons Inc.: Hoboken, NJ, USA, 1960; p. 376.
8. Dinsdale, A.T. SGTE data for pure elements. *Calphad* **1991**, *15*, 317–425. [CrossRef]
9. Komabayashi, T. Thermodynamics of melting relations in the system Fe-FeO at high pressure: Implications for oxygen in the Earth's core. *J. Geophys. Res.* **2014**, *119*. [CrossRef]
10. Komabayashi, T. Thermodynamics of the system Fe-Si-O under high pressure and temperature and its implications for Earth's core. *Phys. Chem. Miner.* **2020**, *47*. [CrossRef]
11. Uchida, T.; Wang, Y.; Rivers, M.L.; Sutton, S.R. Stability field and thermal equation of state of e-iron determined by synchrotron X-ray diffraction in a multianvil apparatus. *J. Geophys. Res.* **2001**, *106*, 21709–21810. [CrossRef]
12. Shen, G.; Mao, H.-K.; Hemley, R.J.; Duffy, T.S.; Rivers, M.L. Melting and crystal structure of iron at high pressures and temperatures. *Geophys. Res. Lett.* **1998**, *25*, 373–376. [CrossRef]
13. Boehler, R. Temperatures in the Earth's core from melting-point measurements of iron at high static pressures. *Nature* **1993**, *363*, 534–536. [CrossRef]
14. Komabayashi, T.; Fei, Y.; Meng, Y.; Prakapenka, V. In-situ X-ray diffraction measurements of the γ-ε transition boundary of iron in an internally-heated diamond anvil cell. *Earth Planet. Sci. Lett.* **2009**, *282*, 252–257. [CrossRef]
15. Anzellini, S.; Dewaele, A.; Mezouar, M.; Loubeyre, P.; Morard, G. Melting of iron at Earth's inner core boundary based on fast X-ray diffraction. *Science* **2013**, *340*, 464–466. [CrossRef] [PubMed]
16. Mao, H.K.; Bell, P.M.; Hadidiacos, C. Experimental phase relations of iron to 360 kbar, 1400 °C, determined in an internally heated diamond-anvil apparatus. In *High-Pressure Research in Mineral Physics*; Manghnani, M.H., Syono, Y., Eds.; American Geophysical Union: Washington, DC, USA, 1987; pp. 135–138.
17. Funamori, N.; Yagi, T.; Uchida, T. High-pressure and high-temperature in situ x-ray diffraction study of iron to above 30 GPa using MA8-type apparatus. *Geophys. Res. Lett.* **1996**, *23*, 953–956. [CrossRef]
18. Kubo, A.; Ito, E.; Katsura, T.; Shinmei, T.; Yamada, H.; Nishikawa, O.; Song, M.; Funakoshi, K. In situ X-ray observation of iron using Kawai-type apparatus equipped with sintered diamond: Absence of β phase up to 44 GPa and 2100 K. *Geophys. Res. Lett.* **2003**, *30*. [CrossRef]
19. Morelli, A.; Dziewonski, A.M.; Woodhouse, J.H. Anisotropy of the inner core inferred from PKIKP travel times. *Geophys. Res. Lett.* **1986**, *13*, 1545–1548. [CrossRef]
20. Woodhouse, J.H.; Giardini, D.; Li, X.-D. Evidence for inner core anisotropy from free oscillations. *Geophys. Res. Lett.* **1986**, *13*, 1549–1552. [CrossRef]
21. Creager, K.C. Anisotropy of the inner core from differential travel times of the phases PKP and PKIKP. *Nat. Cell Biol.* **1992**, *356*, 309–314. [CrossRef]
22. Song, X.; Helmberger, D.V. Anisotropy of Earth's inner core. *Geophys. Res. Lett.* **1993**, *20*, 2591–2594. [CrossRef]
23. Tateno, S.; Hirose, K.; Ohishi, Y.; Tatsumi, Y. The structure of iron in Earth's inner core. *Science* **2010**, *330*, 359–361. [CrossRef]
24. Stixrude, L. Structure of Iron to 1 Gbar and 40 000 K. *Phys. Rev. Lett.* **2012**, *108*, 055505. [CrossRef]

25. Sinmyo, R.; Hirose, K.; Ohishi, Y. Melting curve of iron to 290 GPa determined in a resistance-heated diamond-anvil cell. *Earth Planet. Sci. Lett.* **2019**, *510*, 45–52. [CrossRef]
26. Kuwayama, Y.; Hirose, K.; Sata, N.; Ohishi, Y. Phase relations of iron and iron-nickel alloys up to 300 GPa: Implications for composition and structure of the Earth's inner core. *Earth Planet. Sci. Lett.* **2008**, *273*, 379–385. [CrossRef]
27. Brown, M.J.; McQueen, R.G. Phase transitions, Grueneisen parameter, and elasticity for shocked iron between 77 GPa and 400 GPa. *J. Geophys. Res.* **1986**, *91*, 7485–7494. [CrossRef]
28. Boehler, R. The phase diagram of iron to 430 kbar. *Geophys. Res. Lett.* **1986**, *13*, 1153–1156. [CrossRef]
29. Belonoshko, A.B.; Ahuja, R.; Johansson, B. Stability of the body-centred-cubic phase of iron in the Earth's inner core. *Nature* **2003**, *424*, 1032–1034. [CrossRef] [PubMed]
30. Mikhaylushkin, A.S.; Simak, S.I.; Dubrovinsky, L.; Dubrovinskaia, N.; Johansson, B.; Abrikosov, I.A. Pure Iron Compressed and Heated to Extreme Conditions. *Phys. Rev. Lett.* **2007**, *99*, 165505. [CrossRef] [PubMed]
31. Luo, W.; Johansson, B.; Eriksson, O.; Arapan, S.; Souvatzis, P.; Katsnelson, M.I.; Ahuja, R. Dynamical stability of body center cubic iron at the Earth's core conditions. *Proc. Natl. Acad. Sci. USA* **2010**, *107*, 9962–9964. [CrossRef] [PubMed]
32. Belonoshko, A.B.; Lukinov, T.; Fu, J.; Zhao, J.; Davis, S.; Simak, S.I. Stabilization of body-centred cubic iron under inner-core conditions. *Nat. Geosci.* **2017**, *10*, 312–316. [CrossRef]
33. Nguyen, J.H.; Holmes, N.C. Melting of iron at the physical conditions of the Earth's core. *Nature* **2004**, *427*, 339–342. [CrossRef]
34. Yoo, C.S.; Holmes, N.C.; Ross, M.; Webb, D.J.; Pike, C. Shock temperatures and melting of iron at Earth core conditions. *Phys. Rev. Lett.* **1993**, *70*, 3931–3934. [CrossRef] [PubMed]
35. Turneaure, S.J.; Sharma, S.M.; Gupta, Y.M. Crystal Structure and Melting of Fe Shock Compressed to 273 GPa: In Situ X-ray Diffraction. *Phys. Rev. Lett.* **2020**, *125*, 215702. [CrossRef] [PubMed]
36. Alfè, D.; Gillan, M.J.; Price, G.D. The melting curve of iron at the pressures of the Earth's core from ab initio calculations. *Nature* **1999**, *401*, 462–464. [CrossRef]
37. Belonoshko, A.B.; Ahuja, R.; Johansson, B. Quasi–Ab InitioMolecular Dynamic Study of Fe Melting. *Phys. Rev. Lett.* **2000**, *84*, 3638–3641. [CrossRef] [PubMed]
38. Alfè, D. Temperature of the inner-core boundary of the Earth: Melting of iron at high pressure from first-principles coexistence simulations. *Phys. Rev. B* **2009**, *79*, 060101. [CrossRef]
39. Laio, A.; Bernard, S.; Chiarotti, G.L.; Scandolo, S.; Tosatti, E. Physics of iron at Earth's core conditions. *Science* **2000**, *287*, 1027–1030. [CrossRef]
40. Jackson, J.M.; Sturhahn, W.; Lerche, M.; Zhao, J.Y.; Toellner, T.S.; Alp, E.E.; Sinogeikin, S.V.; Bass, J.D.; Murphy, C.A.; Wicks, J.K. Melting of compressed iron by monitoring atomic dynamics. *Earth Planet. Sci. Lett.* **2013**, *362*, 143–150. [CrossRef]
41. Morard, G.; Boccato, S.; Rosa, A.D.; Anzellini, S.; Miozzi, F.; Henry, L.; Garbarino, G.; Mezouar, M.; Harmand, M.; Guyot, F.; et al. Solving Controversies on the Iron Phase Diagram Under High Pressure. *Geophys. Res. Lett.* **2018**, *45*, 11074–11082. [CrossRef]
42. Guillermet, A.F.; Gustafson, P. An assessment of the thermodynamic properties and the (p, T) phase diagram of iron. *High Temp. High Press.* **1985**, *16*, 591–610.
43. Saxena, S.K.; Dubrovinsky, L.S. Thermodynamics of iron phases at high pressures and temperatures. In *Properties of Earth and Planetary Materials*; Manghnani, M.H., Yagi, T., Eds.; American Geophysical Union: Washington, DC, USA, 1998; pp. 271–279.
44. Tsujino, N.; Nishihara, Y.; Nakajima, Y.; Takahashi, E.; Funakoshi, K.; Higo, Y. Equation of state of gamma-Fe: Reference density for planetary cores. *Earth Planet. Sci. Lett.* **2013**, *375*, 244–253. [CrossRef]
45. Alfè, D.; Price, G.D.; Gillan, M.J. Iron under Earth's core conditions: Liquid-state thermodynamics and high-pressure melting curve from ab initio calculations. *Phys. Rev. B* **2002**, *65*, 165118. [CrossRef]
46. Tiwari, G.P. Modification of Richard's rule and correlation between entropy of fusion and allotropic behaviour. *Met. Sci.* **1978**, *12*, 317–320. [CrossRef]
47. Anderson, W.W.; Ahrens, T.J. An equation of state for liquid iron and implications for the Earth's core. *J. Geophys. Res.* **1994**, *99*, 4273–4284. [CrossRef]
48. Kuwayama, Y.; Morard, G.; Nakajima, Y.; Hirose, K.; Baron, A.Q.R.; Kawaguchi, S.I.; Tsuchiya, T.; Ishikawa, D.; Hirao, N.; Ohishi, Y. Equation of state of liquid iron under extreme conditions. *Phys. Rev. Lett.* **2020**, *124*, 165701. [CrossRef] [PubMed]
49. Wagle, F.; Steinle-Neumann, G. Liquid iron equation of state to the terapascal regime from ab initio simulations. *J. Geophys. Res. Solid Earth* **2019**, *124*, 3350–3364. [CrossRef]
50. Ichikawa, H.; Tsuchiya, T.; Tange, Y. The *P-V-T* equation of state and thermodynamic properties of liquid iron. *J. Geophys. Res. Solid Earth* **2014**, *119*, 240–252. [CrossRef]
51. Dziewonski, A.M.; Anderson, D.L. Preliminary reference Earth model. *Phys. Earth Planet. Inter.* **1981**, *25*, 297–356. [CrossRef]
52. Fei, Y.W.; Murphy, C.; Shibazaki, Y.; Shahar, A.; Huang, H.J. Thermal equation of state of hcp-iron: Constraint on the density deficit of Earth's solid inner core. *Geophys. Res. Lett.* **2016**, *43*, 6837–6843. [CrossRef]
53. Li, J.; Fei, Y. Experimental constraints on core composition. In *Treatise on Geochemistry Update*; Holland, H.D., Turekian, K.K., Eds.; Elsevier Ltd.: Amsterdam, The Netherlands, 2007; pp. 1–31.
54. Lin, J.-F.; Heinz, D.L.; Campbell, A.J.; Devine, J.M.; Mao, W.L.; Shen, G. Iron-Nickel alloy in the Earth's core. *Geophys. Res. Lett.* **2002**, *29*. [CrossRef]
55. Mao, W.L.; Campbell, A.J.; Heinz, D.L.; Shen, G. Phase relations of Fe–Ni alloys at high pressure and temperature. *Phys. Earth Planet. Inter.* **2006**, *155*, 146–151. [CrossRef]

56. Dubrovinsky, L.; Dubrovinskaia, N.; Narygina, O.; Kantor, I.; Kuznetzov, A.; Prakapenka, V.B.; Vitos, L.; Johansson, B.; Mikhaylushkin, A.S.; Simak, S.I.; et al. Body-centered cubic iron-nickel alloy in Earth's core. *Science* **2007**, *316*, 1880–1883. [CrossRef] [PubMed]
57. Komabayashi, T.; Hirose, K.; Ohishi, Y. In situ X-ray diffraction measurements of the fcc–hcp phase transition boundary of an Fe–Ni alloy in an internally heated diamond anvil cell. *Phys. Chem. Miner.* **2012**, *39*, 329–338. [CrossRef]
58. Sakai, T.; Ohtani, E.; Hirao, N.; Ohishi, Y. Stability field of the hcp-structure for Fe, Fe-Ni, and Fe-Ni-Si alloys up to 3 Mbar. *Geophys. Res. Lett.* **2011**, *38*, 09302. [CrossRef]
59. Tateno, S.; Hirose, K.; Komabayashi, T.; Ozawa, H.; Ohishi, Y. The structure of Fe-Ni alloy in Earth's inner core. *Geophys. Res. Lett.* **2012**, *39*. [CrossRef]
60. Zhang, D.Z.; Jackson, J.M.; Zhao, J.Y.; Sturhahn, W.; Alp, E.E.; Hu, M.Y.; Toellner, T.S.; Murphy, C.A.; Prakapenka, V.B. Temperature of Earth's core constrained from melting of Fe and $Fe_{0.9}Ni_{0.1}$ at high pressures. *Earth Planet. Sci. Lett.* **2016**, *447*, 72–83. [CrossRef]
61. Torchio, R.; Boccato, S.; Miozzi, F.; Rosa, A.D.; Ishimatsu, N.; Kantor, I.; Sevelin-Radiguet, N.; Briggs, R.; Meneghini, C.; Irifune, T.; et al. Melting Curve and Phase Relations of Fe-Ni Alloys: Implications for the Earth's Core Composition. *Geophys. Res. Lett.* **2020**, *47*. [CrossRef]
62. Zou, G.; Mao, H.K.; Bell, P.M.; Virgo, D. High pressure experiments on the iron oxide wüstite ($Fe_{1-x}O$). *Carnegie Inst. Wash. Yearb.* **1980**, *79*, 374–376.
63. Jeanloz, R.; Ahrens, T.J. Equations of state of FeO and CaO. *Geophys. J. R. Astron. Soc.* **1980**, *62*, 505–528. [CrossRef]
64. Knittle, E.; Jeanloz, R. High-Pressure metallization of FeO and implications for the Earth core. *Geophys. Res. Lett.* **1986**, *13*, 1541–1544. [CrossRef]
65. Knittle, E.; Jeanloz, R.; Mitchell, A.C.; Nellis, W.J. Metallization of $Fe_{0.94}O$ at elevated pressures and temperatures observed by shock-wave electrical resistivity measurements. *Solid State Commun.* **1986**, *59*, 513–515. [CrossRef]
66. Fei, Y.W.; Mao, H.K. In-situ determination of the NiAs phase of FeO at high-pressure and Temperature. *Science* **1994**, *266*, 1678–1680. [CrossRef] [PubMed]
67. Kondo, T.; Ohtani, E.; Hirao, N.; Yagi, T.; Kikegawa, T. Phase transitions of (Mg,Fe)O at megabar pressures. *Phys. Earth Planet. Inter.* **2004**, *143*, 201–213. [CrossRef]
68. Ozawa, H.; Hirose, K.; Tateno, S.; Sata, N.; Ohishi, Y. Phase transition boundary between B1 and B8 structures of FeO up to 210 GPa. *Phys. Earth Planet. Inter.* **2010**, *179*, 157–163. [CrossRef]
69. Ozawa, H.; Takahashi, F.; Hirose, K.; Ohishi, Y.; Hirao, N. Phase transition of FeO and stratification in Earth's outer core. *Science* **2011**, *334*, 792–794. [CrossRef] [PubMed]
70. Ohta, K.; Cohen, R.E.; Hirose, K.; Haule, K.; Shimizu, K.; Ohishi, Y. Experimental and theoretical evidence for pressure-induced metallization in FeO with rocksalt-type structure. *Phys. Rev. Lett.* **2012**, *108*, 026403. [CrossRef] [PubMed]
71. Ohta, K.; Hirose, K.; Shimizu, K.; Ohishi, Y. High-pressure experimental evidence for metal FeO with normal NiAs-type structure. *Phys. Rev. B* **2010**, *82*, 174120. [CrossRef]
72. Fischer, R.A.; Campbell, A.J.; Lord, O.T.; Shofner, G.A.; Dera, P.; Prakapenka, V.B. Phase transition and metallization of FeO at high pressures and temperatures. *Geophys. Res. Lett.* **2011**, *38*, L24301. [CrossRef]
73. Fischer, R.A.; Campbell, A.J.; Shofner, G.A.; Lord, O.T.; Dera, P.; Prakapenka, V.B. Equation of state and phase diagram of FeO. *Earth Planet. Sci. Lett.* **2011**, *304*, 496–502. [CrossRef]
74. Fischer, R.A.; Campbell, A.J. High-pressure melting of wüstite. *Am. Mineral.* **2010**, *95*, 1473–1477. [CrossRef]
75. Seagle, C.T.; Heinz, D.L.; Campbell, A.J.; Prakapenka, V.B.; Wanless, S.T. Melting and thermal expansion in the Fe-FeO system at high pressure. *Earth Planet. Sci. Lett.* **2008**, *265*, 655–665. [CrossRef]
76. Lindsley, D.H. Pressure-temperature relations in the system FeO-$SiO_2$. *Year Book Carnegie Inst. Wash.* **1966**, *65*, 226–230.
77. Tsuno, K.; Ohtani, E.; Terasaki, H. Immiscible two-liquid regions in the Fe–O–S system at high pressure: Implications for planetary cores. *Phys. Earth Planet. Inter.* **2007**, *160*, 75–85. [CrossRef]
78. Ohtani, E.; Ringwood, A.; Hibberson, W. Composition of the core, II. Effect of high pressure on solubility of FeO in molten iron. *Earth Planet. Sci. Lett.* **1984**, *71*, 94–103. [CrossRef]
79. Wriedt, H. The Fe-O (iron-oxygen) system. *J. Phase Equilibria Diffus.* **1991**, *12*, 170–200. [CrossRef]
80. Sundman, B. An assessment of the Fe-O system. *J. Phase Equilibria Diffus.* **1991**, *12*, 127–140. [CrossRef]
81. Kowalski, M.; Spencer, P.J. Thermodynamic reevaluation of the Cr-O, Fe-O and Ni-O systems-remodeling of the liquid, bcc and fcc phases. *Calphad* **1995**, *19*, 229–243. [CrossRef]
82. Frost, D.J.; Asahara, Y.; Rubie, D.C.; Miyajima, N.; Dubrovinsky, L.S.; Holzapfel, C.; Ohtani, E.; Miyahara, M.; Sakai, T. Partitioning of oxygen between the Earth's mantle and core. *J. Geophys. Res. Space Phys.* **2010**, *115*. [CrossRef]
83. Darken, L.S.; Gurry, R.W. The system iron-oxygen. II. Equilibrium and thermodynamics of liquid oxide and other phases. *J. Am. Chem. Soc.* **1946**, *68*, 798–816. [CrossRef]
84. Ringwood, A.E.; Hibberson, W. The system Fe-FeO revisited. *Phys. Chem. Miner.* **1990**, *17*, 313–319. [CrossRef]
85. Morard, G.; Andrault, D.; Antonangeli, D.; Nakajima, Y.; Auzende, A.L.; Boulard, E.; Cervera, S.; Clark, A.; Lord, O.T.; Siebert, J.; et al. Fe-FeO and Fe-$Fe_3C$ melting relations at Earth's core-mantle boundary conditions: Implications for a volatile-rich or oxygen-rich core. *Earth Planet. Sci. Lett.* **2017**, *473*, 94–103. [CrossRef]
86. Oka, K.; Hirose, K.; Tagawa, S.; Kidokoro, Y.; Nakajima, Y.; Kuwayama, Y.; Morard, G.; Coudurier, N.; Fiquet, G. Melting in the Fe-FeO system to 204 GPa: Implications for oxygen in Earth's core. *Am. Mineral.* **2019**, *104*, 1603–1607. [CrossRef]

87. Hattori, T.; Kinoshita, T.; Narushima, T.; Tsuji, K.; Katayama, Y. Pressure-induced structural change of liquid CdTe up to 23.5 GPa. *Phys. Rev. B* **2006**, *73*, 054203. [CrossRef]
88. Badro, J.; Cote, A.S.; Brodholt, J.P. A seismologically consistent compositional model of Earth's core. *Proc. Natl. Acad. Sci. USA* **2014**, *111*, 7542–7545. [CrossRef] [PubMed]
89. Ichikawa, H.; Tsuchiya, T. Ab Initio Thermoelasticity of Liquid Iron-Nickel-Light Element Alloys. *Minerals* **2020**, *10*, 59. [CrossRef]
90. Alfè, D.; Gillan, M.; Price, G. Composition and temperature of the Earth's core constrained by combining ab initio calculations and seismic data. *Earth Planet. Sci. Lett.* **2002**, *195*, 91–98. [CrossRef]
91. Dobson, D.P.; Crichton, W.A.; Bouvier, P.; Vočadlo, L.; Wood, I.G. The equation of state of CsCl-structured FeSi to 40 GPa: Implications for silicon in the Earth's core. *Geophys. Res. Lett.* **2003**, *30*. [CrossRef]
92. Lin, J.F.; Heinz, D.L.; Campbell, A.J.; Devine, J.M.; Shen, G.Y. Iron-silicon alloy in Earth's core? *Science* **2002**, *295*, 313–315. [CrossRef] [PubMed]
93. Lin, J.F.; Scott, H.P.; Fischer, R.A.; Chang, Y.Y.; Kantor, I.; Prakapenka, V.B. Phase relations of Fe-Si alloy in Earth's core. *Geophys. Res. Lett.* **2009**, *36*. [CrossRef]
94. Kuwayama, Y.; Hirose, K. Phase relations in the system Fe-FeSi at 21 GPa. *Am. Mineral.* **2004**, *89*, 273–276. [CrossRef]
95. Fischer, R.A.; Campbell, A.J.; Reaman, D.M.; Miller, N.A.; Heinz, D.L.; Dera, P.; Prakapenka, V.B. Phase relations in the Fe-FeSi system at high pressures and temperatures. *Earth Planet. Sci. Lett.* **2013**, *373*, 54–64. [CrossRef]
96. Fischer, R.A.; Campbell, A.J.; Caracas, R.; Reaman, D.M.; Heinz, D.L.; Dera, P.; Prakapenka, V.B. Equations of state in the Fe-FeSi system at high pressures and temperatures. *J. Geophys. Res. Solid Earth* **2014**, *119*, 2810–2827. [CrossRef]
97. Tateno, S.; Kuwayama, Y.; Hirose, K.; Ohishi, Y. The structure of Fe-Si alloy in Earth's inner core. *Earth Planet. Sci. Lett.* **2015**, *418*, 11–19. [CrossRef]
98. Ozawa, H.; Hirose, K.; Yonemitsu, K.; Ohishi, Y. High-pressure melting experiments on Fe–Si alloys and implications for silicon as a light element in the core. *Earth Planet. Sci. Lett.* **2016**, *456*, 47–54. [CrossRef]
99. Komabayashi, T.; Pesce, G.; Morard, G.; Antonangeli, D.; Sinmyo, R.; Mezouar, M. Phase transition boundary between fcc and hcp structures in Fe-Si alloy and its implications for terrestrial planetary cores. *Am. Mineral.* **2019**, *104*, 94–99. [CrossRef]
100. Fischer, R.A.; Campbell, A.J.; Caracas, R.; Reaman, D.M.; Dera, P.; Prakapenka, V.B. Equation of state and phase diagram of Fe-16Si alloy as a candidate component of Earth's core. *Earth Planet. Sci. Lett.* **2012**, *357*, 268–276. [CrossRef]
101. Asanuma, H.; Ohtani, E.; Sakai, T.; Terasaki, H.; Kamada, S.; Hirao, N.; Sata, N.; Ohishi, Y. Phase relations of Fe-Si alloy up to core conditions: Implications for the Earth inner core. *Geophys. Res. Lett.* **2008**, *35*. [CrossRef]
102. Kuwayama, Y.; Sawai, T.; Hirose, K.; Sata, N.; Ohishi, Y. Phase relations of iron–silicon alloys at high pressure and high temperature. *Phys. Chem. Miner.* **2009**, *36*, 511–518. [CrossRef]
103. Vočadlo, L.; Alfè, D.; Gillan, M.J.; Wood, I.G.; Brodholt, J.P.; Price, G.D. Possible thermal and chemical stabilization of body-centred-cubic iron in the Earth's core. *Nature* **2003**, *424*, 536–539. [CrossRef]
104. Belonoshko, A.B.; Rosengren, A.; Burakovsky, L.; Preston, D.L.; Johansson, B. Melting of Fe and $Fe_{0.9375}Si_{0.0625}$ at Earth's core pressures studied using ab initio molecular dynamics. *Phys. Rev. B* **2009**, *79*, 220102. [CrossRef]
105. Andrault, D.; Bolfan-Casanova, N.; Ohtaka, O.; Fukui, H.; Arima, H.; Fialin, M.; Funakoshi, K. Melting diagrams of Fe-rich alloys determined from synchrotron in situ measurements in the 15–23 GPa pressure range. *Phys. Earth Planet. Inter.* **2009**, *174*, 181–191. [CrossRef]
106. Morard, G.; Siebert, J.; Andrault, D.; Guignot, N.; Garbarino, G.; Guyot, F.; Antonangeli, D. The Earth's core composition from high pressure density measurements of liquid iron alloys. *Earth Planet. Sci. Lett.* **2013**, *373*, 169–178. [CrossRef]
107. Ohnuma, I.; Abe, S.; Shimenouchi, S.; Omori, T.; Kainuma, R.; Ishida, K. Experimental and thermodynamic studies of the Fe–Si binary system. *ISIJ Int.* **2012**, *52*, 540–548. [CrossRef]
108. Huang, D.Y.; Badro, J.; Brodholt, J.; Li, Y.G. Ab Initio molecular dynamics investigation of molten Fe-Si-O in Earth's core. *Geophys. Res. Lett.* **2019**, *46*, 6397–6405. [CrossRef]
109. Asanuma, H.; Ohtani, E.; Sakai, T.; Terasaki, H.; Kamada, S.; Kondo, T.; Kikegawa, T. Melting of iron–silicon alloy up to the core–mantle boundary pressure: Implications to the thermal structure of the Earth's core. *Phys. Chem. Miner.* **2009**, *37*, 353–359. [CrossRef]
110. Morard, G.; Andrault, D.; Guignot, N.; Siebert, J.; Garbarino, G.; Antonangeli, D. Melting of Fe-Ni-Si and Fe-Ni-S alloys at megabar pressures: Implications for the core-mantle boundary temperature. *Phys. Chem. Miner.* **2011**, *38*, 767–776. [CrossRef]
111. Lord, O.T.; Wann, E.T.H.; Hunt, S.A.; Walker, A.M.; Santangeli, J.; Walter, M.J.; Dobson, D.P.; Wood, I.G.; Vočadlo, L.; Morard, G.; et al. The NiSi melting curve to 70 GPa. *Phys. Earth Planet. Inter.* **2014**, *233*, 13–23. [CrossRef]
112. Yamasaki, M.; Banno, S. Zoning pattern of extremely fractionated plagioclase crystallized from simple system. *Bull. Volcanol. Soc. Jpn.* **1972**, *2*, 18–25. (In Japanese with English abstract)
113. Wade, J.; Wood, B.J. Core formation and the oxidation state of the Earth. *Earth Planet. Sci. Lett.* **2005**, *236*, 78–95. [CrossRef]
114. Antonangeli, D.; Siebert, J.; Badro, J.; Farber, D.L.; Fiquet, G.; Morard, G.; Ryerson, F.J. Composition of the Earth's inner core from high-pressure sound velocity measurements in Fe-Ni-Si alloys. *Earth Planet. Sci. Lett.* **2010**, *295*, 292–296. [CrossRef]
115. Rubie, D.C.; Frost, D.J.; Mann, U.; Asahara, Y.; Nimmo, F.; Tsuno, K.; Kegler, P.; Holzheid, A.; Palme, H. Heterogeneous accretion, composition and core-mantle differentiation of the Earth. *Earth Planet. Sci. Lett.* **2011**, *301*, 31–42. [CrossRef]
116. Badro, J.; Brodholt, J.P.; Piet, H.; Siebert, J.; Ryerson, F.J. Core formation and core composition from coupled geochemical and geophysical constraints. *Proc. Natl. Acad. Sci. USA* **2015**, *112*, 12310–12314. [CrossRef] [PubMed]

117. Antonangeli, D.; Morard, G.; Paolasini, L.; Garbarino, G.; Murphy, C.A.; Edmund, E.; Decremps, F.; Fiquet, G.; Bosak, A.; Mezouar, M.; et al. Sound velocities and density measurements of solid hcp-Fe and hcp-Fe-Si (9 wt%) alloy at high pressure: Constraints on the Si abundance in the Earth's inner core. *Earth Planet. Sci. Lett.* **2018**, *482*, 446–453. [CrossRef]
118. Nakajima, Y.; Kawaguchi, S.I.; Hirose, K.; Tateno, S.; Kuwayama, Y.; Sinmyo, R.; Ozawa, H.; Tsutsui, S.; Uchiyama, H.; Baron, A.Q.R. Silicon-depleted present-day Earth's outer core revealed by sound velocity measurements of liquid fe-si alloy. *J. Geophys. Res. Solid Earth* **2020**, *125*, e2020JB019399. [CrossRef]
119. Hirose, K.; Labrosse, S.; Hernlund, J. Composition and state of the core. *Annu. Rev. Earth Planet. Sci.* **2013**, *41*, 657–691. [CrossRef]
120. Campbell, A.J.; Seagle, C.T.; Heinz, D.L.; Shen, G.Y.; Prakapenka, V.B. Partial melting in the iron–sulfur system at high pressure: A synchrotron X-ray diffraction study. *Phys. Earth Planet. Inter.* **2007**, *162*, 119–128. [CrossRef]
121. Ozawa, H.; Hirose, K.; Suzuki, T.; Ohishi, Y.; Hirao, N. Decomposition of $Fe_3S$ above 250 GPa. *Geophys. Res. Lett.* **2013**, *40*, 4845–4849. [CrossRef]
122. Mori, Y.; Ozawa, H.; Hirose, K.; Sinmyo, R.; Tateno, S.; Morard, G.; Ohishi, Y. Melting experiments on Fe–$Fe_3S$ system to 254 GPa. *Earth Planet. Sci. Lett.* **2017**, *464*, 135–141. [CrossRef]
123. Tateno, S.; Ozawa, H.; Hirose, K.; Suzuki, T.; I-Kawaguchi, S.; Hirao, N. $Fe_2S$: The most Fe-rich iron sulfide at the Earth's inner core pressures. *Geophys. Res. Lett.* **2019**, *46*, 11944–11949. [CrossRef]
124. Kamada, S.; Ohtani, E.; Terasaki, H.; Sakai, T.; Miyahara, M.; Ohishi, Y.; Hirao, N. Melting relationships in the Fe–$Fe_3S$ system up to the outer core conditions. *Earth Planet. Sci. Lett.* **2012**, *359–360*, 26–33. [CrossRef]
125. Pommier, A.; Laurenz, V.; Davies, C.J.; Frost, D.J. Melting phase relations in the Fe-S and Fe-S-O systems at core conditions in small terrestrial bodies. *ICARUS* **2018**, *306*, 150–162. [CrossRef]
126. Waldner, P.; Pelton, A.D. Thermodynamic modeling of the Fe-S system. *J. Phase Equilibria Diffus.* **2005**, *26*, 23–38. [CrossRef]
127. Chen, B.; Li, J.; Hauck, S.A. Non-ideal liquidus curve in the Fe-S system and Mercury's snowing core. *Geophys. Res. Lett.* **2008**, *35*. [CrossRef]
128. Fei, Y.W.; Li, J.; Bertka, C.M.; Prewitt, C.T. Structure type and bulk modulus of $Fe_3S$, a new iron-sulfur compound. *Am. Mineral.* **2000**, *85*, 1830–1833. [CrossRef]
129. Kamada, S.; Terasaki, H.; Ohtani, E.; Sakai, T.; Kikegawa, T.; Ohishi, Y.; Hirao, N.; Sata, N.; Kondo, T. Phase relationships of the Fe-FeS system in conditions up to the Earth's outer core. *Earth Planet. Sci. Lett.* **2010**, *294*, 94–100. [CrossRef]
130. Stewart, A.J.; Schmidt, M.W.; van Westrenen, W.; Liebske, C. Mars: A new core-crystallization regime. *Science* **2007**, *316*, 1323–1325. [CrossRef]
131. Chudinovskikh, L.; Boehler, R. Eutectic melting in the system Fe-S to 44 GPa. *Earth Planet. Sci. Lett.* **2007**, *257*, 97–103. [CrossRef]
132. Morard, G.; Andrault, D.; Guignot, N.; Sanloup, C.; Mezouar, M.; Petitgirard, S.; Fiquet, G. In situ determination of Fe–$Fe_3S$ phase diagram and liquid structural properties up to 65 GPa. *Earth Planet. Sci. Lett.* **2008**, *272*, 620–626. [CrossRef]
133. Morard, G.; Andrault, D.; Antonangeli, D.; Bouchet, J. Properties of iron alloys under the Earth's core conditions. *Comptes Rendus Geosci.* **2014**, *346*, 130–139. [CrossRef]
134. Li, J.; Fei, Y.; Mao, H.K.; Hirose, K.; Shieh, S.R. Sulfur in the Earth's inner core. *Earth Planet. Sci. Lett.* **2001**, *193*, 509–514. [CrossRef]
135. Seagle, C.T.; Campbell, A.J.; Heinz, D.L.; Shen, G.; Prakapenka, V.B. Thermal equation of state of $Fe_3S$ and implications for sulfur in Earth's core. *J. Geophys. Res. Space Phys.* **2006**, *111*. [CrossRef]
136. Kamada, S.; Ohtani, E.; Terasaki, H.; Sakai, T.; Takahashi, S.; Hirao, N.; Ohishi, Y. Equation of state of $Fe_3S$ at room temperature up to 2-megabars. *Phys. Earth Planet. Inter.* **2014**, *228*, 106–113. [CrossRef]
137. Chen, B.; Gao, L.L.; Funakoshi, K.; Li, J. Thermal expansion of iron-rich alloys and implications for the Earth's core. *Proc. Natl. Acad. Sci. USA* **2007**, *104*, 9162–9167. [CrossRef] [PubMed]
138. Thompson, S.; Komabayashi, T.; Breton, H.; Suehiro, S.; Glazyrin, K.; Pakhomova, A.; Ohishi, Y. Compression experiments to 126 GPa and 2500 K and thermal equation of state of $Fe_3S$: Implications for sulphur in the Earth's core. *Earth Planet. Sci. Lett.* **2020**, *534*, 116080. [CrossRef]
139. Hillert, M.; Staffansson, L.I. An analysis of the phase equilibria in the Fe-FeS system. *Metall. Mater. Trans. B* **1975**, *6*, 37–41. [CrossRef]
140. Sharma, R.C.; Chang, Y.A. Thermodynamics and phase relationships of transition metal-sulfur systems: Part III. Thermodynamic properties of the Fe-S liquid-phase and the calculation of the Fe-S phase diagram. *Metall. Trans. B* **1979**, *10*, 103–108. [CrossRef]
141. Guillermet, A.F.; Hillert, M.; Jansson, B.; Sundman, B. An assessment of the Fe-S system using a 2-sublattice model for the liquid-phase. *Metall. Trans. B* **1981**, *12*, 745–754. [CrossRef]
142. Chuang, Y.Y.; Hsieh, K.C.; Chang, Y.A. Thermodynamics and phase relationships of transition metal-sulfur systems: Part V. A reevaluation of the Fe-S System using an associated solution model for the liquid-phase. *Metall. Trans. B* **1985**, *16*, 277–285. [CrossRef]
143. Saxena, S.; Eriksson, G. Thermodynamics of Fe-S at ultra-high pressure. *Calphad* **2015**, *51*, 202–205. [CrossRef]
144. Umemoto, K.; Hirose, K.; Imada, S.; Nakajima, Y.; Komabayashi, T.; Tsutsui, S.; Baron, A.Q.R. Liquid iron-sulfur alloys at outer core conditions by first-principles calculations. *Geophys. Res. Lett.* **2014**, *41*, 6712–6717. [CrossRef]
145. Fu, J.; Cao, L.Z.; Duan, X.M.; Belonoshko, A.B. Density and sound velocity of liquid Fe-S alloys at Earth's outer core P-T conditions. *Am. Mineral.* **2020**, *105*, 1349–1354. [CrossRef]
146. Huang, H.J.; Wu, S.J.; Hu, X.J.; Wang, Q.S.; Wang, X.; Fei, Y.W. Shock compression of Fe-FeS mixture up to 204 GPa. *Geophys. Res. Lett.* **2013**, *40*, 687–691. [CrossRef]

147. Vočadlo, L.; Alfè, D.; Gillan, M.J.; Price, G.D. The properties of iron under core conditions from first principles calculations. *Phys. Earth Planet. Inter.* **2003**, *140*, 101–125. [CrossRef]
148. Grigorovich, V.K. The polymorphism of iron and the electron structure of iron alloys. *Izvt. Akad. Nauk. SSSR Met. JAN-FEB* **1969**, *1*, 53–68. (In Russian)
149. Shterenberg, L.E.; Slesarev, V.N.; Korsunskaya, I.A.; Kamenetskaya, D.S. The experimental study of the interaction between the melt, carbides and diamond in the iron-carbon system at high pressures. *High Temp. High Press.* **1975**, *7*, 517–522.
150. Wood, B.J. Carbon in the core. *Earth Planet. Sci. Lett.* **1993**, *117*, 593–607. [CrossRef]
151. Nakajima, Y.; Takahashi, E.; Suzuki, T.; Funakoshi, K. "Carbon in the core" revisited. *Phys. Earth Planet. Inter.* **2009**, *174*, 202–211. [CrossRef]
152. Gustafson, P. A Thermodynamic Evaluation of the Fe-C System. *Scand. J. Metall.* **1985**, *14*, 259–267. [CrossRef]
153. Chabot, N.L.; Campbell, A.J.; McDonough, W.F.; Draper, D.S.; Agee, C.B.; Humayun, M.; Watson, H.C.; Cottrell, E.; Saslow, S.A. The Fe-C system at 5 GPa and implications for Earth's core. *Geochim. Cosmochim. Acta* **2008**, *72*, 4146–4158. [CrossRef]
154. Fei, Y.W.; Brosh, E. Experimental study and thermodynamic calculations of phase relations in the Fe-C system at high pressure. *Earth Planet. Sci. Lett.* **2014**, *408*, 155–162. [CrossRef]
155. Benz, M.G.; Elliott, J.F. The austenite solidus and revised iron-carbon diagram. *Trans. Metall. Soc. AIME* **1961**, *221*, 323–331.
156. Mashino, I.; Miozzi, F.; Hirose, K.; Morard, G.; Sinmyo, R. Melting experiments on the Fe-C binary system up to 255 GPa: Constraints on the carbon content in the Earth's core. *Earth Planet. Sci. Lett.* **2019**, *515*, 135–144. [CrossRef]
157. Liu, J.; Lin, J.F.; Prakapenka, V.B.; Prescher, C.; Yoshino, T. Phase relations of $Fe_3C$ and $Fe_7C_3$ up to 185 GPa and 5200 K: Implication for the stability of iron carbide in the Earth's core. *Geophys. Res. Lett.* **2016**, *43*, 12415–12422.
158. Walker, D.; Dasgupta, R.; Li, J.; Buono, A. Nonstoichiometry and growth of some Fe carbides. *Contrib. Mineral. Petrol.* **2013**, *166*, 935–957. [CrossRef]
159. Caracas, R. The influence of carbon on the seismic properties of solid iron. *Geophys. Res. Lett.* **2017**, *44*, 128–134. [CrossRef]
160. Yang, J.; Fei, Y.W.; Hu, X.J.; Greenberg, E.; Prakapenka, V.B. Effect of carbon on the volume of solid iron at high pressure: Implications for carbon substitution in iron structures and carbon content in the Earth's inner core. *Minerals* **2019**, *9*, 720. [CrossRef]
161. Gao, L.L.; Chen, B.; Wang, J.Y.; Alp, E.E.; Zhao, J.Y.; Lerche, M.; Sturhahn, W.; Scott, H.P.; Huang, F.; Ding, Y.; et al. Pressure-induced magnetic transition and sound velocities of $Fe_3C$: Implications for carbon in the Earth's inner core. *Geophys. Res. Lett.* **2008**, *35*. [CrossRef]
162. Gao, L.L.; Chen, B.; Zhao, J.Y.; Alp, E.E.; Sturhahn, W.; Li, J. Effect of temperature on sound velocities of compressed $Fe_3C$, a candidate component of the Earth's inner core. *Earth Planet. Sci. Lett.* **2011**, *309*, 213–220. [CrossRef]
163. Chen, B.; Lai, X.J.; Li, J.; Liu, J.C.; Zhao, J.Y.; Bi, W.L.; Alp, E.E.; Hu, M.Y.; Xiao, Y.M. Experimental constraints on the sound velocities of cementite $Fe_3C$ to core pressures. *Earth Planet. Sci. Lett.* **2018**, *494*, 164–171. [CrossRef]
164. Prescher, C.; Dubrovinsky, L.; Bykova, E.; Kupenko, I.; Glazyrin, K.; Kantor, A.; McCammon, C.; Mookherjee, M.; Nakajima, Y.; Miyajima, N.; et al. High Poisson's ratio of Earth's inner core explained by carbon alloying. *Nat. Geosci.* **2015**, *8*, 220–223. [CrossRef]
165. Chen, B.; Li, Z.Y.; Zhang, D.Z.; Liu, J.C.; Hu, M.Y.; Zhao, J.Y.; Bi, W.L.; Alp, E.E.; Xiao, Y.M.; Chow, P.; et al. Hidden carbon in Earth's inner core revealed by shear softening in dense $Fe_7C_3$. *Proc. Natl. Acad. Sci. USA* **2014**, *111*, 17755–17758. [CrossRef]
166. Lord, O.T.; Walter, M.J.; Dasgupta, R.; Walker, D.; Clark, S.M. Melting in the Fe-C system to 70 GPa. *Earth Planet. Sci. Lett.* **2009**, *284*, 157–167. [CrossRef]
167. Takahashi, S.; Ohtani, E.; Sakai, T.; Kamada, S.; Ozawa, S.; Sakamaki, T.; Miyahara, M.; Ito, Y.; Hirao, N.; Ohishi, Y. Phase and melting relations of $Fe_3C$ to 300 GPa and carbon in the core. In *Carbon in Earth's Interior*; Manning, C.E., Lin, J.-F., Mao, W.L., Eds.; AGU: Washington, DC, USA, 2020.
168. Mookherjee, M.; Nakajima, Y.; Steinle-Neumann, G.; Glazyrin, K.; Wu, X.A.; Dubrovinsky, L.; McCammon, C.; Chumakov, A. High-pressure behavior of iron carbide ($Fe_7C_3$) at inner core conditions. *J. Geophys. Res. Solid Earth* **2011**, *116*. [CrossRef]
169. McGuire, C.; Komabayashi, T.; Thompson, S.; Bromiley, G.; Greenberg, E.; Prakapenka, V.B. P-V-T measurements of $Fe_3C$ to 117 GPa and 2100 K: Implications for stability of $Fe_3C$ phase at core conditions. *Am. Mineral.* **2021**. [CrossRef]
170. Chipman, J. Thermodynamics and phase diagram of Fe-C System. *Metall. Trans.* **1972**, *3*, 55–64. [CrossRef]
171. Shubhank, K.; Kang, Y.B. Critical evaluation and thermodynamic optimization of Fe-Cu, Cu-C, Fe-C binary systems and Fe-Cu-C ternary system. *Calphad* **2014**, *45*, 127–137. [CrossRef]
172. Nakajima, Y.; Takahashi, E.; Sata, N.; Nishihara, Y.; Hirose, K.; Funakoshi, K.; Ohishi, Y. Thermoelastic property and high-pressure stability of $Fe_7C_3$: Implication for iron-carbide in the Earth's core. *Am. Mineral.* **2011**, *96*, 1158–1165. [CrossRef]
173. Nakajima, Y.; Imada, S.; Hirose, K.; Komabayashi, T.; Ozawa, H.; Tateno, S.; Tsutsui, S.; Kuwayama, Y.; Baron, A.Q.R. Carbon-depleted outer core revealed by sound velocity measurements of liquid iron-carbon alloy. *Nat. Commun.* **2015**, *6*, 9942. [CrossRef]
174. Fukai, Y.; Mori, K.; Shinomiya, H. The phase diagram and superabundant vacancy formation in Fe-H alloys under high hydrogen pressures. *J. Alloys Compd.* **2003**, *348*, 105–109. [CrossRef]
175. Okuchi, T. Hydrogen partitioning into molten iron at high pressure: Implications for Earth's core. *Science* **1997**, *278*, 1781–1784. [CrossRef]

176. Zinkevich, M.; Mattern, N.; Handstein, A.; Gutfleisch, O. Thermodynamics of Fe-Sm, Fe-H, and H-Sm systems and its application to the hydrogen-disproportionation-desorption-recombination (HDDR) process for the system $Fe_{17}Sm_2$-$H_2$. *J. Alloys Compd.* **2002**, *339*, 118–139. [CrossRef]
177. Fukai, Y.; Suzuki, T. Iron-water reaction under high-pressure and its implication in the evolution of the Earth. *J. Geophys. Res. Solid Earth Planets* **1986**, *91*, 9222–9230. [CrossRef]
178. Fukai, Y. Some properties of the Fe-H system at high pressures and temperatures, and their implications for the Earth's core. In *High-Pressure Research: Application to Earth and Planetary Sciences*; Syono, Y., Manghnani, M.H., Eds.; AGU: Washington, DC, USA, 1992; pp. 373–385.
179. Sakamaki, K.; Takahashi, E.; Nakajima, Y.; Nishihara, Y.; Funakoshi, K.; Suzuki, T.; Fukai, Y. Melting phase relation of FeHx up to 20 GPa: Implication for the temperature of the Earth's core. *Phys. Earth Planet. Inter.* **2009**, *174*, 192–201. [CrossRef]
180. Shibazaki, Y.; Ohtani, E.; Fukui, H.; Sakai, T.; Kamada, S.; Ishikawa, D.; Tsutsui, S.; Baron, A.Q.R.; Nishitani, N.; Hirao, N.; et al. Sound velocity measurements in dhcp-FeH up to 70 GPa with inelastic X-ray scattering: Implications for the composition of the Earth's core. *Earth Planet. Sci. Lett.* **2012**, *313*, 79–85. [CrossRef]
181. Pepin, C.M.; Dewaele, A.; Geneste, G.; Loubeyre, P.; Mezouar, M. New iron hydrides under high pressure. *Phys. Rev. Lett.* **2014**, *113*, 265504. [CrossRef] [PubMed]
182. Hirose, K.; Tagawa, S.; Kuwayama, Y.; Sinmyo, R.; Morard, G.; Ohishi, Y.; Genda, H. Hydrogen limits carbon in liquid iron. *Geophys. Res. Lett.* **2019**, *46*, 5190–5197. [CrossRef]
183. Narygina, O.; Dubrovinsky, L.S.; McCammon, C.A.; Kurnosov, A.; Kantor, I.Y.; Prakapenka, V.B.; Dubrovinskaia, N.A. X-ray diffraction and Mossbauer spectroscopy study of fcc iron hydride FeH at high pressures and implications for the composition of the Earth's core. *Earth Planet. Sci. Lett.* **2011**, *307*, 409–414. [CrossRef]
184. Thompson, E.C.; Davis, A.H.; Bi, W.; Zhao, J.; Alp, E.E.; Zhang, D.; Greenberg, E.; Prakapenka, V.B.; Campbell, A.J. High-pressure geophysical properties of fcc phase FeHx. *Geochem. Geophys. Geosyst.* **2018**, *19*, 305–314. [CrossRef]
185. Kato, C.; Umemoto, K.; Ohta, K.; Tagawa, S.; Hirose, K.; Ohishi, Y. Stability of fcc phase FeH to 137 GPa. *Am. Mineral.* **2020**, *105*, 917–921. [CrossRef]
186. Suzuki, T.; Akimoto, S.; Fukai, Y. The system iron enstatite water at high-pressures and Temperatures-formation of iron hydride and some geophysical implications. *Phys. Earth Planet. Inter.* **1984**, *36*, 135–144. [CrossRef]
187. Caracas, R. The influence of hydrogen on the seismic properties of solid iron. *Geophys. Res. Lett.* **2015**, *42*, 3780–3785. [CrossRef]
188. Fiquet, G.; Badro, J.; Guyot, F.; Requardt, H.; Krisch, M. Sound velocities in iron to 110 gigapascals. *Science* **2001**, *291*, 468–471. [CrossRef] [PubMed]
189. Antonangeli, D.; Komabayashi, T.; Occelli, F.; Borissenko, E.; Walters, A.C.; Fiquet, G.; Fei, Y.W. Simultaneous sound velocity and density measurements of hcp iron up to 93 GPa and 1100 K: An experimental test of the Birch's law at high temperature. *Earth Planet. Sci. Lett.* **2012**, *331*, 210–214. [CrossRef]
190. Murphy, C.A.; Jackson, J.M.; Sturhahn, W. Experimental constraints on the thermodynamics and sound velocities of hcp-Fe to core pressures. *J. Geophys. Res. Solid Earth* **2013**, *118*, 1999–2016. [CrossRef]
191. Umemoto, K.; Hirose, K. Liquid iron-hydrogen alloys at outer core conditions by first-principles calculations. *Geophys. Res. Lett.* **2015**, *42*, 7513–7520. [CrossRef]
192. Komabayashi, T.; Pesce, G.; Sinmyo, R.; Kawazoe, T.; Breton, H.; Shimoyama, Y.; Glazyrin, K.; Konopkova, Z.; Mezouar, M. Phase relations in the system Fe-Ni-Si to 200 GPa and 3900 K and implications for Earth's core. *Earth Planet. Sci. Lett.* **2019**, *512*, 83–88. [CrossRef]
193. Zhang, Y.J.; Sekine, T.; Lin, J.F.; He, H.L.; Liu, F.S.; Zhang, M.J.; Sato, T.; Zhu, W.J.; Yu, Y. Shock compression and melting of an Fe-Ni-Si alloy: Implications for the temperature profile of the Earth's core and the heat flux across the core-mantle boundary. *J. Geophys. Res. Solid Earth* **2018**, *123*, 1314–1327. [CrossRef]
194. Hirose, K.; Morard, G.; Sinmyo, R.; Umemoto, K.; Hernlund, J.; Helffrich, G.; Labrosse, S. Crystallization of silicon dioxide and compositional evolution of the Earth's core. *Nature* **2017**, *543*, 99–102. [CrossRef] [PubMed]
195. Arveson, S.M.; Deng, J.; Karki, B.B.; Lee, K.K.M. Evidence for Fe-Si-O liquid immiscibility at deep Earth pressures. *Proc. Natl. Acad. Sci. USA* **2019**, *116*, 10238–10243. [CrossRef] [PubMed]